

AD _____

Award Number: DAMD17-97-1-7271

TITLE: A Novel Fuzzy Topological Approach to the Detection of Mammographic Lesions and Quantification of Parenchymal Density

PRINCIPAL INVESTIGATOR: Jayaram Udupa, Ph.D.

CONTRACTING ORGANIZATION: University of Pennsylvania
Philadelphia, Pennsylvania 19104-3246

REPORT DATE: February 2001

TYPE OF REPORT: Final

PREPARED FOR: U.S. Army Medical Research and Materiel Command
Fort Detrick, Maryland 21702-5012

DISTRIBUTION STATEMENT: Approved for Public Release;
Distribution Unlimited

The views, opinions and/or findings contained in this report are those of the author(s) and should not be construed as an official Department of the Army position, policy or decision unless so designated by other documentation.

20010724 057

REPORT DOCUMENTATION PAGE

Form Approved
OMB No. 074-0188

Public reporting burden for this collection of information is estimated to average 1 hour per response, including the time for reviewing instructions, searching existing data sources, gathering and maintaining the data needed, and completing and reviewing this collection of information. Send comments regarding this burden estimate or any other aspect of this collection of information, including suggestions for reducing this burden to Washington Headquarters Services, Directorate for Information Operations and Reports, 1215 Jefferson Davis Highway, Suite 1204, Arlington, VA 22202-4302, and to the Office of Management and Budget, Paperwork Reduction Project (0704-0188), Washington, DC 20503

| | | | |
|--|--|---|--|
| 1. AGENCY USE ONLY (Leave blank) | | 2. REPORT DATE February 2001 | 3. REPORT TYPE AND DATES COVERED Final (1 Aug 97 - 31 Jan 01) |
| 4. TITLE AND SUBTITLE A Novel Fuzzy Topological Approach to the Detection of Mammographic Lesions and Quantification of Parenchymal Density | | 5. FUNDING NUMBERS DAMD17-97-1-7271 | |
| 6. AUTHOR(S) Jayaram Udupa, Ph.D. | | | |
| 7. PERFORMING ORGANIZATION NAME(S) AND ADDRESS(ES) University of Pennsylvania Philadelphia, Pennsylvania 19104-3246 | | 8. PERFORMING ORGANIZATION REPORT NUMBER | |
| 9. SPONSORING / MONITORING AGENCY NAME(S) AND ADDRESS(ES) U.S. Army Medical Research and Materiel Command Fort Detrick, Maryland 21702-5012 | | 10. SPONSORING / MONITORING AGENCY REPORT NUMBER | |
| 11. SUPPLEMENTARY NOTES | | | |
| 12a. DISTRIBUTION / AVAILABILITY STATEMENT Approved for public release; distribution unlimited | | | 12b. DISTRIBUTION CODE |
| 13. ABSTRACT (Maximum 200 Words) This research focuses on mammographic image processing for the purpose of density quantification, lesion detection and quantification. The approaches are different from those taken in the literature in two respects. (1) They emphasize on identifying the dense regions and analyzing the parenchymal architecture. (2) They use a novel fuzzy connectedness method of object definition and image segmentation. During this project period, the following have been accomplished: The development and validation of a new method of lesion and density detection based on fuzzy connectedness that utilizes the relative strength of connectedness among objects. The development of a new class of interactive segmentation methods that are more efficient and effective for lesion segmentation than the earlier live wire methods. Further extension of the fuzzy connectedness framework and demonstration of its effectiveness in areas other than mammographic image processing. | | | |
| 14. SUBJECT TERMS Breast Cancer, Mammographic Image Processing, Lesion Detection, Density Quantification | | | 15. NUMBER OF PAGES 82 |
| | | | 16. PRICE CODE |
| 17. SECURITY CLASSIFICATION OF REPORT Unclassified | 18. SECURITY CLASSIFICATION OF THIS PAGE Unclassified | 19. SECURITY CLASSIFICATION OF ABSTRACT Unclassified | 20. LIMITATION OF ABSTRACT Unlimited |

NSN 7540-01-280-5500

TABLE OF CONTENTS

| | |
|-----------------------------------|----|
| Cover..... | 1 |
| SF 298..... | 2 |
| Table of Contents..... | 3 |
| Introduction..... | 4 |
| Body..... | 5 |
| Key Research Accomplishments..... | 11 |
| Reportable Outcomes..... | 12 |
| Conclusions..... | 15 |
| References..... | 15 |
| Appendices..... | 19 |

INTRODUCTION

The subject of this research is image processing of digitized mammograms. Its purpose is to improve the extraction of information from mammograms through image processing techniques so as to facilitate better detection and delineation of densities and lesions. The focus of this research is on mammographic density quantification and lesion delineation. Computer-assisted analysis of mammographic density would provide an objective, quantitative measure of cancer risk factor. This measure will be useful in total risk analysis in several ways; in choosing alternative screening paradigms in determining the risk-benefit-ratio for the administration of toxic preventive measures, in signaling double reading of the mammograms, and in selecting the appropriate lesion detection algorithm.

This research has the following main aims.

1. To develop and implement a fuzzy object definition method for the detection and delineation of parenchymal density, masses and microcalcifications in digitized mammograms.
2. To develop and implement a fuzzy object definition method for the classification of lesions and mammographic densities.
3. To conduct evaluation studies using histologically verified mammographic data to determine the efficacy of the proposed methods of lesion detection and quantitative classifications.

BODY

Tasks 1, 2, 3,4: Collect Image Data, Modify Affinity for Vector Valued Features, Implement and Evaluate Lesion Detection Methods.

We have digitized about 200 existing mammograms (at a resolution of 100 microns) from our patient database in the hospital. These images were transmitted to our (Medical Image Processing Group –MIPG) facility, converted to the format of 3DVIEWNIX [1] (the software platform used in the project), and stored on a medium. These data contain normal studies as well as studies with masses and microcalcifications.

We spent a considerable amount of time investigating the affinity relations that are appropriate for segmenting digitized mammograms. A novel scale-based fuzzy affinity and connectedness method has been developed, implemented in 3DVIEWNIX and tested. A brief summary of its approach [2, 3] is given below.

Fuzzy affinity between two nearby pixels is a reflexive and symmetric relation whose strength lies between 0 and 1 and indicates how the pixels locally “hang together” in the image. The notion of fuzzy affinity between two pixels is expressed as a non-decreasing function of fuzzy adjacency (dependent only on the distance between them), their homogeneity, and their agreement to some global intensity-based object property or feature. In determining the homogeneity and feature-based components of affinity between two pixels p_1 and p_2 , a neighborhood around both p_1 and p_2 are considered. The size of this neighborhood, called scale, is not fixed but depends on the size of the largest homogeneous region locally. The scale is first computed automatically for all pixels in the image.

Fuzzy connectedness between any two (not necessarily nearby) pixels p_1 and p_2 is a fuzzy relation whose strength lies between 0 and 1. It is determined by considering all possible paths

between p_1 and p_2 . A path is simply a sequence of nearby pixels. A strength of connectedness is assigned to each path which is simply the smallest affinity of successive pixels along the path. The strength of connectedness between p_1 and p_2 is the largest of the strengths of all possible paths between p_1 and p_2 .

In one way, we can imagine that two pixels are strongly connected to each other if there is a path between them through locally homogeneous regions. We call it *homogeneity-based connectedness*. In another way, the connectedness between two pixels could be imagined as their likeliness to fit the object features and unlikeness to fit the background features. We call it feature-based connectedness. One may note that *feature-based connectedness* does not have the notion of path homogeneity and thus fails to overcome the effects of slowly varying components over the image. On the other hand, homogeneity based connectedness suffers from the fact that, in some applications, objects merge with background so smoothly that always there is a path from object to background through locally homogeneous regions. This is more pronounced when blurring or partial voluming is high. Moreover, especially in a thin branch of an object, often, there are small regions with high inhomogeneity that stop the homogeneity-based paths for the rest of the branch. Therefore, the two different notions of connectedness are combined. Additionally, the notion of scale allows the correct estimation of homogeneity and object features that is insensitive to noise.

A detailed mathematical formulation of scale-based fuzzy affinity, connectedness, the associated algorithms, and their validation on both 2D and 3D clinical images and phantoms is presented in [2, 3]. A careful statistical evaluation indicates that the scale-based method is much superior to the original method described in [4].

We have investigated several methods for the delineation of lesions in digitized mammograms. We have basically pursued two types of approaches.

The first approach is based on fuzzy connectedness. It looks for abnormality in the network by high-strength-of-connectedness paths within the image. The strength of connectedness of every connecting path between every pair of pixels is determined using the method described in [3]. This method needs some further work. There are many avenues here which we did not realize earlier. This approach seems to offer, without having to explicitly detect and delineate lesions, a method to identify architectural distortions. One exciting possibility is to determine if sufficient distortion in architecture can be detected well ahead of the time of appearance of visible lesions. We are investigating this avenue currently and possibly pursue other funding sources in the future to support this activity.

The second approach we have developed is called live wire [5]. In this method, an operator initially selects a point in the vicinity of a lesion boundary. At this time a “live-wire” is displayed in real time as the operator moves the mouse cursor. The live wire represents the best path from the initial point selected by the operator to the current cursor position. Since the best path is always computed and displayed in real time, the user can test how to select a largest possible boundary segment by moving the cursor close to the boundary and checking how well the live wire snaps onto the boundary. If this boundary segment is acceptable, the user deposits the cursor which now becomes the new initial point and the process continues. Typically 2-3 points selected on the boundary in this fashion are adequate to segment and entire boundary. A 3D version of this method has also been developed [6] for segmentation of lesions in MR images. This method has also been utilized in several other applications [7, 8].

Tasks 5, 6, 7: Prepare Reports, Implement and Evaluate Density Classification Methods

A method for automatically segmenting dense regions and quantifying density has been fully developed, implemented and tested on over 100 mammograms [9, 10]. This method is described below in some detail.

Segmentation of breast from background: At the very beginning, using 3DVIEWNIX supported LIVE-WIRE [6] tool, regions corresponding to pectoral muscles are interactively excluded when those are projected in the image. In the entire process, this is the only step requiring operator intervention. Fuzzy connectivity is used as the underlying technique in segmenting breast from background. To apply the fuzzy connectivity model, we need to estimate several parameters. Studying 120 images from 60 patients, we found that the intensity histogram always contains a highly prominent peak at the lower intensities, and the peak is contributed mostly by background. The first prominent peak in the intensity histogram is detected and used to (roughly) calculate the mean and standard deviation of background intensity. To apply the fuzzy connectivity algorithm, we need to select a set of reference (seed) pixels. For this purpose, we assume that the rightmost column in the image always lies in the background. We include all these pixels in the reference set. Fuzzy connectedness processing starting from these pixels gives us a fuzzy connectivity image for background. We discard connectivity strengths in the upper half and keep the lower half as the breast region.

Fuzzy connectivity image for glandular tissue: The fuzzy connectivity method is used to enhance glandular dense regions and to suppress fat tissues; the resulting fuzzy connectivity image, in turn, is used for automatic segmentation of the glandular region. The major task in applying the fuzzy connectivity model is to estimate the parameters of the affinity relation and to select a set of reference pixels. After ignoring the upper 0.01 percentile intensities, the mean and

standard deviation parameters (for the homogeneity and feature-based affinity) are estimated from those parts of the breast region falling in the upper 25% of the intensity range. Finally, the pixels in the breast region falling in the upper 15% of the intensity range are selected as reference pixels. The fuzzy connected image for the glandular tissue is then computed.

Automatic threshold selection: For any threshold, the image is divided into two regions. Local homogeneity based affinity between every pair of spatially adjacent pixels is used to define their likeliness of belonging to the same object or of not belonging to the same object. The optimum threshold is determined from the associated statistics called threshold energy. The threshold with the minimum threshold energy is selected as the optimum threshold. We generate several descriptors from the segmented binary image and the original image to quantify the glandular tissues as described below. Note that all steps are completely automatic except the exclusion of pectoral muscles if they are included in the mammogram.

Density quantification: The method has been tested on over 80 studies (each study produces two digitized mammograms) from routine exams from two projections (CC and MLO). The population included normal as well as cancer cases (masses and calcifications). Except for the exclusion of pectoral muscles, the entire method has worked automatically on all images wherein all parameters required by the algorithms are selected automatically. The algorithms produced visually acceptable segmentations in all images. From the segmented regions and the image intensities in them, we compute a set of density related parameters including total glandularity (TG), TG/total fat(TF), TG/average fat(AvF), TG/area of breast(AB), area of glandularity(AG), AG/area of fat(AF), AG/AB. TG and TF are computed by integrating radiographic intensity over respective segmented regions while AG, AB and AF are computed by

counting the number of pixels in the respective regions. Finally, AvF is computed by dividing TF and AF.

To evaluate the density quantification method, we tested the correlation between the parameters from the two projections (CC and MLO). The correlations for TG, TG/TF, TG/AvF, TG/AB, AG, AG/AF and AG/AB are 0.967, 0.902, 0.951, 0.944, 0.959, 0.915 and 0.941 respectively.

We also conducted a phantom experiment as follows. A rectangular parallelepiped wax object was suspended in a cylindrical water bath and imaged at different orientations. The various measures based on integrating intensity in the segmented object (wax) region produced more accurate density quantification than the area measures.

Task 8, 9, 10: Prepare Technical Reports/Papers, Compare Among lesion Detection Strategies

The previously developed density segmentation method was based on the principle of fuzzy connectedness [4]. This method has been further extended and improved, resulting in the publications cited in [3, 11-13]. We believe that these theoretical and algorithmic developments are very general, constitute a breakthrough in image segmentation, and have far wider applications than just in mammographic image processing. Although not related to the grant under consideration, we have explored a variety of applications for these same algorithms, including the clutter-free display of vessels via MRA [14], Multiple Sclerosis lesion quantification via MRI [15, 16], tumor detection in the brain via MRI [17], and the quantification of hyper-intense lesions in late-life depression [18]. These algorithms have been compared with the earlier versions of the algorithms and have been shown to be more robust under noise and with improved segmentation effectiveness [11-13].

A new class of interactive methods for lesion detection based on live wire has also been developed [5]. These are user-steered methods and are needed in extremely difficult segmentation situations. These methods have been compared to manual methods and earlier live wire methods and shown to be significantly more efficient with improved precision.

Tasks 11, 12: Evaluate the Accuracy of Lesion/Density Classification, Write Technical Reports/Papers.

The density classification method has been tested on over 150 mammograms [10] and has shown high consistency (better than 0.96 correlation) between the two projections (MLO and CC) of the same breasts. This method is now being utilized in another project for density classification of women undergoing hormone therapy.

In the process of evaluating lesion classification strategies using fuzzy connectedness parameters, we have realized that it is more sensible to classify the architectural distortions quantified through fuzzy connectedness prior to the appearance of visible mammographic lesions. Based on 40 cases of masses, for which we had 2-3 prior mammograms available prior to the appearance of masses, we have evidence that the fuzzy connectedness parameters may be able to describe the architectural distortions that take place before visible lesions appear. This exciting possibility requires considerable further work to prove conclusively the preliminary observations. If proven, this may have a significant impact on the early diagnosis of breast cancer.

KEY RESEARCH ACCOMPLISHMENTS

- The development of a novel method of defining the “hanging-togetherness” of dense regions via scale-based fuzzy affinity and connectedness [3]. This framework, we believe, constitutes a breakthrough in image segmentation. It has been further studied by other research groups. We have extended this framework considerably [11-13] and demonstrated

that it is effective also in several areas of medical image analysis [14-18] other than mammographic image processing.

- An interactive method of lesion segmentation using live wire [5, 6].
- An automatic, validated method of mammographic density quantification and the development of a host of intensity-based parameters that are more accurate than the measure of the area of dense regions. This method is currently utilized in another project in which change in breast density is assessed as a result of hormone therapy.
- A novel method of detecting architectural distortions without explicitly delineating lesions. The method is being tested for its effectiveness in predicting the onset of lesions. This interesting preliminary result indicates that this method may have a significant impact on the early detection of cancer in the future before lesions appear.

REPORTABLE OUTCOMES

The following papers/patents have been presented, submitted or published.

- [1] Udupa, J.K., Saha, P.K., Lotufo, R.A.: "Fuzzy-connected object definition in images with respect to co-objects," *SPIE Proceedings*, 3661:236-245, 1999.
- [2] Saha, P.K., Udupa, J.K.: "Scale-based fuzzy connectivity: A novel image segmentation methodology and its validation," *SPIE Proceedings*, 3661:246-257, 1999.
- [3] Saha, P.K., Udupa, J.K., Conant, E.F., Chakraborty, D.P.: "Near-automatic segmentation and quantification of mammographic glandular tissue density," *SPIE Proceedings*, 3661:266-276, 1999.
- [4] Falcao, A.X., Udupa, J.K., Miyazawa, F.K.: "Ultrafast user-steered segmentation paradigm: Live-wire-on-the-fly," *SPIE Proceedings*, 3661:184-191, 1999.

- [5] Lei, T, Udupa, J.K., Saha, P.K., Odhner, D.: “3D MR angiographic visualization and artery-vein separation,” *SPIE Proceedings*, 3658:58-66, 1999.
- [6] Saha, P., Udupa, J.K.: “Scale-based fuzzy connected image segmentation: Theory, algorithms and validation,” *Computer Vision and Image Understanding*, 77(2):145-174, 2000.
- [7] Falcao, A., Udupa, J.K., Miyazawa, F.K.: “An ultrafast user-steered image segmentation paradigm: Live-wire-on-the-fly,” *IEEE Transactions on Medical Imaging*, 19(1):55-61, 2000.
- [8] Rice, B.L., Udupa, J.K.: “Fuzzy connected clutter-free volume rendering for MR angiography,” *International Journal of Imaging Systems and Technology*, 11:62-70, 2000.
- [9] Falcao, A.X., Udupa, J.K.: “A 3D generalization of user-steered live wire segmentation,” *Medical Image Analysis*, 4:389-402, 2000.
- [10] Saha, P.K., Udupa, J.K.: “A new optimum thresholding method using region homogeneity and class uncertainty,” *SPIE Proceedings*, 3979:180-191, 2000.
- [11] Saha, P.K., Udupa, J.K.: “Scale-based filtering of medical images,” *SPIE Proceedings*, 3979:735-746, 2000.
- [12] Udupa, J.K., Grossman, R.I., Nyul, L.G., Ge, Y., Wei, L.: “Multiprotocol MR image segmentation in multiple sclerosis: Experience with over 1000 studies,” *SPIE Proceedings*, 3979:1017-1027, 2000.
- [13] Lei, T., Udupa, J.K., Saha, P.K., Odhner, D.: “Separation of artery and vein in contrast enhanced MRA images,” *SPIE Proceedings*, 3978:233-244, 2000.

[14] Saha, P.K., Udupa, J.K.: Iterative relative fuzzy connectedness and object definition: Theory, algorithms, and applications in image segmentation." *Proceedings of IEEE Workshop on Mathematical Methods in Biomedical Image Analysis*, Hilton Head, South Carolina, pp. 28-35, 2000.

[15] Saha, P.K., Udupa, J.K.: "Relative fuzzy connectedness among multiple objects: Theory, algorithms, and applications in image segmentation," *Computer Vision and Image Understanding*, in press.

[16] Saha, P., Udupa, J.K., Conant, E., Chakraborty, D.P., Sullivan, D.: "Breast tissue glandularity quantification via digitized mammograms," *IEEE Transactions on Medical Imaging*, accepted.

[17] Udupa, J.K., Saha, P.K., Lotufo, R.A.: "Relative fuzzy connectedness and object definition: Theory, algorithms, and applications in image segmentation," *IEEE Transactions on Pattern Analysis and Machine Intelligence*, submitted.

[18] Saha, P.K., Udupa, J.K.: "Optimum image thresholding via class uncertainty and region homogeneity," *IEEE Transactions on Pattern Analysis and Machine Intelligence*, in press.

[19] Saha, P.K., Udupa, J.K.: "Scale-based image filtering preserving boundary sharpness and fine structures," *IEEE Transactions on Medical Imaging*, submitted.

[20] Udupa, J.K., Grevera, G.J.: "Go digital, go fuzzy," *Pattern Recognition Letters*, submitted.

[21] Lei, T., Udupa, J.K., Saha, P.K., Odhner, D., Baum, R., Tadikonda, S.K., Yucel, K.: "3D MRA visualization and artery-vein separation using blood-pool contrast agent MS-325," *Journal of Academic Radiology*, accepted.

[22] Saha, P.K., Udupa, J.K.: "Fuzzy connected object delineation: Axiomatic path strength definition and the case of multiple seeds," *Computer Vision and Image Understanding*, submitted.

CONCLUSIONS

1. The new scale-based fuzzy connectedness method is more robust and effective than the original method. It is very effective for mammographic image segmentation as well as in several other applications.
2. Glandularity is considered to be one of the strongest factors for breast cancer. Automatic breast glandularity quantification from digitized mammograms is practical using the proposed method. The method removes the subjectivity inherent in interactive threshold selection techniques currently used.
3. The live wire method is effective in segmenting mammographic lesions. It seems to be more robust than the active contour methods commonly used. Its utility is being evaluated in 3D (MRI) lesion segmentation.
4. The fuzzy connectedness method facilitates various ways of characterizing the architecture of the breast. There are some preliminary indications that the distortions in architectures as measured by fuzzy connectedness parameters may predict the occurrence of visible lesions.

REFERENCES

[1] Udupa, J.K., Odhner, D., Samarasekera, S., Goncalves, R.J., Iyer, K., Venugopal, K., Furui, S.: "3DVIEWNIX: A open, transportable, multidimensional, multimodality, multiparametric imaging system," *Proceedings of SPIE*, 2164:58-73, 1994.

- [2] Saha, P.K., Udupa, J.K.: "Scale-based fuzzy connectivity: A novel image segmentation methodology and its validation," *SPIE Proceedings*, 3661:246-257, 1999.
- [3] Saha, P.K., Udupa, J.K.: "Scale-based fuzzy connected image segmentation: Theory, algorithms and validation," *Computer Vision and Image Understanding*, 77(2):145-174, 2000.
- [4] Udupa, J.K., Samarasekera, S.: "Fuzzy connectedness and object definition: Theory, algorithms, and applications in image segmentation," *Graphical Models and Image Processing*, 58(3):246-261, 1996.
- [5] Falcao, A., Udupa, J.K., Miyazawa, F.K.: "An ultrafast user-steered image segmentation paradigm: Live-wire-on-the-fly," *IEEE Transactions on Medical Imaging*, 19(1):55-61, 2000.
- [6] Falcao, A.X., Udupa, J.K.: "A 3D generalization of user-steered live wire segmentation," *Medical Image Analysis*, 4:389-402, 2000.
- [7] Stindel, E., Udupa, J.K., Hirsch, B.E., Odhner, D., Couture, C.: "3D MR image analysis of the morphology of the rear foot: Application to classification of bones," *Computerized Medical Imaging and Graphics*, 23(2):75-83, 1999.
- [8] Stindel, E., Udupa, J.K., Hirsch, B.E., Odhner, D.: "A characterization of the geometric architecture of the peritalar joint complex via MRI: An aid to classification of feet," *IEEE Transactions on Medical Imaging*, 18:753-763, 1999.
- [9] Saha, P.K., Udupa, J.K., Conant, E.F., Chakraborty, D.P.: "Near-automatic segmentation and quantification of mammographic glandular tissue density," *SPIE Proceedings*, 3661:266-276, 1999.

- [10] Saha, P., Udupa, J.K., Conant, E., Chakraborty, D.P., Sullivan, D.: "Breast tissue glandularity quantification via digitized mammograms," *IEEE Transactions on Medical Imaging*, in press.
- [11] Udupa, J.K., Saha, P.K., Lotufo, R.A.: "Fuzzy-connected object definition in images with respect to co-objects," *SPIE Proceedings*, 3661:236-245, 1999.
- [12] Udupa, J.K., Saha, P.K.: "Relative fuzzy connectedness among multiple objects: Theory, algorithms and applications in image segmentation," *Computer Vision and Image Understanding*, accepted.
- [13] Udupa, J.K., Saha, P.K., Lotufo, R.A.: "Relative fuzzy connectedness and object definition: Theory, algorithms and applications in image segmentation," *IEEE Transactions on Pattern Analysis and Machine Intelligence*, submitted.
- [14] Rice, B.L., Udupa, J.K.: "Fuzzy connected clutter-free volume rendering for MR angiography," *International Journal of Imaging Systems and Technology*, 11:62-70, 2000.
- [15] Udupa, J.K., Grossman, R.I., Nyul, L.G., Ge, Y., Wei, L.: "Multiprotocol MR image segmentation in multiple sclerosis: Experience with over 1000 studies," *SPIE Proceedings*, 3979:1017-1027, 2000.
- [16] Ge, Y., Udupa, J.K., Nyul, L.G., Wei, L., Grossman, R.I.: "Numerical tissue characterization in MS via standardization of the MR image intensity scale," *Journal of Magnetic Resonance Imaging*, 12:715-721, 2000.
- [17] Moonis, G., Liu, J., Udupa, J.K., Hackney, D.C.: "Estimation of tumor volume using fuzzy connectedness segmentation of MRI," *Radiology*, submitted.

[18] Kumar, A., Bilker, W., Jin, Z., Udupa, J.: "Atrophy and high intensity lesions: Complementary neurobiological mechanisms in late-life major depression," *Neuropsychopharmacology* 22(3):264-274, 2000.

Fuzzy connected object definition in images with respect to co-objects

Jayaram K. Udupa^a, Punam K. Saha^a and Roberto A. Lotufo^b

^aMedical Image Processing Group, Department of Radiology
University of Pennsylvania, Philadelphia, PA 19104

^bState University of Campinas, Faculty of Electrical Engineering and Computing
Campinas SP, Brazil

ABSTRACT

Tangible solutions to practical image segmentation are vital to ensure progress in many applications of medical imaging. Toward this goal, we previously proposed a theory and algorithms for fuzzy connected object definition in n -dimensional images. Their effectiveness has been demonstrated in several applications including multiple sclerosis lesion detection/delineation, MR Angiography, and craniofacial imaging. The purpose of this work is to extend the earlier theory and algorithms to fuzzy connected object definition that considers all relevant objects in the image simultaneously. In the previous theory, delineation of the final object from the fuzzy connectivity scene required the selection of a threshold that specifies the weakest "hanging-togetherness" of image elements relative to each other in the object. Selection of such a threshold was not trivial and has been an active research area. In the proposed method of relative fuzzy connectivity, instead of defining an object on its own based on the strength of connectedness, all co-objects of importance that are present in the image are also considered and the objects are let to compete among themselves in having image elements as their members. In this competition, every pair of elements in the image will have a strength of connectedness in each object. The object in which this strength is highest will claim membership of the elements. This approach to fuzzy object definition using a relative strength of connectedness eliminates the need for a threshold of strength of connectedness that was part of the previous definition. It seems to be more natural since it relies on the fact that an object gets defined in an image by the presence of other objects that coexist in the image. All specified objects are defined simultaneously in this approach. The concept of iterative relative fuzzy connectivity has also been introduced. Robustness of relative fuzzy objects with respect to selection of reference image elements has been established. The effectiveness of the proposed method has been demonstrated using a patient's 3D contrast enhanced MR angiogram and a 2D phantom scene.

Keywords: Image segmentation, fuzzy connectivity, object definition, object delineation

1. INTRODUCTION

Two- and higher-dimensional images are currently available through sensing devices that operate on a wide range of frequency in the electromagnetic spectrum — from ultrasound to visible light to X- and γ -rays.¹ The activity of defining meaningful objects in these images, generally referred to as image segmentation, spans over three decades.² The present paper falls in this category and deals with an extension of a previous work³ which was also motivated by the problem of defining objects in multidimensional medical images. Defining objects in these image data is fundamental to most image-related applications. It is obvious that defining objects is essential prior to their visualization, manipulation, and analysis. Even operations such as image interpolation and filtering, seemingly unrelated to object definition, can be made more effective with object knowledge.

Object definition in images may be considered to consist of mainly two related tasks — recognition and delineation. *Recognition* is the process of determining roughly the whereabouts of the object in the image. *Delineation*, on the other hand, is a process that defines the precise spatial extent and composition of the object in the image. A variety of approaches have been taken in biomedical imaging applications, wherein the degree of automation for recognition and delineation ranges from completely manual to completely automatic.

Correspondence: Email: jay@mipg.upenn.edu; http://www.mipg.upenn.edu/~Vnews/mipg_images/jay1.gif
Telephone: 215 662 6780; Fax 215 898 9145

Among automatic approaches to recognition, two classes may be identified: knowledge-based and model-based. Knowledge-based methods^{4,5} form hypotheses relating to objects and test them for recognizing object parts. Usually, some preliminary delineation is needed for forming and testing hypotheses relating to object components. Model-based methods⁶⁻⁸ utilize predefined object models to optimally match image information to models for recognizing object components.

Approaches to delineation may be broadly classified into two groups: boundary-based and region-based. Boundary-based methods⁹⁻¹¹ produce a delineation of the object boundaries in the image whereas region-based methods^{3,12-14} generate delineations in the form of the region occupied by the object in the image. Each of these groups may be further divided into subgroups — hard and fuzzy — depending on whether the defined regions/boundaries are described by hard or fuzzy sets.

The subject matter of this paper is related to delineation. In a previous paper,³ we described a theory and algorithms for fuzzy connected object definition, treating a given image as a fuzzy subset of the set of spatial elements (spels) comprising the image. The method is currently utilized in several medical imaging applications including multiple sclerosis lesion segmentation and quantification,¹⁵⁻¹⁷ MR angiography,¹⁸ and hard and soft tissue 3D imaging for craniofacial surgery.¹⁹

In the present paper, an extension to the above definition of fuzzy objects is proposed. In the proposed method of relative fuzzy connectivity, instead of defining an object on its own based on the strength of connectedness, all co-objects of importance that are present in the image are also considered and the objects are let to compete among themselves in having spels as their members. In this competition, every pair of spels in the image will have a strength of connectedness in each object. The object in which this strength is highest will claim membership of the spels. This approach to fuzzy object definition using a relative strength of connectedness eliminates the need for a threshold of strength of connectedness that was part of the previous definition. It seems to be more natural since it relies on the fact that an object gets defined in an image by the presence of other objects that coexist in the image. All specified objects are defined simultaneously in this approach. Its theory and algorithms are presented in Sections 2 and 3, respectively. In section 4, we introduce the key ideas behind the extension of the relative connectivity model to an iterative framework. In Section 5, we illustrate the results of application of these methods on a contrast enhanced MR angiography data set. In the same section, using a 2D phantom, we compare the method to a method of optimum thresholding of the fuzzy connectivity scenes.^{3,20} Finally, concluding remarks are drawn in Section 6.

2. THEORY

Terminologies and notations of our previous paper³ are followed in this paper. For completeness, some of the key concepts that are required in this paper are briefly described here. Prior to this, an intuitive description of the key ideas is given using a two dimensional example.

2.1. An Outline of the Key Ideas

Consider a 2D image composed of three regions corresponding to three objects O_1, O_2, O_3 as illustrated in Figure 1, O_3 being the background. Suppose we determine an affinity relation³ for each object that assigns to every pair of nearby spels in the image a value based on the nearness of spels in space and in intensity (or in features derived from intensities). Affinity represents local “hanging togetherness” of spels. To every “path” connecting every pair of spels, such as the solid curve π_1 connecting c and d in Figure 1, a “strength of connectedness” in every object is assigned which is simply the smallest pairwise affinity (associated with the corresponding object) of spels along the path. If the affinities are derived properly, then π_1 is likely to have a higher strength in O_1 than in O_2 or in O_3 . Further, a path such as π_2 is likely to have a lower strength in O_1 than the strength of π_1 in O_1 . This relative strength of connectedness in different objects offers a natural mechanism for partitioning spels into regions based on the strongest paths between every pair of spels in every object. A spel such as a in the fuzzy boundary between O_1 and O_3 will be claimed by O_1 or O_3 depending on which pool of spels it hangs together more strongly.

2.2. Notations and Definitions

Let X be any reference set. A *fuzzy subset* A of X is a set of ordered pairs $\{(x, \mu_A(x)) | x \in X\}$ where $\mu_A : X \rightarrow [0, 1]$ is the *membership function* of A in X . A *fuzzy relation* ρ in X is a fuzzy subset, $\{((x, y), \mu_\rho(x, y)) | x, y \in X\}$, of $X \times X$. ρ will be called a *similitude relation* in X if it is *reflexive* (i.e., $\forall x \in X, \mu_\rho(x, x) = 1$), *symmetric* (i.e.,

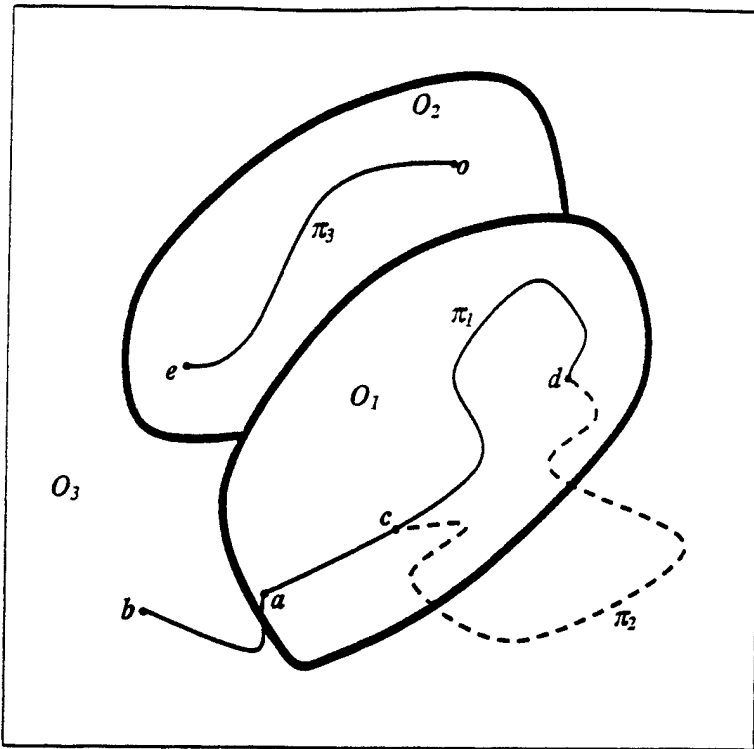


Figure 1. Illustration of the basic ideas of relative connectivity.

$\forall x, y \in X, \mu_\rho(x, y) = \mu_\rho(y, x)$ and *transitive* (i.e., $\forall x, z \in X, \mu_\rho(x, z) = \max_{y \in X} [\min[\mu_\rho(x, y), \mu_\rho(y, z)]]$). The analogous concept for a hard binary relation is an *equivalence relation*.

The pair (Z^n, α) , where Z^n is the set of n -tuples of integers and α is a *fuzzy spel adjacency relation* (i.e., any fuzzy relation that is reflexive and symmetric) on Z^n , will be referred to as a *fuzzy digital space*. Elements of Z^n will be called a *spel* (short for spatial element). A *scene* over a fuzzy digital space (Z^n, α) is a pair $C = (C, f)$ where $C = \{c \mid b_j \leq c_j \leq b_j \text{ for some } b \in Z_+^n\}$, Z_+^n is the set of n -tuples of positive integers, f is a function whose domain is C , called the *scene domain*, and whose range is a set of numbers $[L, H]$.

Any fuzzy relation κ in C is said to be a *fuzzy spel affinity relation in C* if it is reflexive and symmetric. In practice, κ should be such that $\mu_\kappa(c, d)$ is a function of the fuzzy adjacency between c and d , the homogeneity of their intensities (or other features) and their agreement to some expected value of object intensity (or features).²⁰ Further, $\mu_\kappa(c, d)$ may also depend on the scale of the object at c and d .²⁰ Throughout this paper, κ with an appropriate subscript and/or a superscript will be used to denote fuzzy spel affinity. A *path* π in C from a spel c to a spel d is a sequence $\langle c_1, c_2, \dots, c_m \rangle$ of $m \geq 2$ spels in C , such that $c_1 = c$ and $c_m = d$. The *strength assigned to a path* is defined as the weakest affinity between successive pairs of elements along the path. Thus, the strength of π is $\min_{1 \leq i < m} [\mu_\kappa(c_i, c_{i+1})]$. For any $S \subseteq C$, we say that the path π is *contained in S* if all all spels in π belong to S . The *strength of fuzzy κ -connectedness* from c to d , denoted $\mu_K(c, d)$, is the maximum of the strengths of all paths between c and d . We have shown earlier³ that fuzzy κ -connectedness is a similitude relation. Throughout this paper, the upper case form of the symbol used to represent a fuzzy spel affinity will be used for the corresponding fuzzy connectedness relation.

For any scene $C = (C, f)$ over (Z^n, α) , for any fuzzy spel affinity κ in C , and for any spel $o \in C$, the κ -*connectivity scene of o in C* is the scene $C_{K_o} = (C, f_{K_o})$ such that, for any $c \in C$, $f_{K_o}(c) = \mu_K(o, c)$.

2.3. Relative Fuzzy κ -Objects

For any spels o, b in C , define

$$P_{ob_\kappa} = \{c \mid c \in C \text{ and } \mu_K(o, c) > \mu_K(b, c)\}. \quad (1)$$

The idea here is that o and b are spels specified in “object” and “background”, respectively. Note that $P_{ob_\kappa} = \emptyset$ if $b = o$.

A *relative fuzzy κ -object* \mathcal{O} of a scene $C = (C, f)$ containing a spel o relative to a background containing a spel b is the fuzzy subset of C defined by the membership function

$$\mu_{\mathcal{O}}(c) = \begin{cases} \eta(f(c)), & \text{if } c \in P_{ob_\kappa} \\ 0, & \text{otherwise.} \end{cases} \quad (2)$$

where η is an “objectness” function whose domain is $[L, H]$ and whose range is $[0, 1]$. The range of $f(c)$ is usually not $[0, 1]$ and $f(c)$ itself may not directly represent the degree of objectness. For example, in a CT scene of the lungs, the spels consisting of the interior of the bronchial tree have low $f(c)$ values. The proper choice of η to give accurate values of the measurements (such as volume) that are sought from the segmented fuzzy object is a non trivial issue. Since, it is out of scope of the present work, we will not delve into this here. For short, we will refer to \mathcal{O} as simply a *relative fuzzy κ -object* of C . Some particular cases are instructive to study. Suppose $\mu_K(b, o) = 1$. Then by (1), $P_{ob_\kappa} = \emptyset$ and the relative κ -object is empty. This makes sense since both o and b are inside the “object” in this case, and there is no meaningful separation between sets of spels “hanging together” with o and with b . Note also that, when C is a binary scene and $f(o) \neq f(b)$, i.e., $\mu_K(o, b) \neq 1$, then P_{ob_κ} is essentially a connected component of spels whose type is that of o that contains o . To ensure that this is a reasonable definition, we will state (but not prove) several properties of relative fuzzy κ -objects. The most important among these is that, for any spel p in P_{ob_κ} and most spels q not in P_{ob_κ} , we get the same relative fuzzy κ -object.

The following theorem states the tightness of relative fuzzy κ -objects.

Theorem 1. For any scene $C = (C, f)$ over (Z^n, α) , for any fuzzy spel affinity κ in C , and for any spels o, b, p and c in C such that $p \in P_{ob_\kappa}$,

$$\mu_K(p, c) > \mu_K(b, c) \quad (3)$$

if, and only if, $c \in P_{ob_\kappa}$.

The following theorem asserts the robustness of relative fuzzy κ -objects with respect to reference spels specified in the object and in the background.

Theorem 2. For any scene $C = (C, f)$ over (Z^n, α) , for any fuzzy spel affinity κ in C , and for any spels o, b, p and q in C such that $p \in P_{ob_\kappa}$,

$$P_{ob_\kappa} = P_{pq_\kappa} \text{ if } q \in P_{bo_\kappa}. \quad (4)$$

Note that the condition in (4) is sufficient for $P_{ob_\kappa} = P_{pq_\kappa}$ but not necessary. The necessary and sufficient condition is expressed in the following theorem.

Theorem 3. For any scene $C = (C, f)$ over (Z^n, α) , for any fuzzy spel affinity κ in C , and for any spels o, b, p and q in C such that $p \in P_{ob_\kappa}$,

$$P_{ob_\kappa} = P_{pq_\kappa} \text{ if, and only if, } \mu_K(b, o) = \mu_K(q, o). \quad (5)$$

The above two theorems have different implications in the practical computation of relative fuzzy κ -objects in a given scene in a repeatable, consistent manner. Although less specific, and therefore more restrictive, Theorem 2 offers practically a more relevant guidance than Theorem 3 for selecting spels in the object and background so that the relative fuzzy κ -object defined is independent of the reference spels.

It follows from Theorems 2 and 3, by setting $p = o$, that $P_{oq_\kappa} = P_{ob_\kappa}$. However, the constancy of the relative fuzzy κ -object, even in this situation where the reference spel for the object is fixed but changeable only for the background, requires constraints expressed in (4) and (5).

The following theorem states an important property of relative fuzzy κ -objects, namely that their domain, that is the set $P_{ob\kappa}$, is connected in the sense that for any two spels $p, c \in P_{ob\kappa}$, the best path between them is contained by $P_{ob\kappa}$.

Theorem 4. For any scene $C = (C, f)$ over (Z^n, α) , for any fuzzy spel affinity κ in C , and for any spels o, b, p and c in C such that $p, c \in P_{ob\kappa}$, the best path connecting p and c is contained in $P_{ob\kappa}$.

3. ALGORITHMS

In this section, we present an algorithm, named $\kappa RFOE$, for extracting the relative fuzzy κ -object \mathcal{O} of a scene $C = (C, f)$ containing a spel, say o , relative to a background containing a spel, say b . Prior to this, we present another algorithm, named κFOE , for creating the κ -connectivity scene of o in C . Algorithm κFOE^3 is based on dynamic programming and is called by algorithm $\kappa RFOE$.

Algorithm $\kappa FOE(o)$

Input: $C = (C, f)$, and κ as defined in Section 2.

Output: κ -connectivity scene $C_{K_o} = (C, f_{K_o})$.

Auxiliary Data Structures: An n -D array representing $C_{K_o} = (C, f_{K_o})$ and a queue Q of spels. We refer to the array itself by C_{K_o} for the purpose of the algorithm.

begin

0. set all elements of C_{K_o} to 0 except the spel o which is set to 1;
1. push all spels $c \in C$ such that $\mu_\kappa(o, c) > 0$ to Q ;
2. **while** Q is not empty **do**
3. remove a spel c from Q ;
4. find $f_{\max} = \max_{d \in C} [\min[f_{K_o}(d), \mu_\kappa(c, d)]]$;
5. **if** $f_{\max} > f_{K_o}(c)$ **then**
6. set $f_{K_o}(c) = f_{\max}$;
7. push all spels e such that $\mu_\kappa(c, e) > f_{K_o}(e)$ to Q ;
8. **endif**;
9. **endwhile**;
10. output the κ -connectivity scene C_{K_o} ;

end

Algorithm $\kappa RFOE(o, b)$

Input: $C = (C, f)$, and κ as defined in Section 2.

Output: The relative fuzzy κ -object $\mathcal{O} = (C, \mu_{\mathcal{O}})$ of C .

Auxiliary Data Structures: Three n -D arrays to store the following: (1) the κ -connectivity scene $C_{K_o} = (C, f_{K_o})$, (2) the κ -connectivity scene $C_{K_b} = (C, f_{K_b})$, and (3) \mathcal{O} .

begin

0. set $C_{K_o} = \kappa FOE(o)$;
1. set $C_{K_b} = \kappa FOE(b)$;
2. **for** all $c \in C$ **do**
3. **if** $f_{K_o}(c) > f_{K_b}(c)$ **then**
4. set $\mu_{\mathcal{O}}(c) = \eta(f(c))$;
5. **else**
6. set $\mu_{\mathcal{O}}(c) = 0$;
7. **endif**
8. **endfor**
9. output the relative fuzzy κ -object \mathcal{O} ;

end

4. ITERATIVE RELATIVE FUZZY κ -OBJECTS

In this section, we introduce the key ideas behind an extension of relative connectedness to an iterative framework, while still satisfying the key ideas behind relative connectedness developed in Section 2.

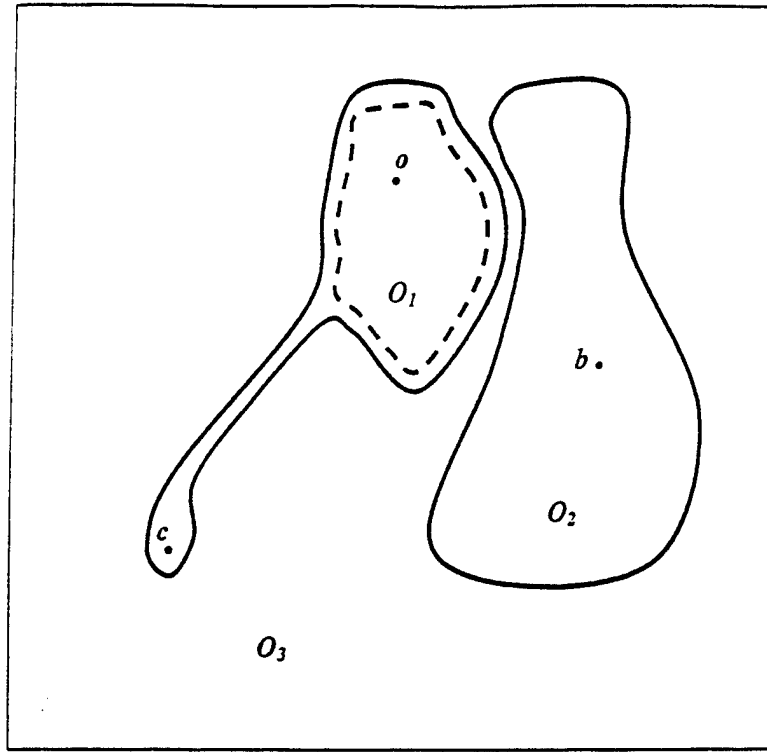


Figure 2. Illustration of the basic ideas of iterative relative connectivity.

Consider the situation illustrated in Figure 2 which demonstrates three objects O_1 , O_2 and O_3 . It is very likely that, for a spel such as c , $\mu_K(o, c) \approx \mu_K(b, c)$ because of the blurring that takes place in those parts where O_1 and O_2 come close together. In this case, the strongest path from b to c is likely to pass through the “core” of O_1 indicated by the dotted curve in the figure. This core which is roughly P_{ob_n} , can be detected first and then excluded from consideration in a subsequent iteration for any path from b to c to pass through. Then, we can substantially weaken the strongest path from b to c compared to the strongest path from o to c which is still allowed to pass through the core. This leads us to an iterative strategy to grow from o (and so complementarily from b) to more accurately capture O_1 (and O_2) than if a single shot relative connectedness strategy is used. An outline of this formulation is given below.

For any fuzzy affinity κ and any two spels $c, d \in C$, define

$$\mu_{\kappa_{ob}^0}(c, d) = \mu_\kappa(c, d) \quad (6)$$

$$P_{ob_n}^0 = \{c \mid c \in C \text{ and } \mu_K(o, c) > \mu_{\kappa_{ob}^0}(b, c)\}. \quad (7)$$

Note that $P_{ob_n}^0$ is exactly the same as P_{ob_n} , defined in (1). Assuming that $P_{ob_n}^{i-1}$ and κ_{ob}^{i-1} for any integer i , $P_{ob_n}^i$ and κ_{ob}^i are defined as follows. For all $c, d \in C$

$$\mu_{\kappa_{ob}^i}(c, d) = \begin{cases} 0, & \text{if } c \text{ or } d \in P_{ob_n}^{i-1} \\ \mu_\kappa(c, d), & \text{otherwise,} \end{cases} \quad (8)$$

$$P_{ob_n}^i = \{c \mid c \in C \text{ and } \mu_K(o, c) > \mu_{\kappa_{ob}^i}(b, c)\}. \quad (9)$$

An *iterative relative fuzzy κ^i -object* \mathcal{O}^i of a scene $\mathcal{C} = (C, f)$ containing a spel o relative to a background containing a spel b is the fuzzy subset of C defined by the membership function

$$\mu_{\mathcal{O}^i}(c) = \begin{cases} \eta(f(c)), & \text{if } c \in P_{ob_n}^i, \\ 0, & \text{otherwise.} \end{cases} \quad (10)$$

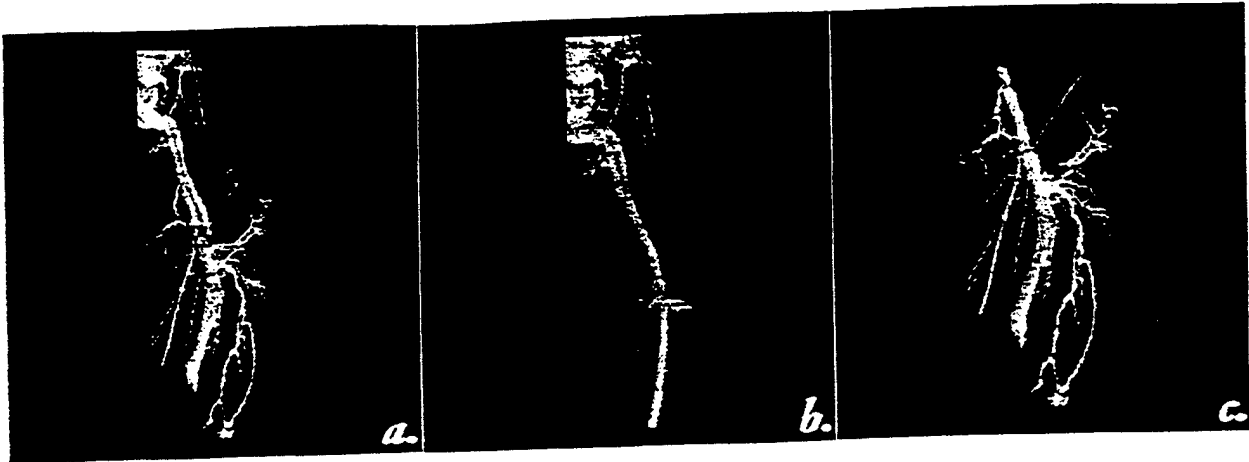


Figure 3. Results of application on a contrast enhanced 3D MR angiogram of a patient's left thigh. (a) Whole vessel tree structure automatically segmented using scale-based fuzzy connectedness. (b) Artery tree structure segmented via relative fuzzy connectivity. (c) Same as (b) for vein.

We are currently pursuing a rigorous mathematical and experimental study of the properties, robustness and effectiveness of this iterative relative fuzzy connectedness strategy for image segmentation.

5. RESULTS AND DISCUSSION

In this section, we demonstrate the effectiveness of the proposed relative fuzzy connectedness method both qualitatively and quantitatively. Figure 3 demonstrates the results of application of the method on a 3D contrast enhanced MR angiogram of a patient's left thigh. Figure 3(a) shows the whole vessel structure which was automatically segmented from the MR angiogram using scale-based fuzzy connectedness²⁰ and was rendered using shell rendering.²¹ Figure 3(b) shows the segmented artery structure obtained using relative fuzzy connectedness while Figure 3(c) shows the segmented vein structure. Here, reference voxels were manually selected inside artery and inside vein. The same fuzzy affinity relation that was used for the whole vessel segmentation was adopted for artery-vein separation. The angiography scene has a domain of $512 \times 512 \times 60$ and a voxel size of $0.94 \text{ mm} \times 0.94 \text{ mm} \times 1.80 \text{ mm}$.

Figure 4 quantitatively demonstrates the effectiveness of the method. Figure 4(a) shows the white matter region manually segmented from a 2D slice of a 3D MR scene of a multiple sclerosis patient's head. The segmentation of the white matter region was carefully performed using 3DVIEWNIX²² supported Live-wire¹¹ tool. A new 2D scene was then obtained by assigning to every pixel in the segmented white matter region a constant intensity equal to the average intensity within the segmented white matter region in the original slice, and by assigning to each of the rest of the pixels a constant intensity equal to the average intensity within the segmented gray matter region in the original slice. From the simulated scene, we created the actual test phantom by adding (a) a blurring using a 2D Gaussian kernel, (b) a 0-mean Gaussian correlated noise, and (c) a slowly varying (ramp) background component from 0 to 100 across the columns. Figure 4(b) shows the final test phantom scene. Figure 4(c) shows the scale-based fuzzy connectivity scene for the phantom scene of Figure 4(b). From the fuzzy connectivity scene, the best possible hard segmentation of white matter region was obtained as follows. A distance between two binary scenes is defined as the percentage of normalized counts of pixel mismatches between the two binary scenes. The fuzzy connectivity scene was then segmented at a threshold at which the distance between the segmented binary scene and the white matter scene (i.e., the initial truth) of Figure 4(a) is minimum. Figure 4(d) shows the best possible hard segmentation for white matter region from the fuzzy connectivity scene of Figure 4(c). (Note that the best threshold was selected by exhaustive search.) The computed distance for the segmented scene of Figure 4(d) is 2.81574. Figure 4(e) shows the segmented white matter region using relative fuzzy connectivity; here, the computed distance for the segmented scene is 2.60409. In both cases, the same parameters for fuzzy affinity relations and the same set of reference pixels (for white matter region) were used. One background reference pixel was selected for relative fuzzy connectivity. The phantom scene has a domain of 189×230 and a pixel size of $0.86 \text{ mm} \times 0.86 \text{ mm}$. Although, the final segmentations in

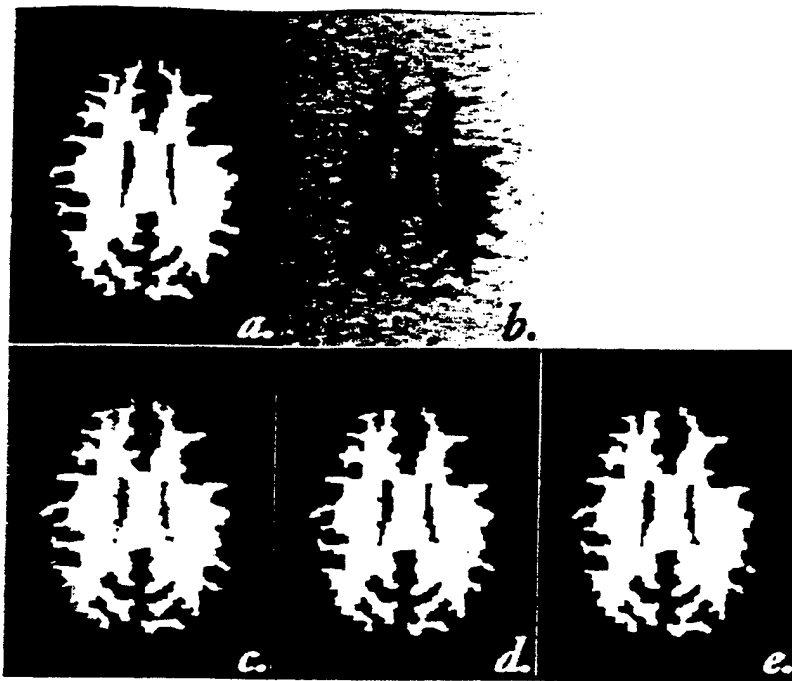


Figure 4. Results of application of relative fuzzy connectivity on a 2D phantom. (a) Binary white matter region manually segmented out from a 2D slice of a 3D MR scene of a multiple sclerosis patient's head. (b) Test phantom scene generated from (a) after adding noise, blurring and background variation. (c) Scale-based fuzzy connectivity scene for white matter region. (d) Hard segmented white matter region obtained from (c) at the best possible threshold. (e) Hard segmented white matter region obtained via relative fuzzy connectivity.

Figures 4(d) and (e) are visually very close. the segmentation using relative connectivity is closer to the initial truth. This observation may be argued by the fact that in absolute fuzzy connectivity, a fixed global threshold is chosen while in relative connectivity the competition between objects (foreground and background) is spatially variant. Effectively, relative connectedness allows a variable threshold in the strength of connectivity in different parts of the scene. Most importantly, to achieve the best threshold in absolute fuzzy connectivity, the initial phantom truth is used which is not available in any real application. Relative fuzzy connectivity eliminates this need.

6. CONCLUSION

Based on our previously developed framework of fuzzy connectedness and object definition,^{3,20} we have proposed an extension of this framework that considers all relevant objects simultaneously. The fundamental premise on which this is developed is that an object gets defined in an image by the existence of other co-objects (including the background). We consider certain regions in the image as part of the object because these regions hang-together more strongly with object elements than with background elements.

One drawback of the previous fuzzy connectivity theory is having to select a threshold for the fuzzy connectivity scene to delineate the object region. Relative fuzzy connectivity provides an effective and robust solution to this problem. The robustness of relative fuzzy objects with respect to reference pixel selection has been stated. An algorithm for computing relative fuzzy connected objects using dynamic programming has also been presented. The concept of iterative relative fuzzy connectivity has been introduced.

We have demonstrated the effectiveness of the proposed method in artery-vein separation in a contrast enhanced 3D MR angiogram. Based on a 2D phantom scene, we have shown that the segmentation by relative fuzzy connectivity is better than that obtainable via the best thresholding of the absolute fuzzy-connectivity scene. More extensive experiments in several ongoing applications are currently undergoing, as well as the development of the theory for multiple objects.

ACKNOWLEDGMENTS

The authors are grateful to Dr. Tianhu Lei for the MR vessel image data. The work of the authors is supported by grants DAMD 179717271 and NS 37172.

REFERENCES

1. Z. H. Cho, J. P. Jones, and M. Sing, *Foundation of Medical Imaging*, John Wiley & Sons Inc., New York, 1993.
2. R. M. Haralick and L.G. Shapiro, "Image segmentation techniques" *Computer Vision, Graphics and Image Processing*, **29**, pp. 100-132, 1985.
3. J. K. Udupa and S. Samarasekera, "Fuzzy connectedness and object definition: theory, algorithms, and applications in image segmentation", *Graphical Models and Image Processing*, **58**, pp. 246-261, 1996.
4. S. Raya, "Low-level segmentation of 3-D magnetic resonance brain images — a rule-based system", *IEEE Transactions on Medical Imaging*, **9**, pp. 327-337, 1990.
5. L. Gong and C. Kulikowski, "Composition of image analysis processes through object-centered hierarchical planning" *IEEE Transactions on Pattern Analysis and Machine Intelligence*, **17**, pp. 997-1009, 1995.
6. M. Kamber, R. Singhal, D. Collins, G. Francis, and A. Evans, "Model-based 3D segmentation of multiple sclerosis lesions in magnetic resonance brain images", *IEEE Transactions on Medical Imaging*, **4**, pp. 442-453, 1995.
7. J. Gee, M. Reivich, and R. Bajcsy, "Elastically deforming 3D atlas to match anatomical brain images", *Journal of Computer Assisted Tomography*, **17**, pp. 225-236, 1993.
8. G. Christensen, R. Rabbitt, and M. Miller, "3-D brain mapping using a deformable neuroanatomy", *Phys. Med. Biol.*, **39**, pp. 609-618, 1994.
9. J. Cappelletti and A. Rosenfeld, "Three-dimensional boundary following", *Computer Vision Graphics and Image Processing*, **48**, pp. 80-92, 1989.
10. U. Montanari, "On the optimal detection of curves in noisy pictures", *Communications of the ACM*, **14**, pp. 335-345, 1971.
11. A.X. Falcão, J. K. Udupa, S. Samarasekera, and S. Sharma, "User-steered image segmentation paradigms: live wire and live lane", *Graphical Models Image Processing*, **60**, pp. 233-260, 1998.
12. N. Otsu, "A threshold selection method from gray-level histogram", *IEEE Transactions on Systems, Man and Cybernetics*, **9**, pp. 62-66, 1979.
13. T. Hong and A. Rosenfeld, "Compact region extraction using weighted pixel linking in a pyramid", *IEEE Transactions on Pattern Analysis and Machine Intelligence*, **6**, pp. 222-229, 1984.
14. H. Soltanian-Zadeh, J. Windham, and D. Peck, "A comparative analysis of several transformations for enhancement and segmentation of magnetic images", *IEEE Transactions on Medical Imaging*, **11**, pp. 302-318, 1992.
15. J. K. Udupa, L. Wei, S. Samarasekera, Y. Miki, M. A. van Buchem, and R. I. Grossman, "Multiple sclerosis lesion quantification using fuzzy connectedness principles", *IEEE Transactions on Medical Imaging*, **16**, pp. 598-609, 1997.
16. S. Samarasekera, J. K. Udupa, Y. Miki, and R. I. Grossman, "A new computer-assisted method for enhancing lesion quantification in multiple sclerosis", *Journal of Computer Assisted Tomography*, **21**, pp. 145-151, 1997.
17. M. Phillips, R.I Grossman, Y. Miki, L. Wei, D. L. Kolson, M.A. van Buchem, M. Polansky, J. C. McGowan, and J. K. Udupa, "Comparison of T2 lesion volume and magnetization transfer ratio histogram analysis and atrophy and measures of lesion burden in patients with multiple sclerosis", *ANJR American Journal of Neuroradiology*, **19**, pp. 1055-1060, 1998.
18. J. K. Udupa, D. Odhner, J. Tian, G. Holland, and L. Axel, "Automatic clutter-free volume rendering for MR angiography using fuzzy connectedness", *SPIE Proceedings*, **3034**, pp. 111-119, 1997.
19. J. K. Udupa, J. Tian, D. Hemmy, and P. Tessier, "A pentium PC-based craniofacial 3D imaging and analysis system", *Journal of Craniofacial Surgery*, **8**, pp. 333-339, 1997.
20. P. K. Saha and J. K. Udupa, "Scale-based fuzzy connectivity: a novel image segmentation methodology and its validation" *SPIE Proceedings*, **3661**, (in press), 1999.
21. J. K. Udupa, and D. Odhner, "Shell rendering", *IEEE Computer Graphics and Applications*, **13**, pp. 58-67, 1993.

22. J. K. Udupa, D. Odhner, S. Samarasekera, R. Goncalves, K. Iyer, K. Venugopal, and S. Furie. "3DVIEWNIX: An open, transportable, multidimensional, multimodality, multiparametric imaging software system. *SPIE Proceedings* 2164, pp. 58-73, 1994.

Clutter-Free Volume Rendering for Magnetic Resonance Angiography Using Fuzzy Connectedness

Bowen L. Rice, Jr.,¹ Jayaram K. Udupa²

¹ Department of Electrical and Computer Engineering, Drexel University, Philadelphia, Pennsylvania

² Medical Image Processing Group, Department of Radiology, University of Pennsylvania, 423 Guardian Drive, 4th Floor Blockley Hall, Philadelphia, PA 19104-6021. E-mail: jay@mipg.upenn.edu

ABSTRACT: The purpose of this paper is to describe a practical method for the clutter-free, three-dimensional (3D) volume rendering of magnetic resonance angiographic (MRA) data. In MRA, clutter due to artifacts or nearby high-intensity structures prevents clear visualization of the vessel under investigation. We offer an alternative to the manual editing that is commonly used to remove clutter. The method is near automatic and requires the user to point at structures on a 3D maximum intensity projection (MIP) display. It utilizes recently developed fuzzy connected object delineation algorithms to extract the vessels of interest. Because the resulting definition is nonbinary, it can be displayed via MIP or more sophisticated volume-rendering techniques. The improved renditions are illustrated with several MRA studies. Implementation of the fuzzy connectedness method proved to be effective in removing the associated clutter in the images and, in some cases, dramatically improving visibility. Additionally, vessels could be extracted with a nominal number of points selected within the object by the user that retained most of the information present in the conventional MIP display. This could all be performed in a practical time frame: the first vessel delineation in 30 s, subsequent delineations in 2–10 s per view, all on a 100-MHz Pentium PC. Automatic delineation of vessels for 3D MRA visualization is feasible via fuzzy connectedness principles. The method retains the original intensity constitution, an advantage of the MIP method, and mostly eliminates the clutter commonly observed in MIP. Its speed and effectiveness make it feasible for routine clinical use. © 2000 John Wiley & Sons, Inc. *Int J Imaging Syst Technol*, 11, 62–70, 2000

I. INTRODUCTION

Magnetic resonance angiography (MRA) is a relatively recent development (compared to X-ray angiography). It has better sensitivity for the detection of vascular abnormalities, such as aneurysms, than routine magnetic resonance imaging (MRI). MRA methods are based on the same principles as flow quantitation techniques: time-of-flight (TOF) and phase-sensitive principles. Regardless of the specific techniques used to image the flowing blood, it is necessary to isolate the vascular system from the surrounding stationary tissues (Stark and Bradley, 1992). In MRA, a major concern is to distinguish the vessel in question from the additional clutter introduced by

artifacts. For the three-dimensional (3D) display of MRA data, maximum intensity projection (MIP) is the most commonly used technique (Stark and Bradley, 1992; Mistretta, 1993; Owen et al., 1993; Prince et al., 1995; Napel et al., 1992; Bluemke and Chambers, 1995). In MIP, the intensity (shading) assigned to a pixel in the rendered picture represents the maximum of the intensities of the voxels in the input volume image along a line from the pixel that is orthogonal to the picture plane. The high-intensity points in space are projected to generate a MR angiogram. Although this is conceptually and computationally a simple technique, it has several drawbacks. These include the presence of clutter in display, lack of information about structural juxtaposition and constitution, the creation of irregular depth cues, and the lack of a sense of the real size of objects. A limitation of the method is the lack of selectivity because every signal intense structure in the selected volume is depicted (Welte et al., 1996). Nonvascular high-intensity patterns are caused due to artifacts during MRI (e.g., susceptibility artifacts, inhomogeneities of the RF fields). Furthermore, projections from different orientations do not necessarily contain the same objects (as they may or may not be obscured by another object). The MIP procedure along a projection ray path is commutative, i.e., two MIP images computed 180° apart are equivalent. Each MIP image thus has two equally valid perspectives (correct and mirrored) so that one can only guess at the true image orientation (Verdonck, 1996).

Clutter appears in MIP displays either due to high-intensity artifacts, such as those stemming from surface coils, or to uninteresting vessels. Creation of clutter-free MIP displays has remained a challenge in tomographic angiography mainly because the problem originates in the difficult task of image segmentation. The successful solutions to this problem have invariably involved some form of slice-by-slice help from a human operator in defining the region of the vessel in the given volume image (Shiffman et al., 1996).

The lack of information about juxtaposed structures (e.g., as to which vessel is in front) in MIP displays is due to the lack of any structure shading in the MIP method. Objects such as plaques and calcifications usually have a graded constitution. MIP cannot capture this information in its displays. Because of this, various techniques have been developed. Such techniques include TOF and phase-contrast (PC) MRA. In both of these cases, these methods produce a projected image similar to a conventional angiogram. However, for analysis, both the projection and the individual slices that make

Correspondence to: Jayaram K. Udupa
Contract grant sponsor: NIH; Contract grant number: NS37172; Contract grant sponsor: Department of the Army; Contract grant number: DAMD 179717271.

up the image must be used (Shiffman et al., 1996; Atlas et al., 1997). Sophisticated rendering strategies that account for reflection, transmission, and emission through various fuzzy interfaces through the vasculature are needed for this purpose.

In an attempt to overcome some of the above problems, we have devised an approach of vessel definition and rendering based on a recently developed concept of fuzzy connectedness (Udupa and Samarasekera, 1996). In this strategy, an object (such as a vascular tree) is considered to be a fuzzy entity where the object elements (voxels) "hang together" with varying degrees of strength. The concept and the associated algorithms have been effectively applied quite extensively to MRI segmentation of the brain (Udupa et al., 1997a, b; Samarasekera et al., 1997; Miki et al., 1997, 1998; Phillips et al., 1998) and computed tomographic (CT)-based craniofacial applications (Udupa et al., 1997a, b). In this paper, we explore their effectiveness for the clutter-free display of vessels in MRA data. Their adaptation for MRA is different from that for these other applications. This consists of two steps: fuzzy object definition and rendering. These are described in detail in the next section.

II. METHODS

A. Fuzzy Connected Vessel Definition. The fuzzy connected object definition concepts (Udupa and Samarasekera, 1996) are applicable to n -dimensional images. Because our application of these ideas focuses on 3D MRA images, the description here will be for 3D volume images. We think of a 3D volume image I as a pair $I = (V, f)$ where V is a 3D array of voxels, and for any voxel v in V , $f(v)$ represents the image intensity. On the 3D grid system defined by the 3D voxel array V in a given 3D volume image I , we define a fuzzy adjacency relation α . It assigns to every pair (u, v) of voxels in V a degree $\mu_\alpha(u, v)$ of adjacency between them. This relation α is intended to be a local phenomenon for capturing the blurring property of the imaging device.

Now we think of the given volume image I as being defined over this fuzzy grid system. We define over this fuzzy grid system another fuzzy relation, called fuzzy affinity κ , on V , that assigns a degree of affinity $\mu_\kappa(u, v)$ to every pair (u, v) of voxels in V . This relation is also local, but it takes into account how close u and v are spatially as well as in their image intensities, $f(u)$ and $f(v)$, and possibly also in their image-derived properties such as the magnitude of the image intensity gradient. For MRA, we devised the following fuzzy affinities. These were arrived at after extensive experimentation within our software framework (Udupa et al., 1994), which allows combining several image-derived properties including the original intensities to define affinities. We associate two "features," denoted $\phi_1(u, v)$ and $\phi_2(u, v)$, with every pair of voxels in any volume image $I = (V, f)$ as

$$\phi_1(u, v) = \max(f(u), f(v)), \quad (1)$$

$$\phi_2(u, v) = |f(u) - f(v)|. \quad (2)$$

The affinity, $\mu_\kappa(u, v)$, between u and v based on ϕ_1 and ϕ_2 and μ_α is given by

$$\mu_\kappa(u, v) = \mu_\alpha(u, v) \left\{ \prod_{i=1}^2 \left(0.5 + 0.5 t_i \left(\frac{(\phi_i(u, v) - m_i)}{\sigma_i} \right) \right) \right\} \quad (3)$$

where

$$\mu_\alpha(u, v)$$

$$= \begin{cases} 1, & \text{if } u \text{ and } v \text{ differ in at most one coordinate by 1,} \\ 0, & \text{otherwise,} \end{cases} \quad (4)$$

$$t_1(x) = \begin{cases} x + \frac{1}{2}, & \text{if } -\frac{1}{2} \leq x \leq \frac{1}{2}, \\ 0, & \text{if } x < -\frac{1}{2}, \\ 1, & \text{if } x > \frac{1}{2}, \end{cases} \quad (5)$$

and

$$t_2(x) = e^{-2x^2}. \quad (6)$$

The idea behind the above affinity relation is the following. If $u \neq v$ and u and v do not share a voxel face, their affinity is 0. Otherwise, their affinity depends on both the larger of the two intensities, denoted $\phi_1(u, v)$, and their difference, $\phi_2(u, v)$, as per the function in Eq. (3). The smaller the difference and the greater the larger value, the greater is the affinity. There are altogether four parameters, m_1 , σ_1 , m_2 , σ_2 , that characterize the affinity. These parameters are determined via "training." The operator "paints" some typical vessel regions in a display of one slice of the volume image using the mouse cursor. The software subsequently determines the mean and standard deviation of the features ϕ_1 and ϕ_2 within this region. The value of m_1 is set to the mean for ϕ_1 , and σ_1 is set to roughly four times the computed standard deviation. (The logic behind this is that with two standard deviations on either side of the mean, we would capture roughly 97% of the samples in a Gaussian distribution. Under this distribution, therefore, most of the painted region will be included with nonzero affinity.) The value for m_2 is set to 0, and for σ_2 , four times the standard deviation for ϕ_2 . Note that the training to learn the parameters is needed in only in one slice. More regions may be painted, but this is not necessary.

Our aim is to define a 3D object, such as a vascular tree, as a fuzzy connected entity. This is facilitated through another fuzzy

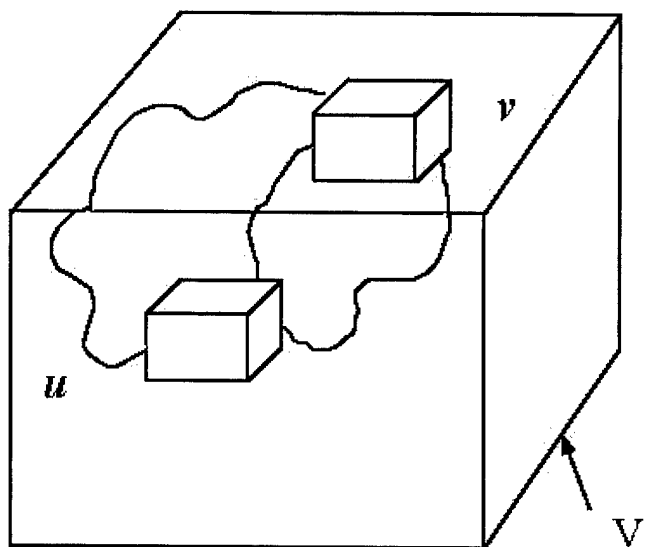


Figure 1. In determining a fuzzy connected object, the strength of all paths between all pairs of voxels (such as u, v) is considered.

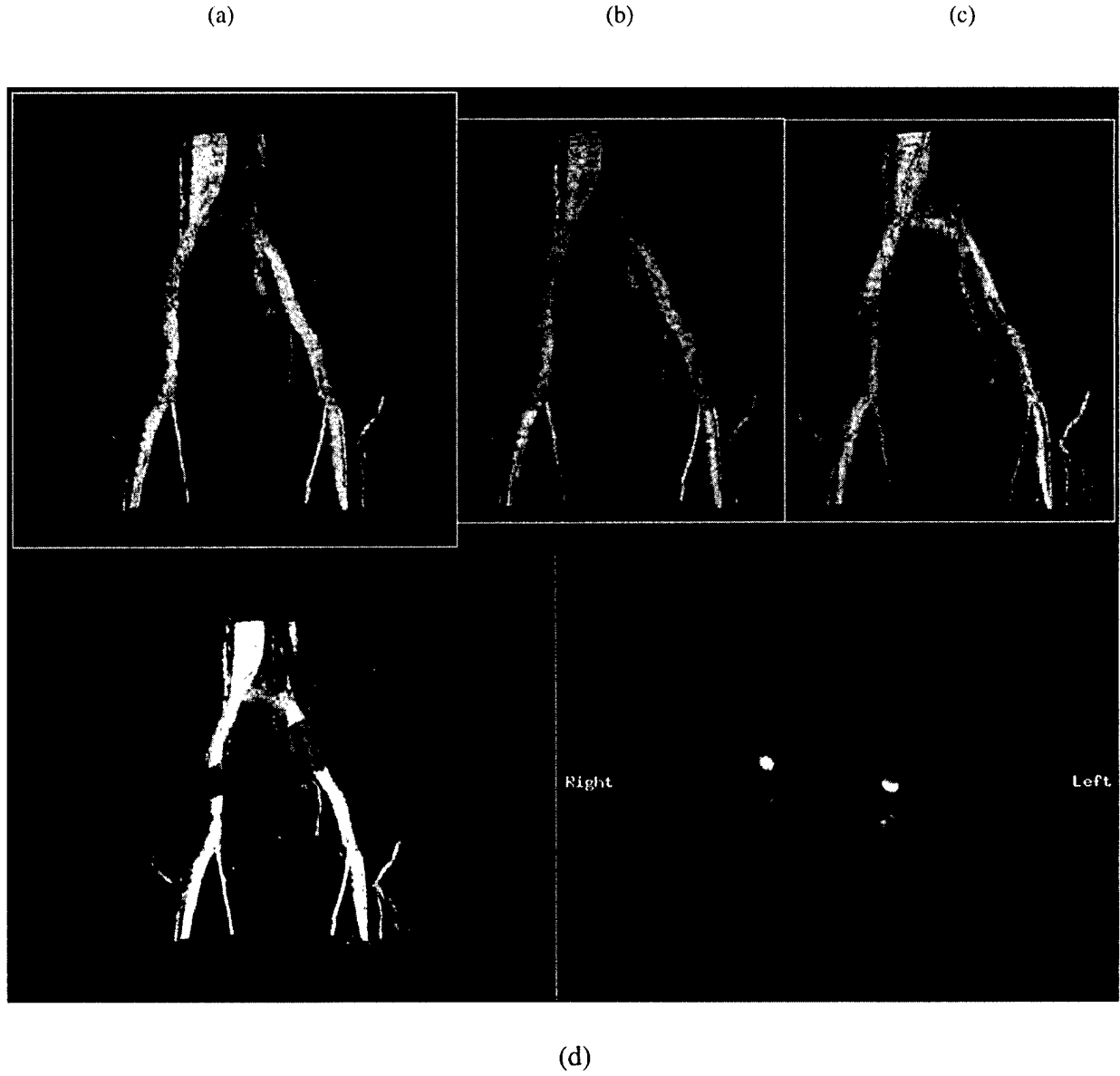


Figure 2. (a) MIP display of a body shell. (b) MIP display of the fuzzy connected vessels extracted from the body shell depicted in (a). (c) A volume rendition of the fuzzy connected vessels. (d) Interactive slice selection guided by an MIP display. The MRI corresponding to the depicted slice is displayed.

relation defined on V , called fuzzy connectedness, K . This is a global phenomenon as compared to α and κ . The strength of connectedness, $\mu_K(u, v)$, between any two voxels u and v is determined as follows. There are many possible paths between u and v , where each path is a sequence of nearby voxels starting from u and ending on v . Figure 1 shows three paths among the possible paths between u and v . Each path has a strength associated with it, which is simply the smallest of the affinities between successive voxels in the path. Finally, the strength of connectedness $\mu_K(u, v)$ between u and v is the largest of the strengths of all paths between u and v .

A fuzzy object of strength x is a pool of voxels (together with their strength values) such that, between any two voxels u and v in the pool, the strength of connectedness $\mu_K(u, v) \geq x$, whereas between any two voxels v and w such that u is in the pool and w is

not, the strength $\mu_K(u, v) < x$. Typically, a small value of x , no greater than 0.1, is adequate to separate the object from the rest of the image.

For completeness, we present one algorithm for fuzzy connected object tracking. More details on the algorithm and other algorithms and the analysis of their behavior can be found in Udupa and Samarasekera (1996). This algorithm takes as input an MRA volume image $I = (V, f)$, a voxel o specified in the vessel region, affinity κ (as defined in Eqs. 1–6), and a threshold x . Its output is a fuzzy object O represented as a volume image $O = (V, f_o)$, such that for any voxel v in the pool corresponding to the fuzzy object, $f_o(v) = f(v)$, and $f_o(v) = 0$ if v is not in the pool. The algorithm uses a queue Q and the volume image O as auxiliary data structures. It is a slightly modified version of algorithm $\kappa x FOE$ of (Udupa and Samarasekera, 1996).

ALGORITHM κ xBFT

```

begin
  set  $f_o(c) = 0$  for all voxels  $c$  of  $V$ ;
  initialize queue  $Q$  to contain just  $o$ ;
  mark  $o$ ;
repeat
  dequeue a voxel  $q$  from  $Q$ ;
  for each unmarked 6-neighbor  $w$  of  $q$  do
    if  $\mu_\kappa(q, w) \geq x$  then
      mark  $w$ ;
      enqueue  $w$  on  $Q$ ;
    endif;
  endfor;
until  $Q$  is empty;
for each marked voxel  $c$  do
  set  $f_o(c) = f(c)$ ;
endfor;
end

```

B. Fuzzy Object Rendering. The underlying rendering principle is based on a method called shell rendering (Udupa and Odhner, 1993). In shell rendering, potentially every voxel v in I contributes to the rendered picture. This contribution is influenced in three ways: (1) reflection of light from v depending on the strength of the surface contained in v , (2) emission depending on the degree of object membership of v , and (3) attenuation depending on the opacity assigned to v . The shell rendering concept allows a continuum from only reflection-based hard surface rendering to a variety of degrees of translucent renditions that mix reflection, emission, and transmission in different proportions.

A shell is a data structure that allows rapid rendering of fuzzy objects by retaining only those voxels in its representation that make nonnegligible contribution to the rendered picture. With each voxel, several other items of information are stored, including the voxel's degree of membership in the object, the magnitude of the gradient at the voxel computed from the given volume image, and the direction of the gradient. In MRA, for example, the voxels outside the body and even those far away from the vessel boundary need not be stored in the shell. However, before the vessels are actually detected, we cannot be sure as to which voxels inside the body do not belong to the vessels. Therefore, we first create a shell that stores only the voxels that are inside the body, together with their descriptions. These voxels are easily identified by thresholding. For further reference, we will call this a body shell. This shell is created automatically without loss of any relevant information when the image data are transferred from the MR scanner to the viewing workstation via our picture archiving and communication system.

We then create an MIP display of the body shell, with 3D orientation selections under user control. We utilize this display, although cluttered, to guide the user in selecting the vessel structures that need to be extracted from the body shell. This selection is done by pointing the cursor at a vessel structure and clicking the mouse button. By this action, the user specifies a voxel in the array V . This specification is made possible by storing the coordinates of the maximum intensity voxel that contributed to the rendition. Several such voxels may be specified. Typically, a voxel should be specified for each separate vessel structure that is either not connected to or loosely connected to other structures for which voxels have already been specified. Once this specification is completed and the process

to detect fuzzy connected objects is initiated, the fuzzy connected objects containing the specified voxels are first detected using algorithm κ xBFT. These are then converted to a shell representation and then displayed using MIP.

C. Image Data. We utilize five patient MRA data sets to demonstrate the effectiveness of the fuzzy connected object detection and rendering methods. These data sets were acquired as a stack of rapid 2D gradient echo images using TOF effects to produce vessel images brighter than adjacent stationary structures. The matrix size was 256×256 , with the number of slices varying between 86 and 140. The voxel sizes in these data sets ranged from $1.02 \times 1.02 \times 3$ mm to $1.17 \times 1.17 \times 3$ mm.

All algorithms were implemented within the 3DVIEWNIX software system (Udupa et al., 1994) and all experiments were performed using this system.

III. RESULTS

The implementation of the methods has been optimized for routine interactive use in the clinical vascular imaging section. In a routine use, the following steps are involved. The timings reported are all for a 100-MHz Pentium PC with 256 MB RAM.

- Step 1:** The image data are transferred to the workstation and the body shell is created simultaneously and automatically. This typically takes 1 min.
- Step 2:** MIP display of the body shell is rendered. This takes 5–10 s per view. Figure 2(a) gives an example.
- Step 3:** One or more points are specified on the vessels in this MIP display. A fuzzy connected object of a specified strength x (chosen on a slider) containing the points is extracted and rendered using MIP display. This operation takes 20 s. Figure 2(b) shows the fuzzy connected vessels extracted from the body shell in Figure 2(a).
- Step 4:** If more vessels are to be selected, additional points are specified. Subsequently, the fuzzy connected object containing all points specified so far is extracted and rendered via MIP. This step takes about 2–5 s.
- Step 5:** The fuzzy connected vessel structure is visualized at a fraction of a second per view via MIP or more sophisticated volume rendering that takes into account transmission, reflection, and emission. Figure 2(c) shows such a rendition of the vessels in Figure 2(b).
- Step 6:** For a closer scrutiny of selected regions in the vessel, cut planes of arbitrary orientation are interactively selected and stepped along vessels to determine the image intensity values on those planes. Figure 2(d) illustrates this operation. The operation takes 5–10 s the first time and subsequently about 1–2 s.

Figure 3 shows different renditions of the five data sets. The rows correspond to the different data sets. The first column shows MIP renditions of the five body shells. The second column shows MIP renditions of the fuzzy connected vessels extracted from the body shells. All data sets required one to three points to extract the vessels shown.

IV. DISCUSSION

As seen from all patient study examples, fuzzy connected vessel definition is remarkably effective in removing the clutter, with a dramatic improvement in visibility in some cases. Most of the vessels seen in the MIP rendition of the body shell are included in

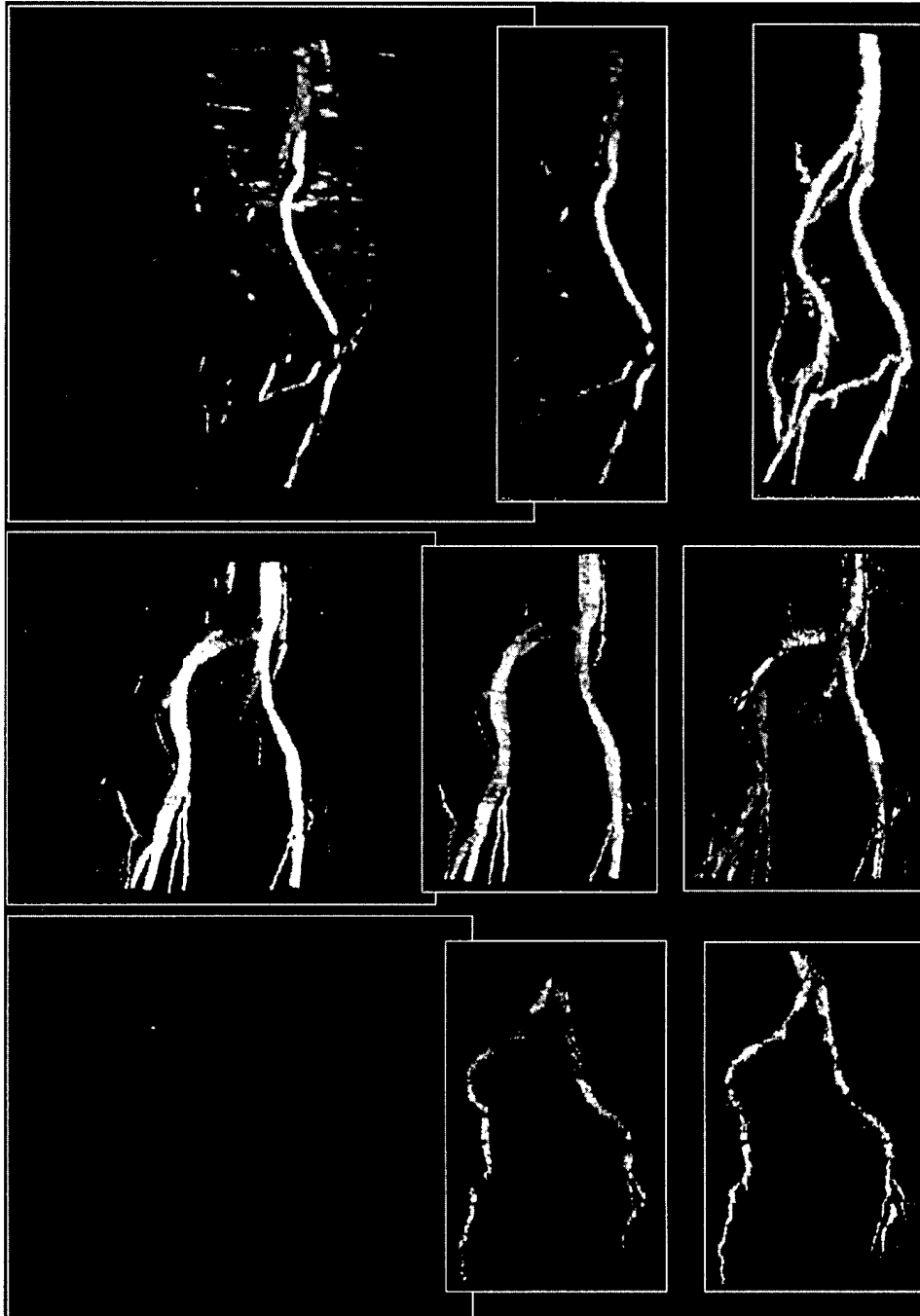


Figure 3. Column 1: MIP renditions of the body shells of the five data sets. Column 2: MIP renditions of the fuzzy connected vessels extracted from the body shells. Column 3: Volume rendering of the fuzzy connected vessels.

the fuzzy connected object. We emphasize that in the fuzzy connected objects, all original MR intensity values that matter (namely, those in the vessels) are retained in the fuzzy connected object. In order to test the validity of this claim, an operator outlined the major vessel regions in every slice for three among the five studies (shown in columns 1, 2, and 3 in Fig. 3). Denoting the set of voxels defined in this fashion for a study by X_i , we computed the fraction $(|X_i - X_f|/|X_i|) \times 100$, where X_f denotes the set of voxels determined by the algorithm to be in the fuzzy object (i.e., with strength of

connectedness $\geq x$) for the same study. Here $|\cdot|$ denotes the cardinality of the set. $|X_i - X_f|$ represents the number of voxels in X_i that are not in X_f . Clearly, the extreme values of this fraction are 0 and 100, assuming that $|X_i| \neq 0$ for the study. The values of this fraction for the three studies were 0.1487, 0.2201, and 0.3174.

The most time-consuming step in our approach after creating the body shell is the first fuzzy connected vessel definition step, requiring about 20 s. The computations involved in algorithm $\kappa x BFT$ are both computation and memory intensive. With 64 MB RAM (as

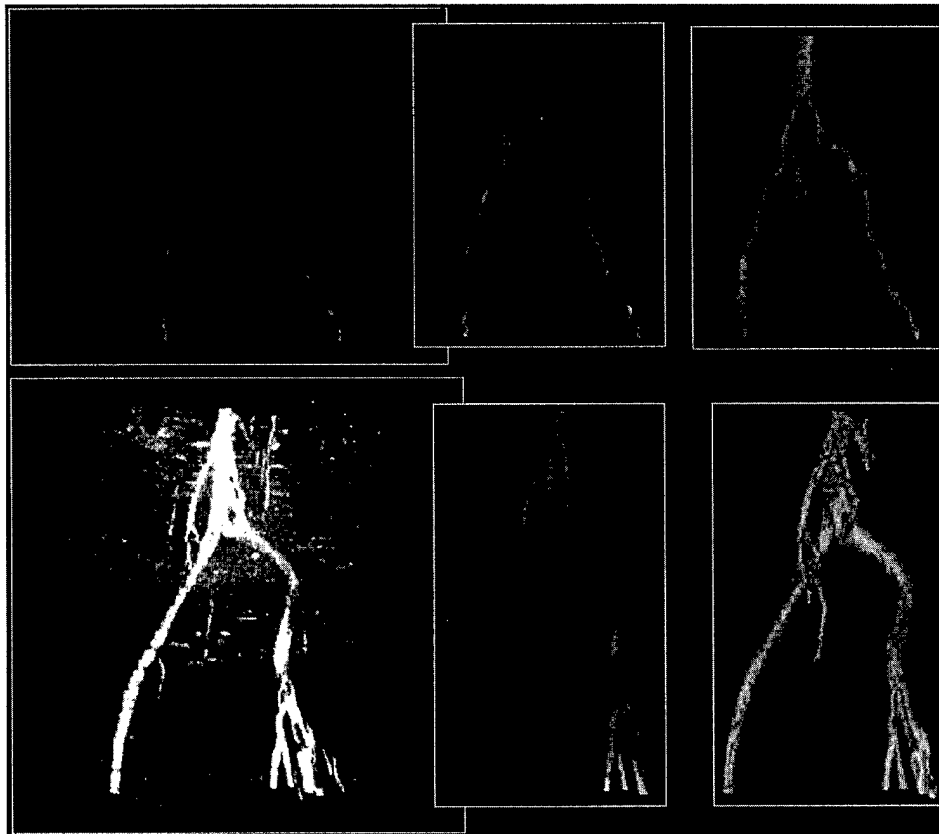


Figure 3. (Continued)

opposed to 256 MB), the time requirement for this jumps to 2 min, becoming noninteractive and unsuitable in a clinical vascular imaging setting. Interestingly, on a 300-MHz Pentium PC (running under Linux) with 256 MB RAM, all operations described in Steps 1–6 ran at interactive speeds. This is particularly relevant to the cost-conscious health care environment considering how inexpensive the Pentium PCs are today.

Volume-rendering operations that take into account transmission, emission, and reflection allow more flexibility for portraying the heterogeneity of MR signal intensities in the vessels than the MIP method. MIP rendering does not portray the geometric relationships among and the shapes of the vessels properly because of the lack of shading coming from the above components. This is demonstrated in Figures 4(a)–(d), which show an MIP rendition of a fuzzy connected vessel and its three volume renditions at different combinations of the three properties. Note how the heterogeneity of MR image intensities comes through in the displays, especially in Figure 4(d). The extra computational time (1–2 s) for such renditions over MIP for vessels is negligible.

One possible disadvantage of fuzzy connected MIP and volume rendering over direct MIP rendering of the body shell is that the contextual information coming from the faintly portrayed body contour in the latter display is lacking in the former. Such information is potentially useful in providing constantly an orientation to the viewer for extremely unfamiliar viewing directions. The body surface information is easily grafted into the fuzzy connected renditions by segmenting the body at the threshold at which the body shell was

created and by merging the shells corresponding to the body surface obtained in this fashion and the fuzzy connected vessels. Figure 5(b) illustrates a volume rendition of a composite shell obtained in this fashion. Figure 5(a) shows, for comparison, an MIP rendition of the original body shell.

There is no guarantee in our system that with a single seed, all aspects of the vessels depicted in the MIP rendition are delineated by the fuzzy connectedness method. To include vessels that are left out, the user simply has to select more seed points in such vessels in subsequent stages after verifying the resulting shell renditions, as described in Step 4.

We have not tested the system specifically for its ability to detect stenosis better than in the original MIP renditions. This requires further work involving observer studies and comparison with X-ray angiography. However, as indicated by our experiment comparing manual tracing, our method loses less than 0.5% of the voxels identified by an operator. This, combined with the fact that our method retains all original intensity information, indicates that the MIP renditions of the delineated vessels contain almost all the information contained in the original MIP renditions minus the clutter. The proof of this claim requires further validation.

The fuzzy objects delineated by our method may be utilized for measuring vessel diameters. Such tools already exist in 3DVIEW-NIX. However, these measurements need to be carefully calibrated to ensure that they agree with truth. We have not done this testing in this work.

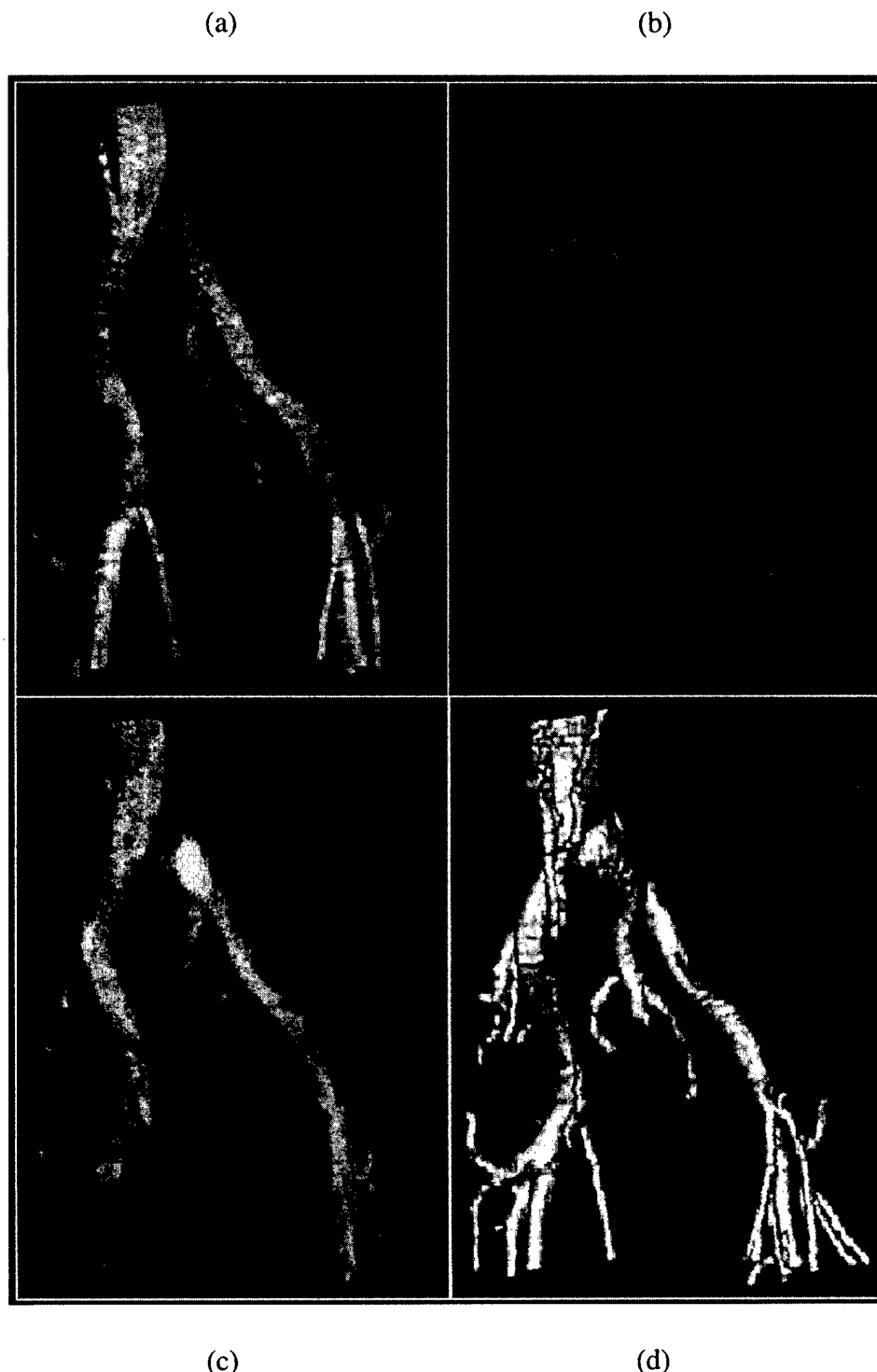


Figure 4. MIP rendition of a fuzzy connected vessel (a) and its volume renditions (b-d) at different high settings of transmission (b), emission (c), and reflection (d).

V. CONCLUDING REMARKS

We have presented an approach and a system for removing clutter in MRA with minimal user effort as an alternative to the slice-by-slice removal of obscuration that is currently practiced. The approach is based on a theory of fuzzy connectedness of object regions that

utilizes information from all connecting paths between all possible pairs of voxels. We have demonstrated that the approach is practically viable, requiring less than 15 s for all operations and less than 4 s for all rendering operations on a 300-MHz Pentium PC. We have not carried out rigorous evaluation studies for specific clinical tasks

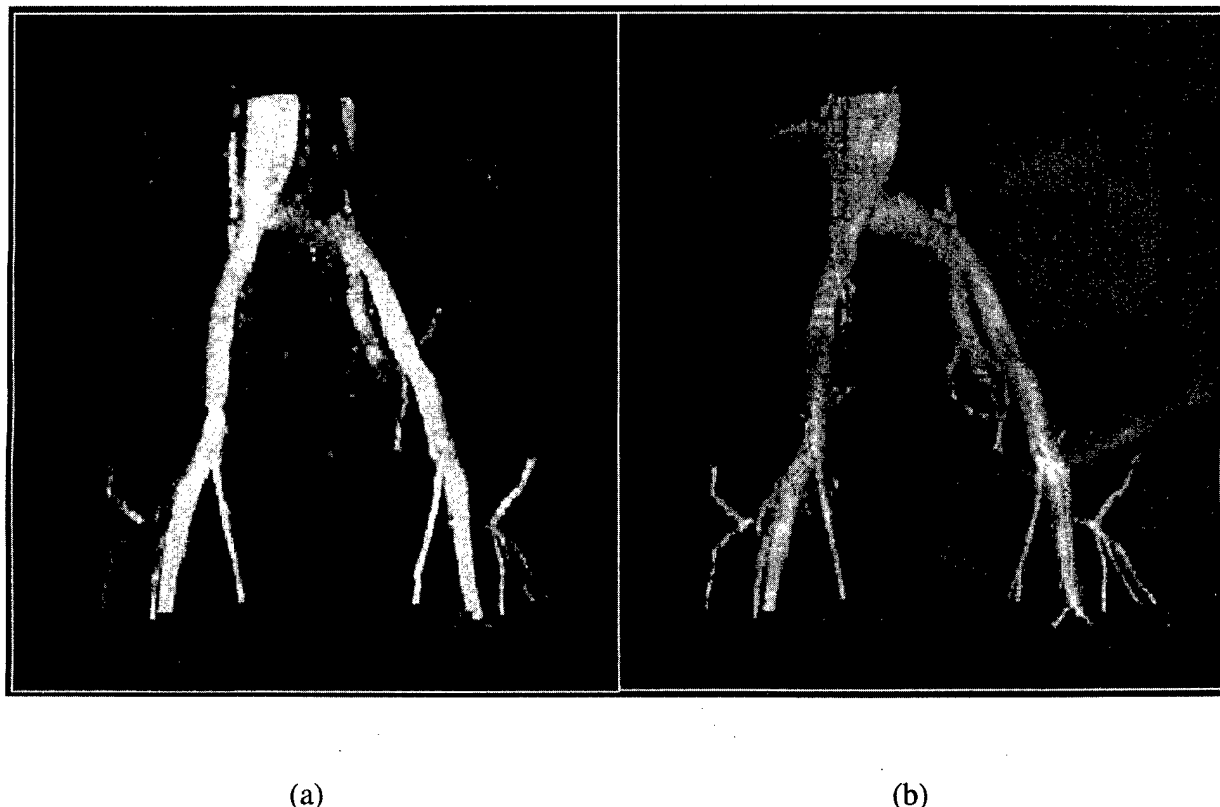


Figure 5. (a) MIP rendition of the body shell of an MRA data set. (b) A combined display via volume rendering of the body surface and fuzzy connected vessels extracted from the body shell in (a).

comparing the MIP method commonly used in clinical MRA today with the proposed fuzzy connected strategies. However, we have presented evidence based on five clinical studies that the proposed method, at the least, retains most of the information present in the conventional MIP display, removes most of the obscuring clutter, and possibly portrays this information better than conventional MIP. Although we have not experimented with CT angiography, we believe that the approach presented here is applicable to CT angiography for separating vessels from high-intensity structures, such as bones. We are currently investigating ways to separate arteries and veins in MRA images using fuzzy connectedness principles.

ACKNOWLEDGMENTS

The authors are grateful to Drs. George Holland and Leon Axel for the MRA data sets.

REFERENCES

S.W. Atlas, L. Sheppard, H.I. Goldberg, R.I. Hurst, J. Listerud, and E. Flamm, Intracranial aneurysms: Detection and characterization with MR angiography with use of an advanced post-processing technique in a blinded-reader study, *Radiology* 203 (1997), 807–814.

D. Bluemke and T. Chambers, Spiral CT angiography: An alternative to conventional angiography (editorial comment), *Radiology* 195 (1995), 317–319.

Y. Miki, R.I. Grossman, S. Samarasekera, J.K. Udupa, M.A. van Buchem, B.S. Cooney, S.N. Pollack, D.K. Kolson, M. Polansky, and L.J. Mannon, Clinical correlation of computer assisted enhancing lesion quantification in multiple sclerosis, *Am J Neuroradiol* 18 (1997), 705–710.

Y. Miki, R.I. Grossman, J.K. Udupa, L. Wei, D.L. Kolson, and L.J. Mannon, Isolated U-fiber involvement in multiple sclerosis and its quantification, *Neurology* 50 (1998), 1301–1306.

C. Mistretta, Relative properties of MR angiography and competing vascular modalities, *J Magn Reson Imaging* 3 (1993), 685–698.

S. Napel, M. Marks, and G. Rubin, CT angiography with spiral CT and maximum intensity projection, *Radiology* 185 (1992), 607–610.

R. Owen, R. Baum, J. Carpenter, G. Holland, and C. Cope, Symptomatic peripheral vascular disease: Selection of imaging parameters and clinical evaluation with MR angiography, *Radiology* 187 (1993), 627–635.

M. Phillips, R.I. Grossman, Y. Miki, L. Wei, D.L. Kolson, M.A. van Buchem, M. Polansky, and J.K. Udupa, Correlation of T2 lesion volume and MTR histogram analysis with atrophy in multiple sclerosis, *Am J Neuroradiol* 19 (1998), 1055–1060.

M. Prince, D. Narasimhan, J. Stanley, T. Chenevert, D. Williams, M. Marx, and K. Cho, Breathhold gadolinium-enhanced MR angiography of the abnormal aorta and its major branches, *Radiology* 197 (1995), 785–792.

S. Samarasekera, J.K. Udupa, Y. Miki, and R.I. Grossman, A new computer-assisted method for enhancing lesion quantification in multiple sclerosis, *J Computer Assist Tomogr* 21 (1997), 145–151.

S. Shiffman, G. Rubin, and S. Napel, Semi-automated editing of computed tomography sections for visualization of vasculature, *Proc SPIE* 2707 (1996), 140–151.

D.D. Stark and W.G. Bradley, Jr. (Editors), *Magnetic resonance imaging* (2nd ed.), Mosby, St. Louis, 1992, pp. 290–296.

J. Udupa and D. Odhner, Shell rendering, *IEEE Computer Graphics Appl* 13 (1993), 58–67.

J.K. Udupa, D. Odhner, S. Samarasekera, R. Goncalves, K. Iyer, K. Venugopal, and S. Furui, “3DVIEWNIX: An open, transportable, multidimensional, multimodality, multiparametric imaging and software system. *Proc SPIE* 2164 (1994), 58–73.

J.K. Udupa and S. Samarasekera, Fuzzy connectedness and object definitions: Theory, algorithms and applications in image segmentation, *Graphic Models Image Process* 58 (1996), 246–261.

J.K. Udupa, J. Tian, D.C. Hemmy, and P. Tessier, A pentium-based craniofacial 3D imaging and analysis system, *J Craniofac Surg* 8 (1997a), 333–339.

J.K. Udupa, L. Wei, S. Samarasekera, Y. Miki, M.A. van Buchem, and R.I. Grossman, Multiple sclerosis lesion quantification using fuzzy connected principles, *IEEE Trans Med Imaging* 16 (1997b), 598–609.

P. Verdonck, Blood vessel segmentation, quantification and visualization for 3D MR spiral CT angiography, *Telecom*, Paris, 1996.

D. Welte, D. Petersen, U. Klose, and T. Grunert, Segmentation and selective 3D-visualization of cerebral vessels from MRA data, *Int Soc for Magnetic Resonance in Medicine, Fourth Scientific Meeting and Exhibition*, 1996, p. 1611.



Multiprotocol MR image segmentation in multiple sclerosis: experience with over 1000 studies

Jayaram K. Udupa^a, László G. Nyúl^a, Yulin Ge^a, Robert I. Grossman^b

^aMedical Image Processing Group, Department of Radiology
University of Pennsylvania, 423 Guardian Drive - Fourth Floor Blockley Hall
Philadelphia, PA 19104-6021

^bDepartment of Radiology-Neuroradiology Division
3400 Spruce Street - Ground Floor Founders
Philadelphia, PA 19104-4283

ABSTRACT

Multiple Sclerosis (MS) is an acquired disease of the central nervous system. Subjective cognitive and ambulatory test scores on a scale called EDSS are currently utilized to assess the disease severity. Various MRI protocols are being investigated to study the disease based on how it manifests itself in the images. In an attempt to eventually replace EDSS by an objective measure to assess the natural course of the disease and its response to therapy, we have developed image segmentation methods based on fuzzy connectedness to quantify various objects in multiprotocol MRI. These include the macroscopic objects such as lesions, the grey matter (GM), white matter (WM), cerebrospinal fluid (CSF), and brain parenchyma as well as the microscopic aspects of the diseased WM. Over 1000 studies have been processed to date. By far the strongest correlations with the clinical measures were demonstrated by the Magnetization Transfer Ratio (MTR) histogram parameters obtained for the various segmented tissue regions emphasizing the importance of considering the microscopic/diffused nature of the disease in the individual tissue regions. Brain parenchymal volume also demonstrated a strong correlation with the clinical measures indicating that brain atrophy is an important indicator of the disease. Fuzzy connectedness is a viable segmentation method for studying MS.

Keywords: Image segmentation, Multiple Sclerosis, MR imaging, fuzzy connectedness.

1. INTRODUCTION

MS is an acquired disease of the central nervous system (CNS) characterized primarily by multifocal inflammation and destruction of myelin. Inflammation and edema are accompanied by different degrees of demyelination and destruction of oligodendrocytes, and may be followed by remyelination, axonal loss and/or gliosis. The disease was first characterized by Charcot¹ and has since been investigated extensively. The highest frequency of MS occurs in northern and central Europe, Canada, the USA, and New Zealand and South of Australia.² In the US, it affects approximately 350,000 adults and stands out as the most frequent cause of non-traumatic neurologic disability in young and middle-aged adults.³ In its advanced state, the disease may severely impair the ambulatory ability and may even cause death.

MS is usually classified into three subtypes: (1) Relapsing-remitting (RR): Clearly defined disease relapses with full recovery, or with sequelae and residual deficit upon recovery, but there is no disease progression between relapses. (2) Secondary-progressive (SP): Initial RR disease course followed by gradual progression with or without occasional superimposed relapses. (3) Chronic-progressive (CP): Gradual progression from the onset with occasional plateaus and temporary minor improvements. The most commonly used scale to clinically measure disease progression in MS is the Expanded Disability Status Scale (EDSS) introduced by Kurtzke.⁴ This scale extends from 0 to 10, and is based on the functional systems (visual, brainstem, pyramidal, cerebellar, sensory, bowel/bladder, and cerebral) in the lower scores, and on ambulation in the higher scores. The clinical quantification of disease severity is subjective and sometimes equivocal. The development of new treatments demands objective outcome measures for relatively short trials. Therefore, MR imaging has

* Correspondence: Email: jay@mipg.upenn.edu; Telephone: (215) 662-6780; Fax: (215) 898-9145.

become one of the most important paraclinical tests for diagnosing MS and in monitoring disease progression in MS. As described in the rest of this section, a variety of MRI protocols have been utilized in understanding this disease.

1.1. T2-weighted imaging (T2WI)

The sensitivity of T2WI in the detection of MS has long been recognized.^{5, 6} MS lesions appear hyperintense in T2WI. The clinical course of MS is mainly defined by the "baseline" disability of the patient, also called the disease "burden". The extent of lesions on T2WI, expressed usually by the total volume of lesions (T2LV), is currently regarded as the MRI measure of this disease burden. Usually dual echo T2 and proton density (PD) images are acquired and the lesions are detected using the combined information presented in the two images. The positive effects of three currently available injectable medications (Betaseron, Avonex, Copaxone) on T2 lesion load (T2LV) have been demonstrated.⁷⁻¹⁰ Despite impressive progress in the treatment and understanding of MS, both its etiology and pathogenesis still remain incompletely understood. An important limitation of T2WI is its low pathological specificity.¹¹ All histopathological features of MS, such as inflammation, edema, demyelination, axonal loss, gliosis and remyelination are seen as hyperintense lesions on T2WI while not all of these processes are clinically relevant. Reports from several research groups have shown only weak correlations between clinical measures of disability and the traditional T2 lesion load.¹²⁻¹⁴ There are also contradictory results among these reports - for example, that T2LV increases consistently and significantly in RR MS^{13, 15} and that it does not.^{12, 16} The reasons for such disagreements include imaging and processing methodological differences, subjectivity of EDSS and the non-accountability of the microscopic disease. In short, there is increasing evidence that T2LV is not a reliable measure of disease/disability in spite of its use in clinical trials.

1.2. T1-weighted imaging with gadolinium enhancement (T1WIE)

In MS, gadolinium (-DTPA) enhancement on MR images is characterized by blood brain barrier (BBB) breakdown and intense inflammation which represents the acute stage of the evolution of MS.^{17, 18} In T1WIE, gadolinium enhancement appears as a homogenous strongly hyperintense lesion or as a ring-shaped hyper-intensity at the edge of chronic reactivated lesions. Enhancement is more sensitive than either clinical examination or T2WI in detecting disease activity and potentially can separate clinical groups.¹⁹ Delayed imaging (50-60 minutes after gadolinium injection), triple doses of gadolinium, and a single dose with MT saturation to suppress normal brain have all been shown to increase the number of detectable enhancing lesions.²⁰ (There are disadvantages to high-dose contrast studies including possibly more false lesions, more scan time and more expense.) These results suggest that enhancement is not an "all or none" phenomenon. Enhancement may precede the development of T2 hyper-intensity and clinical symptoms, which suggest that the BBB abnormality may be the crucial event in the inflammatory cascade.^{15, 21} Further, we know that there is microscopic manifestation of the disease in normal appearing white matter (NAWM) which is not apparent under visual examination of the images.

1.3. Magnetization transfer imaging (MTI)

MS is now believed to be a diffuse process that extensively involves the white matter and is not restricted to the focal regions of disease activity visible as "lesions" in conventional T2, PD and T1WIE images. This notion came about mainly from magnetization transfer (MT) image analysis,²² but subsequently also supported by postmortem²³ revealing microscopic disease characterized by edema, cellular infiltration and demyelination in macroscopically normal appearing white matter. In MT imaging,²⁴ two consecutive sets of images are required, one with off-resonance pre-saturation of the relatively immobile macromolecular protons and one without. A magnetization transfer ratio (MTR) image is then computed from the two images according to $(M_o - M_s) / M_o$, where M_o and M_s are pixel intensities with and without pre-saturation. Published studies²²⁻²⁷ suggest that the MTR values for white matter in normal subjects are highly reproducible within each institution with a variation of less than 2%. Several studies have demonstrated that the microscopic aspect of the disease can be characterized by the MTR values measured in different regions (WM, lesions, the periphery of lesions) in a much more specific fashion than by T2LV.

1.4. T1-weighted imaging (T1WI)

Another standard MRI technique that is routinely used in MS is T1WI (SE). It often shows hypo-intense areas which were suggested to represent areas of axonal loss and gliosis.²⁸ In a recent quantitative study,²⁹ a significant correlation was reported between increase in disability and increase in the volume of these lesions (T1LV). In another study involving a larger cohort of patients³⁰ including RR and SP patients, a strong correlation was found only in the SP group between increase in T1LV and increase in disability over 3 years of follow-up that was higher than the increase in T2LV. In RR

patients, many T2 changes are unaccompanied by T1 changes. In contrast, in SP patients, there was a more linear relationship between accumulations of lesions in T1WI and T2WI. If hypointense lesions represent areas of severe demyelination, axonal loss or gliosis,^{27, 28} then the higher rate of new T2 lesions accompanied by signal loss on T1WI could reflect a deficit in available repair mechanism in SP patients. A higher "inflammatory" activity perhaps exhausts repair mechanisms leading to persistent structural loss without significant remyelination, in turn leading to persistent functional loss.³¹ From this, we may conclude that the quantitative assessment of hypointense lesions on T1WI may resolve part of the clinico-radiological paradox encountered when correlating MRI lesion load with clinical disability. The observed differences between RR and SP groups probably relate to a quantitative difference in repair mechanisms.

We have been developing MR image analysis methods for MS since 1993. Our approaches are guided by two premises. First, tissue regions in any anatomic object have a heterogeneous composition with or without the disease. Treating them in a binary fashion by considering a voxel to contain either 100% or 0% tissue material is unrealistic and inaccurate. The segmentation methods and the quantitative measures derived from them that we have devised take into account the heterogeneity and the fuzziness inherent in tissue regions. Second, as we have seen from the description in this section, different MRI protocols capture different aspects of the MS disease puzzle. We have therefore taken a multiprotocol approach wherein we utilize all major protocols currently employed in MS imaging and attempt to get a composite understanding of the most specific way of characterizing the disease through image derived parameters. In Section 2, we describe the methods employed for extracting these parameters from the various MRI protocols, and in Section 3, we summarize the clinical results we have obtained to date. In Section 4, we summarize the lessons learned from this experience and the outstanding problems that need to be addressed.

2. METHODS

2.1 Data acquisition

The MRI protocols we have been using in our patient studies are listed in the following table. Every patient recruited in our trial undergoes all acquisitions listed in the table. Our image database currently consists of the following number of patient studies and 3D volume images that have been processed by the methods described in this section: 690 T2WI studies, 660 T1 studies each with and without contrast, 670 MT studies, altogether 100 patients and over 4000 3D scenes.

| Pulse Seq. | Plane | TR (ms) | TE (ms) | Slice Th (mm) | Matrix | NEX | FOV (cm) |
|--------------|-------|---------|---------|---------------|--------|-----|----------|
| FSE VE | AXIAL | 2500 | 18, 90 | 3 | 192 | 1 | 22 |
| 3DMT Vas Tof | AXIAL | 106 | 5 | 5 | 128 | 1 | 22 |
| SE | AXIAL | 600 | 27 | 3 | 192 | 1 | 22 |
| SE with Gd | AXIAL | 600 | 27 | 3 | 192 | 1 | 22 |

The T2 and PD images in these acquisitions are in registration since they are acquired simultaneously. Similarly the two MT images are also in registration. However, between these two sets and among other image data, registration cannot be guaranteed.

2.2. Fuzzy connectedness image segmentation

The method of fuzzy connectedness forms the essential underpinning of all segmentation algorithms utilized in our MS image analysis efforts. Therefore, we will first give an outline of its principles. These principles are applicable to n -dimensional vector-valued scenes. However, our description will be confined to the three-dimensional case and to scalar-valued scenes.

We represent a volume image, called a 3D *scene* (*scene* for short) \mathcal{C} by a pair $\mathcal{C} = (C, f)$ where C is a rectangular array of voxels, called the *scene domain*, and f is a function that assigns to every voxel $c \in C$ an intensity value $f(c)$ from a range $[L, H]$ where L and H are integers. Objects such as WM in the brain are manifest in scenes with a heterogeneity of property values

(such as PD) because of the heterogeneity of material composition inherent in the object, and noise, blurring and background variations introduced by the imaging device. In spite of this *graded composition* of intensity values within object regions, human readers perceive regions in the scene belonging to the same object as a whole (gestalt). This property of *hanging-togetherness* of image elements and their graded composition are both fuzzy phenomena, which should be addressed properly for effective image segmentation. While the property of graded composition has been handled in the past through fuzzy logic and/or probabilistic methods, fuzzy connectedness was the first framework that allowed capturing the idea of fuzzy hanging-togetherness via fuzzy topological principles.³² It is defined as follows.

We think of any nearby voxels c and d in C as having a fuzzy adjacency. The strength $\mu_\alpha(c, d)$ of this fuzzy relation α is smaller the farther c and d are. The idea behind α is to capture the blurring property of imaging devices. We define another fuzzy relation κ in C that assigns to every pair of voxels (c, d) an *affinity*. The strength $\mu_\kappa(c, d)$ of this relation depends on how near c and d are spatially (i.e., on $\mu_\alpha(c, d)$) and on how similar the scene intensities $f(c)$ and $f(d)$ are as well as how similar intensity-based properties computed at c and d are. The intent here is that κ is "local"; that is, if c and d are far apart (spatially), then their affinity is 0. To define *fuzzy connectedness* K as another fuzzy relation in C , we consider all possible "paths" between all possible pairs of voxels in C . A path between any voxels c and d is simply a sequence of nearby voxels starting from c and ending in d . To every path from c to d we assign a "strength of connectedness" which is simply the smallest affinity of pairwise voxels along the path (weakest link). Finally, the strength of connectedness $\mu_K(c, d)$ between c and d is the largest of the strengths of connectedness of all paths between c and d . In determining a fuzzy connected object in C , $\mu_K(c, d)$ should be determined for all possible pairs (c, d) of voxels in C . This computationally explosive problem is considerably simplified through some key theoretical results, and finding fuzzy connected objects essentially reduces to dynamic programming.³²

The definition of affinity is a key to the effectiveness of segmentation in this method. We think of the strength of affinity $\mu_\kappa(c, d)$ between c and d to consist of three components:³³

$$\mu_\kappa(c, d) = g(\mu_\alpha, \mu_\psi, \mu_\phi) \quad (1)$$

μ_α is the adjacency component mentioned above. μ_ψ is a homogeneity-based component. As per this component, the greater the homogeneity of the intensity in the vicinity of c and d is the greater is the affinity. μ_ϕ is an object-feature-based component. As per this component, the closer the intensity-based features at c and d are to an expected value of these features for the object region, the greater is their affinity. A functional form of g we have used commonly is

$$\mu_\kappa(c, d) = \mu_\alpha(c, d) \sqrt{\mu_\psi(c, d) \mu_\phi(c, d)}. \quad (2)$$

In the scale-based approach,^{33, 34} $\mu_\psi(c, d)$ and $\mu_\phi(c, d)$ are defined taking into consideration all voxels within a sphere centered at c and d . The radius of this sphere is related to the "scale" at c and d of the object being defined. The *scale* of the object at any voxel c is defined as the radius of the largest sphere that can be placed with its center at c such that it encloses only voxels in the object region. Paradoxically, this may sound like we need object segmentation to define scale at c . We have developed a simple algorithm^{32, 33} that does not require object segmentation for estimating scale at every voxel c . The algorithm uses simply a homogeneity measure to determine at what radius there is a sudden change in homogeneity as the sphere is increased from a radius of 1. We have shown³² that scale-based fuzzy connectedness is less sensitive to noise and can detect thin and subtle aspects of the object more effectively than the original fuzzy connectedness method, yet the theory of the original fuzzy connectedness framework still holds. Scale-based fuzzy connectedness is a powerful segmentation method that differs from published methods in that, (1) it takes into account in its design the size of the object in different parts of the scene and image noise and other artifacts; (2) it handles both the graded composition and hanging-togetherness in a fuzzy setting. We note that since the local scale is taken into account in determining $\mu_\kappa(c, d)$, the actual functional form of the affinity varies over the scene domain, adapting to the local object size and noise characteristics. We have also shown that slow background variations do not affect fuzzy connected object segmentations.^{32, 33}

In the rest of this section, we summarize our approach to analyzing the scenes for the different protocols. The basic premise behind these approaches is the following. We think of segmentation to consist of two related tasks - recognition and delineation. *Recognition* is the high-level process of roughly determining the whereabouts of the object in the scene.

Delineation is the low-level process of determining the precise spatial extent and voxel-by-voxel material percent content of the object. Knowledgeable humans can outperform computer algorithms in most recognition tasks such as those encountered in our application. Conversely, computer algorithms can be devised to more precisely, accurately, and efficiently delineate objects in scenes than manual delineation. Clearly, manual delineation to indicate the graded material composition within an object is impossible. The system we have developed for the above four tasks exploits this synergy between human and computer abilities in devising practical solutions that can be used routinely in clinical trials.

2.3. Analysis of FSE T2, PD images

The approach here consists of the following four steps.³⁵ We consider here the scene to be vector-valued with two (T2 and PD) values per voxel.

1. On one slice, roughly centrally situated in the brain, an operator specifies a few voxels (seeds). This is a recognition step that uses the superior human knowledge. Points (voxels) are specified for the CSF, GM, and WM regions (and not for lesions).
2. This is a delineation step. The seed voxels are utilized to determine the fuzzy connected objects that contain them. This results first in a segmentation of WM, GM, and CSF. This knowledge is subsequently used to determine automatically a set of points (determined as holes in the union of GM and WM fuzzy objects) in each 3D lesion object that are used subsequently to delineate the lesions, each as a 3D fuzzy connected object.
3. This is again a recognition step taking help from a human operator. In this step, the operator accepts true lesions and rejects false lesions with a mouse button click. Each 3D lesion is displayed on one slice image passing close to the centroid of the lesion. The operator may override this mode of display and examine the lesions on all or any selected slices. All false positives are eliminated in this fashion. These are usually artifacts and choroid plexus. We found that the number of false negatives is very low in our system (see next section for details on validation). Nevertheless, the system allows in this step selecting new seed points for missed lesions. These are subsequently utilized in delineating these lesions by repeating part of Step 2 above.
4. The final step is the computation of quantitative measures from the segmented objects. These include the number of 3D lesions and their total volume (T2LV), the volume of CSF (CSFV), the volume of the brain parenchyma (BPV) which is the volume of the union of GM and WM, and normalized BPV, $nBPV = BPV/(BPV + CSFV)$. The purpose of the last measure is to express the parenchymal volume independent of subject-to-subject variations in brain size.

2.4 Analysis of T1WIE images

The approach here consists of the following steps.³⁶

1. A conservative threshold is determined automatically from the histogram of the T1WIE 3D scene (see ³⁶ for details). The purpose of this threshold is to select seed points automatically within the enhancing lesions. This is a recognition step.
2. The seed points are utilized to determine the fuzzy connected objects that contain them. This delineation step often results in the delineation of vessels. Taking the volume enclosed by the object as a criterion, large objects (large vessels) are automatically discarded.
3. This step is identical to Step 3 of the previous section.
4. For the accepted lesions, their total volume (T1EV) and number ($nT1EV$) are computed.

2.5. Analysis of MT images

The steps involved in this process are as follows.³⁷

1. The brain is first segmented from the two MT scenes (corresponding to the off-resonance pulse on and off). The brain mask is then utilized to compute an MTR scene $\mathcal{C}_{MT}^{BP} = (C_{MT}^{BP}, f_{MT}^{BP})$, which is such that $f_{MT}^{BP}(c) = 0$ if c is not in the brain parenchymal region, otherwise $f_{MT}^{BP}(c)$ will have a value as determined from the two MT scenes as described in Section 1.3.
2. The PD scene is registered with the MT scene corresponding to the off-resonance pulse off.³⁸ Subsequently the PD and T2 scenes are redigitized to match with the MT scenes slice-to-slice. The redigitized scenes are segmented for WM and GM as described in Section 2.3. The MTR scenes \mathcal{C}_{MT}^{GM} and \mathcal{C}_{MT}^{WM} are computed subsequently.
3. For each of the MTR scenes \mathcal{C}_{MT}^{BP} , \mathcal{C}_{MT}^{WM} , and \mathcal{C}_{MT}^{GM} , a histogram of the whole scene normalized to BPV is computed. From each of these histograms, the following parameters are computed: peak height normalized by BPV (nPh_{BP}); the mode M_x ; the 25th and 50th percentiles ($P25_x$, $P50_x$) and the mean m_x , where x stands for BP, WM, or GM.

3. RESULTS

3.1. Validation

Any segmentation effort consists of: (i) a theoretical/algorithmic framework, (ii) considerable engineering effort to make the framework work in the application at hand, and (iii) evaluation to establish the precision, accuracy, and efficiency of the subjective actions including how the patient is positioned in the scanner and any operator input required by the algorithms. *Accuracy* denotes the degree of agreement of the result with truth. *Efficiency* indicates the degree of operator help required (the degree of automation), which may be expressed as the operator time required for each study. A compromise in one factor is usually required to achieve an improvement in another. Below we summarize the precision, accuracy, and efficiency of the various analysis processes described in the previous section. We have done extensive evaluations of our system taking into account the subjectivity that appears in Steps 1 and 3 and in the placement of the patient in the scanner. A summary of the results is as follows.^{35-37, 39} For T2LV: Inter- and intra-operator coefficient of variation < 0.9%; repeat scan variations = 1.5%; 95% confidence interval for false negative T2LV: 0%-2.8%; mean operator-time required (on a Sparc 20 Sun workstation): 10 minutes per study. This reduced to about 7 minutes on a Sun Ultra Sparc. For T1ELV: No inter- and intra-operator variations, and 1.3% false negative T1ELV; mean operator time: 2 minutes per study. For BPV: Inter- and intra-operator coefficient of variation < 0.5% including repeat scans; false negative volume < 1%; mean operator time: 5 minutes per study. For MTR: > 99% correlation for MTR histogram parameters in repeated experiments; mean operator time: 10 minutes/study.

Any segmentation method can and will go wrong in practice. In completely automatic methods, a question arises as to what to do in case of false positives and negatives for recognition and delineation. Our system is, by design, not automatic to facilitate taking recognition help from the user to minimize false positives and negatives. However, this help is taken as efficaciously as possible to make the system efficient and practical. We continue to improve the efficiency of our system without sacrificing precision and accuracy.

3.2. Clinical

In this section we summarize the results we have obtained to date in analyzing the images in our database and in conducting clinical correlation analysis with the EDSS scores.

T2WI:³⁹⁻⁴⁵ By far, the strongest correlations were seen in our experiments for T2LV with nBPV (-0.73, $p < .001$) in the RR group and with nPH_{BP} (-0.76, $p < .001$) and T1ELV (0.66, $p < 0.001$) both in the RR group. T2LV showed a good correlation with nBPV (-0.66, $p < 0.02$) in the CP group. In both groups, the correlation of T2LV with EDSS scores was not significant. Generally, we found CSFV to be significantly larger in MS patients and nBPV to be smaller than in age-matched normal control subjects ($p < 0.005$). A good correlation was seen between T2LV and CSFV (0.73, $p < 0.001$). By analyzing U-fiber lesions, we found a significant ($p \leq 0.05$) difference in three of the 11 neuropsychological test scores between patients with

and without these lesions, possibly indicating that these lesions may lead to neuropsychological impairment. By analyzing the lesions in gray matter, we found that cortical gray matter lesions comprised about 5.7% of the total T2LV while deep gray matter lesions comprised about 4.6%. No significant correlation was found between these volumes and clinical disability. By far, the parameter computed from T2-PD scenes that produced the strongest correlation with disability was nBPV ($-0.69, p < 0.004$) for the SP group of patients suggesting that brain atrophy may be an important measure for characterizing disease via T2WI.

T1W1E:^{39, 41, 42, 46, 47} We have generally found that T1ELV was greater in RR patients than in CP patients ($p < 0.05$). T1ELV showed good correlation with nBPV ($-0.51, p < 0.009$) only for RR MS. It also correlates well with T2LV only in the RR group. Compared to a group of RR patients receiving placebo, another group of RR patients receiving copaxone had a significant decrease in the number of enhancing lesions ($p = 0.05$) and in their volume ($p = 0.01$) at the end of 24 months.⁴⁷ No differences were seen in T2LV in the two groups. The loss of brain tissue was significantly less ($p = 0.02$) in the group receiving copaxone than in the placebo group. This was the first study to report the MRI activity in copaxone clinical trials of MS therapies. We were able to demonstrate through our MS software system that the drug made a significant impact on inflammation and on preventing brain atrophy in RR patients.

MT imaging:^{41-43, 48-50} Compared to the normal control group, nPH_{BP} for the MS study group (consisting of both RR and CP patients) was significantly lower ($p < 0.0005$), and so were M_{BP} ($p < 0.05$), P25_{BP} ($p < 0.05$), and P50_{BP} ($p < 0.05$). nPH_{BP}, particularly, showed the best correlation with EDSS score for the RR group ($-0.44, p < .02$). This parameter correlated strongly with nBPV in both RR ($0.69, p < 0.001$) and the CP ($0.87, p < 0.001$) groups, and with CSFV ($-0.828, p < 0.0001$) when the two groups are pooled into a single group. MTR parameters also correlated with disease duration ($p < 0.01$). Individual neuropsychological tests correlated with MTR measures ($p < 0.001$). The unnormalized histogram peak height differed ($p < 0.05$) among severely impaired, moderately impaired, and normal patients. In a serial MRI study of the RR group, nPH_{BP} demonstrated a subtle but significant ($p < 0.05$) decline over time while no significant changes in EDSS were noted. M_{WM} and m_{WM} were significantly ($p < 0.05$) lower in RR MS patients than in normal controls.⁵¹ In longitudinal studies, both these entities shifted in the direction of normal with increasing disease duration. Up to 44% of new lesions identified on later studies were demonstrated to have originated in the WM region, which had been identified as abnormal by MTR criteria. As to the GM, M_{GM} and m_{GM} were significantly ($p < 0.01$) lower in RR MS patients than in normal controls.⁵² nPH_{GM} inversely correlated with EDSS ($r = 0.65, p < 0.01$).

In summary, the strongest correlations with the disease status as measured by EDSS were observed in our clinical trials with the brain parenchymal volume (normalized) and the MTR parameters for the various tissue components. This emphasizes the need to consider nBPV and the microscopic MS disease in devising objective measures to assess the MS disease.

4. CONCLUDING REMARKS

4.1. Automation, failure, user assistance

Any segmentation method can, and therefore, will, go wrong if a sufficient number of studies are analyzed in a routine clinical trial setting. Therefore, for quality assurance, it is important to have a knowledgeable human operator within the processing loop. Complete automation may, therefore, be an elusive goal, perhaps reachable after only a great deal of experience within the same imaging modality, protocol, and application setting. As researchers and developers, our aim should be to consider human interaction within the design framework itself of the segmentation algorithms with a research goal of minimizing this interaction as much as possible. The system that we presented here may not be optimal yet in terms of the degree of automation achievable, but it is certainly practical. We continue to tighten this slack in efficiency.

4.2. Standardization of MR intensity scale

A major difficulty with the MRI techniques for most protocols has been that image intensities do not have a fixed meaning, even within the same protocol, for the same body region, for images obtained on the same scanner, for the same patient. This poses problems in finding the proper window setting for image display, and more importantly, in image segmentation and analysis. Most image segmentation methods have parameters. Without the same protocol-specific intensity meaning, setting values for the parameters in a patient-study-independent fashion becomes very difficult. This results in compromising precision, accuracy, and efficiency of segmentation. For example, per study adjustment of parameters may be necessary to handle these scanner-dependent variations in intensity, which will affect efficiency and may also lower precision.

We have recently developed a method^{53, 54} to standardize the MR image intensity scale. It is a post-acquisition processing method which maps non-linearly the scene intensities in any given scene acquired as per a given protocol for a given body region into a standard scale so that the same intensities in the transformed scene will have the same tissue specific meaning. The method is based on deforming histograms so that they are as similar as possible for all scenes of the same body region and protocol. We are in the process of utilizing this method in modifying our system to improve the efficiency of the various processes of quantification without sacrificing precision and accuracy.

4.3. Standard intensity-based analysis

All objects - normal and pathological - have a heterogeneous tissue composition. This combined with the blurring and noise introduced by the imaging device makes tissue regions have a heterogeneity of intensities. We believe that this heterogeneity has tissue-specific information and is useful in characterizing disease stage and severity. Such a characterization becomes impossible when there is scanner-dependent intensity variation. As illustrated by MTR analysis,^{22-27, 48, 49} because of the tissue-specific meaning of MTR values, standardization may permit us to treat other protocols (T2, PD, T1WIE, T1WI) also in the same tissue-specific way as MT imaging. More importantly, flat measures such as volume of tissue regions ignore the heterogeneity information and may lose important disease specific information. We should really consider volume distributions, that is, intensity histograms within segmented tissue regions, as demonstrated by MTR analysis, for understanding subtle disease processes.

4.4. MS segmentation "workshop"

In MS (and other neurological applications), a variety of MRI protocols are utilized as we examined in this paper. The actual imaging parameters used in these protocols vary among institutions. In spite of the numerous brain MR image segmentation methods developed during the past 15 years, none of them is capable of handling variations within the same protocol, and much less, the variations among protocols. What we need is a segmentation "workshop" wherein a protocol-specific segmentation method can be quickly fabricated. For the MS application, we believe that the fuzzy connectedness framework can be utilized to build such a workshop and we are working toward this goal.

ACKNOWLEDGEMENT

The authors are grateful to Mary A. Blue for typing the manuscript. The research reported here is supported by NIH grants NS37172 and NS29029.

REFERENCE

1. J.M. Charcot, *Lectures on the Diseases of the Nervous System*, New Sydenham Society, London, England, 1977.
2. J.F. Kurtzke, "Geographic distribution of multiple sclerosis: An update with special reference to Europe and the Mediterranean region," *Acta Neurology Scandinavia* 62, pp. 65-80, 1980.
3. S.L. Hauser, "Multiple sclerosis and other demyelinating disease," in Harrison's Principle of Internal Medicine, pp. 2287-2295. K.J. Isselbacher, E.G., J.D. Wilson, J.B. Martin, A.S. Fauci, and D.L. Kasper (eds.), McGraw-Hill, Inc., New York, 1994.
4. J.F. Kurtzke, "Rating neurologic impairment in multiple sclerosis: An expanded disability status scale (EDSS)," *Neurology* 33, pp. 1444-1452 1983.
5. S.A. Lukes, L.E. Crooks, M.J. Aminoff, L. Kaufman, H.S. Panitch, C. Mills, and D. Norman, "Nuclear magnetic resonance imaging in multiple sclerosis," *Annals of Neuroradiology* 13, pp. 592-601, 1983.
6. J.J. Sheldon, R. Siddharthan, A. Tobias, W.A. Sheremata, K. Soila and M.J. Viamonte, "MR imaging of multiple sclerosis: Comparison with clinical and CT examinations in 74 patients," *American Journal of Neuroradiology* 6, pp. 683-680, 1985.
7. L.D. Jacobs, D.L. Cookfair, R.A. Rudick, R.M. Herndon, J.R. Richert, A.M. Salazar, J.S. Fischer, D.E. Goodkin, C.V. Granger, J.H. Simon, J.J. Alam, D.M. Bartoszak, J. Brainman, C.M. Brownscheidle, M.E. Coats, S.L. Cohan, D.S. Dougherty, R.P. Kinkel, M.K. Mass, F.E. Munschauer, R.L. Priore, P.M. Pullincino, B.J. Scherokman and R.H. Whitham, "Intramuscular interferon beta-1a for disease progression in relapsing multiple sclerosis," The Multiple Sclerosis Collaborative Research Group (MSCRG), *Annals of Neuroradiology* 39, pp. 285-294, 1996.

8. R.A Rudick, D.E. Goodkin, L.D. Jacobs, D.L. Cookfair, R.M. Herndon, J.R. Richert, A.M. Salazar, J.S. Fischer, C.V. Granger, J.H. Simon, J.J. Alam, N.A. Simonian, M.K. Campion, D.M. Bartoszak, D.N. Bourdette, J. Brainman, C.M. Brownscheidle, M.E. Coats, S.L. Cohan, D.S. Dougherty, R.P. Kinkel, M.K. Mass, F.E. Munschauer, and R.L. Priore, "Impact of interferon beta-1a on a neurologic disability in relapsing multiple sclerosis," *Neurology* 49, pp. 358-363, 1997.
9. K.P. Johnson, B.R. Brooks, J.A. Cohen, C.C. Ford, J. Goldstein, R.P. Lisak, L.W. Myers, H.S. Panitch, J.W. Rose, R.B. Schiffer, t. Vollmer, L.P. Weiner, and J.S. Wolinsky, "Extended use of glatiramer acetate (Copaxone) is well tolerated and maintains its clinical effects on multiple sclerosis relapse rate and degree of disability," Copolymer 1 Multiple Sclerosis Study Group, *Neurology* 50, pp. 701-708, 1998.
10. IFNB Multiple Sclerosis Study Group and the University of British Columbia MS/MRI Analysis Group [see comments], "Interferon beta-1a in the treatment of sclerosis: Final outcome of the randomized controlled trial," *Neurology* 45, pp. 1277-85, 1995.
11. D.H. Miller, R.I. Grossman, S.C. Reingold, and H.F. McFarland, "The role of magnetic resonance techniques in understanding and managing multiple sclerosis," *Brain* 122, pp. 3-24, 1998.
12. D.W. Paty, D.K. Li, Group tUMMS, and Group atIMSS, "Interferon beta-1b is effective in relapsing-remitting multiple sclerosis, II: MRI analysis results of a multicenter, randomized, double-blind, placebo-controlled trial," UBC MS/MRI Study Group and the IFNB Multiple Sclerosis Study Group [see comments], *Neurology* 43, pp. 662-667, 1993.
13. Y. Miki, R.I. Grossman, J.K. Udupa, L. Wei, M. Polansky, L.J. Mannon and D.L. Kolson, "Relapsing-remitting multiple sclerosis: Longitudinal analysis of MR images - lack of correlation between changes in T2 lesions volume and clinical findings," *Radiology* 213, pp. 395-399, 1999.
14. A.J. Thompson, A.G. Kermode, D.G. MacManus, B.E. Kendall, D.P. Kingsley, I.F. Moseley, and W.I. McDonald, "Patterns of disease activity in multiple sclerosis: Clinical and magnetic resonance imaging study," [see comments]. *BMJ* 300, pp. 631-634, 1990.
15. A.G. Kermode, A.J. Thompson, P. Tofts, D.G. MacManus, B.E. Kendall, D.P. Kingsley, I.F. Moseley, P. Rudge, and W.I. McDonald, "Breakdown of the blood-brain barrier precedes symptoms and other MRI signs of new lesions in multiple sclerosis: Pathogenetic and clinical implications," *Brain* 113, pp. 1477-1489, 1990.
16. M. Filippi, M.A. Horsfield, S.P. Morrissey, D.G. MacManus, P. Rudge, W.I. McDonald and D.H. Miller, "Quantitative brain MRI lesion load predicts the course of clinically isolated syndromes suggestive of multiple sclerosis," *Neurology* 44, pp. 635-641, 1994.
17. R.I. Grossman, F. Gonzalez-Scarano, and S.W. Atlas, "Multiple sclerosis: Gadolinium enhancement in MR imaging," *Radiology* 161, pp. 721-725, 1986.
18. A.G. Kermode, P.S. Tofts, A.J. Thompson, D.G. MacManus, P. Rudge, B.E. Kendall, D.P. Kingsley, I.F. Moseley, and W.I. McDonald, "Heterogeneity of blood-brain barrier changes in multiple sclerosis: A MRI study with gadolinium-DTPA enhancement," *Neurology* 40, pp. 229-235, 1990.
19. D.H. Miller, F. Barkhof, and J.J. Nauta, "Gadolinium enhancement increases the sensitivity of MRI in detecting disease activity in multiple sclerosis," *Brain* 116, pp. 1077-1094, 1993.
20. M. Filippi, T. Yousry, A. Campi, C. Kandziora, B. Colombo, R. Voltz, V. Martinelli, S. Spuler, S. Bressi, G. Scotti, and G. Comi, "Comparison of triple dose versus standard dose gadolinium-DTPA for detection of MRI enhancing lesions in patients with MS," *Neurology* 46, p. 379-384, 1996.
21. H.J. Baratt, D. Miller, and P. Rudge, "The site of lesion causing deafness in multiple sclerosis," *Scandinavian Audiology* 17, pp. 67-71, 1988.
22. V. Dousset, R.I. Grossman, K.N. Ramer, M.D. Schnall, L.H. Young, S.F. Gonzalez, E. Lavi, and J.A. Cohen, "Experimental allergic encephalomyelitis and multiple sclerosis: Lesion characterization with magnetization transfer imaging," *Radiology* 182, pp. 483-492, 1992.
23. I.V. Allen and S.R. McKeown, "A histopathological, histochemical and biochemical study of the macroscopically normal white matter in multiple sclerosis," *Journal of Neurological Science* 41, pp. 81-91, 1979.
24. S.D. Wolff and R.S. Balaban, "Magnetization transfer contrast (MTC) and tissue water proton relaxation *in vivo*," *Magnetic Resonance in Medicine* 10, pp. 135-144, 1989.
25. M. Filippi, a. Campi, V. Dousset, C. Baretta, V. Martinelli, N. Canal, G. Scotti, and G. Comi, "A magnetization transfer imaging study of normal-appearing white matter in multiple sclerosis," *Neurology* 45, pp. 478-482, 1995.
26. L.A. Loewner, R.I. Grossman, J.A. Cohen, F.J. Lexa, D. Kessler, and D.L. Kolson, "Microscopic disease in normal appearing white matter on conventional MR images in patients with multiple sclerosis: Assessment with magnetization-transfer measurements," *Radiology* 196, pp. 511-515, 1995.
27. A. Gass, G.J. Barker, D. Kidd, J.W. Thorpe, D. MacManus, A. Brenna, P.S. Tofts, A.J. Thompson, W.I. McDonald, and D.H. Miller, "Correlation of magnetization transfer ratio with clinical disability in multiple sclerosis," *Annals of Neurology* 36, pp. 62-67, 1994.

28. D. Uhlenbrock and S. Sehlen, "The value of T1-weighted images in the differentiation between MS, white matter lesions and subcortical arteriosclerotic encephalopathy (SAE)," *Neuroradiology* 31, pp. 203-212, 1989.
29. M.A. van Walderveen, F. Barkhof, O.R. Hommes, C.H. Polman, H. Tobi, and S.T.F.M. Frenquin, "Correlating MR imaging and clinical disease activity in multiple sclerosis: Relevance of hypointense lesions on short TR short TE ("T1-weighted") spin-echo images," *Neurology* 45, pp. 1684-1690, 1995.
30. L. Truyen, J.H.T.M. van Waesberghe, M.A.A. van Walderveen, B.W. van Oosten, C.H. Polman, O.R. Hommes, and H.J. Ader, "Accumulation of hypointense lesions ("black holes") on T1 spin-echo MRI correlates with disease progression in multiple sclerosis," *Neurology* 47, pp. 1469-1476, 1996.
31. J.W. Prineas, R.O. Barnard, T. Revesz, and et al., "Multiple sclerosis: Pathology of recurrent lesions," *Brain* 116, pp. 681-693, 1993.
32. J.K. Udupa and S. Samarasekera, "Fuzzy connectedness and object definition: Theory, algorithms and applications in image segmentation," *Graphical Models and Image Processing* 58(3), pp. 246-261, 1996.
33. P.K. Saha and J.K. Udupa, "Scale-based fuzzy connectivity: A novel image segmentation methodology and its validation," *SPIE Proceedings* 3661, pp. 249-257, 1999.
34. P. Saha and J.K. Udupa, "Scale-based fuzzy connected image segmentation: Theory, algorithms and validation," *Computer Vision and Image Understanding*, in press.
35. J.K. Udupa, L. Wei, S. Samarasekera, Y. Miki, M.A. van Buchem, and R.I. Grossman, "Multiple sclerosis lesion quantification using fuzzy connectedness principles," *IEEE Transactions on Medical Imaging* 16(5), pp. 598-709, 1997.
36. S. Samarasekera, J.K. Udupa, Y. Miki, and R.I. Grossman, "A new computer-assisted method for enhancing lesion quantification in multiple sclerosis," *Journal of Computer Assisted tomography* 21(1), pp. 145-151, 1997.
37. M.A. van Buchem, J.K. Udupa, J.C. McGowan, S. Samarasekera, and R.I. Grossman, "Quantification of macroscopic and microscopic cerebral disease burden in multiple sclerosis," *American Journal of Neuroradiology* 18, pp. 1287-1290, 1997.
38. R. Woods, J. Mazziotta, and S. Cherry, "MRI-PET registration with automated algorithm," *Journal of Computer Assisted Tomography* 17, pp. 536-546, 1993.
39. Y. Ge, R.I. Grossman, J.K. Udupa, L. Wei, L.J. Mannon, M. Polansky, and D.L. Kolson, "Longitudinal quantitative analysis of brain atrophy in relapsing-remitting and secondary-progressive multiple sclerosis," *Radiology*, accepted.
40. Y. Miki, R.I. Grossman, J.K. Udupa, L. Wei, D.L. Kolson, and L.J. Mannon, "Isolated U-fiber involvement in MS: Preliminary observations," *Neurology* 50, pp. 1301-1306, 1998.
41. Y. Miki, R.I. Grossman, J.K. Udupa, M.A. van Buchem, L. Wei, M.D. Phillips, U. Patel, J.C. McGowan, and D.L. Kolson, "Differences between relapsing remitting and chronic progressive multiple sclerosis as determined with quantitative MR imaging," *Radiology* 210, pp. 769-774, 1999.
42. Y. Miki, R.I. Grossman, J.K. Udupa, L. Wei, M. Polansky, L.J. Mannon, and D.L. Kolson, ""Relapsing-remitting multiple sclerosis: Longitudinal analysis of MR images - lack of correlation between changes in T2 lesions volume and clinical findings," *Radiology* 213, pp. 395-399, 1999.
43. M. Phillips, R.I. Grossman, Y. Miki, L. Wei, D.L. Kolson, M.A. van Buchem, M. Polansky, J.C. McGowan, and J.K. Udupa, "Comparison of T2 lesion burden in patients with multiple sclerosis," *American Journal of Neuroradiology* 19, pp. 1055-1060, 1998.
44. I. Catalaa, J.C. Fulton, X. Zhang, J.K. Udupa, D. Kolson, M. Grossman, L. Wei, J. McGowan, M. Polansky, and R.I. Grossman, "MR imaging quantitation of gray matter involvement in multiple sclerosis and its correlation with disability measures and neuro-cognitive testing," *American Journal of Neuroradiology* 20, pp. 1613-1618, 1999.
45. J.C. Fulton, R.I. Grossman, J.K. Udupa, L.J. Mannon, M. Grossman, L. Wei, M. Polansky, and D.L. Kolson, "Lesion load and disability measurements in multiple sclerosis," *Neurology*, submitted.
46. Y. Miki, R.I. Grossman, S. Samarasekera, J.K. Udupa, M.A. van Buchem, B.S. Cooney, S.N. Pollack, D.K. Kolson, M. Polansky, and L.J. Mannon, "Clinical correlation of computer assisted enhancing lesion quantification in multiple sclerosis," *American Journal of Neuroradiology* 18, pp. 705-710, 1997.
47. Y. Ge, R.I. Grossman, J.K. Udupa, J. Fulton, C.S. Constantinescu, F. Gonzales-Scarano, J.S. Babb, L.J. Mannon, D.L. Kolson, and J.A. Cohen, "Glatiramer acetate (copaxone) treatment in relapsing-remitting multiple sclerosis: Quantitative MR assessment," *Neurology*, submitted.
48. M.A. van Buchem, J.K. Udupa, F.H. Heyning, M.P. Boncoeur-Martel, Y. Miki, J.C. McGowan, D.L. Kolson, M. Polansky, and R.I. Grossman, "Quantitation of macroscopic and microscopic cerebral disease burden in multiple sclerosis," *American Journal of Neuroradiology* 18, pp. 1287-1290, 1997.
49. M.A. van Buchem, R.I. Grossman, C. Armstrong, M. Polansky, Y. Miki, F.H. Heyning, M.P. Boncoeur-Martel, L. Wei, J.K. Udupa, M. Grossman, D.L. Kolson, and J.C. McGowan, "Correlation of volumetric magnetization transfer imaging with clinical data in MS," *Neurology* 50, pp. 1609-1617, 1998.

50. U.J. Patel, R.I. Grossman, J.K. Udupa, M.D. Phillips, J.C. McGowan, Y.I. Miki, L. Wei, M. Polansky, M.A. van Buchem, and D. Kolson, "Serial analysis of magnetization transfer histograms and expanded disability status scale in relapsing multiple sclerosis patients," *American Journal of Neuroradiology*, submitted.
51. I. Catalaa, R.I. Grossman, D.L. Kolson, J.K. Udupa, L.G. Nyul, L. Wei, X. Zhang, M. Polansky, L.J. Mannon, and J.C. McGowan, "Magnetization transfer histogram analysis of segmented normal-appearing white matter in multiple sclerosis," *Radiology*, in press.
52. Y. Ge, R.I. Grossman, J.K. Udupa, J.S. Babb, D.L. Kolson, and J.C. McGowan, "Magnetization transfer histogram analysis of gray matter in relapsing-remitting multiple sclerosis," *American Journal of Neuroradiology*, submitted.
53. L.G. Nyul and J.K. Udupa, "On standardizing the MR image intensity scale," *Magnetic Resonance in Medicine* 42, pp. 1072-1081, 1999.
54. L.G. Nyul and J.K. Udupa, "New variants of a method of MRI scale standardization," *IEEE Transactions on Medical Imaging*, in press.

An ultra-fast user-steered image segmentation paradigm: live-wire-on-the-fly

Alexandre X. Falcão^a, Jayaram K. Udupa^b, and Flávio K. Miyazawa^a

^aComputing Institute, State University of Campinas, Campinas, SP, Brazil

^bDepartment of Radiology, University of Pennsylvania, Philadelphia, PA, USA

ABSTRACT

In the past, we have presented three user-steered image segmentation paradigms: live wire, live lane, and the 3D extension of the live-wire method. In this paper, we introduce an ultra-fast live-wire method, referred to as live-wire-on-the-fly, for further reducing user's time compared to live wire. For both approaches, given a slice and a 2D boundary of interest in this slice, we translate the problem of finding the best boundary segment between any two points specified by the user on this boundary to the problem of finding the minimum-cost path between two vertices in a weighted and directed graph. The entire 2D boundary is identified as a set of consecutive boundary segments, each specified and detected in this fashion. A drawback in live wire is that the speed for optimal path computation depends on image size, compromising the overall segmentation efficiency. In this work, we solve this problem by exploiting some properties of graph theory to avoid unnecessary minimum-cost path computation during segmentation. Based on 164 segmentation experiments from an actual medical application, we demonstrate that live-wire-on-the-fly is about 1.5 to 33 times faster than live wire for actual segmentation, although the pure computational part alone is found to be over a hundred times faster.

Keywords: image segmentation, boundary detection, active boundaries, 3D imaging, shortest-path algorithms, dynamic programming, graph theory.

1. INTRODUCTION

Image segmentation is a hard problem with numerous applications in the imaging sciences.¹ It consists of two tightly coupled tasks - *recognition* and *delineation*. Recognition is the process of identifying roughly the whereabouts of a particular object in the image and delineation is the process of specifying the precise spatial extent and composition of this object. While computer algorithms are very effective in object delineation, the absence of relevant global object-related knowledge is the main reason for their failure in object recognition. On the other hand, a simple user assistance in object recognition is often sufficient to complement this deficiency and to complete the segmentation process. There are many difficult segmentation tasks that require a detailed user assistance. To address these problems, a variety of interactive segmentation methods are being developed.² These methods range from totally manual painting of object regions or drawing of object boundaries to the detection of object region/boundaries with minimal user assistance.³⁻⁷

We have been developing interactive segmentation strategies with two specific aims: (i) to provide as *complete* a *control* as possible to the user on the segmentation process *while* it is being executed, and (ii) to minimize the user involvement and the total user's time required for segmentation, without compromising the precision and accuracy of segmentation. Our strategy in these methods has been to actively exploit the superior abilities of human operators (compared to computer algorithms) in object recognition and the superior abilities of computer algorithms (compared to human operators) in object delineation.

In the past, we have presented two user-steered segmentation paradigms, referred to as live wire and live lane,^{6,8} to segment 3D/4D object boundaries in a slice-by-slice fashion. These methods are in routine use in two applications⁹⁻¹² with over 15,000 tracings done so far. Although the live-wire method has its origin in some early joint work between Barrett and Udupa,¹³⁻¹⁵ this method has been subsequently developed independently by the two groups.^{6-8,16-18} There are many differences between the live-wire method developed by each group, as previously explained in.⁶ Besides these differences, we have extended the ideas underlying the live-wire method to create new methods, live

Further author information: Send correspondence to A.X.F.: E-mail:afalcao@dcc.unicamp.br, Telephone: +55(19)7885881, FAX +55(19)7885847.

lane⁶ and the 3D extension of live wire.¹⁶ In this paper, we introduce an ultra-fast live-wire method, referred to as live-wire-on-the-fly, with a new live-wire algorithm for drastically reducing user's time compared to our previous work on 2D live wire.

In live wire,^{6,7} to segment a 2D boundary, the user initially picks a point on the boundary and all possible minimum-cost paths from this point to all other points in the image are computed via dynamic programming. Subsequently, a "live wire" is displayed in real time from the initial point to any subsequent position taken by the cursor. If the cursor is close to the desired boundary, the live wire snaps on to the boundary. The cursor is then deposited and a new live-wire segment is found next. The entire 2D boundary is specified via a set of live-wire segments in this fashion. A drawback of this approach is the computational time for all possible minimum-cost segments from each selected point on the boundary to other points in the image. This time increases with the size of the image compromising the interactivity of the method in some practical situations. For images from 256×256 to 1024×1024 pixels, for example, live wire running on a 300MHz Pentium PC requires about 2 to 180 seconds to compute all possible minimum-cost segments from each selected point.

In live wire on the fly, the user-interaction process remains the same, but we have devised a linear time complexity algorithm to save a considerable amount of user time by avoiding the computation of all possible minimum-cost segments. When the user selects a point on the boundary, the live-wire segment is *computed and displayed* in real time from the selected point to any subsequent position of the cursor in the image. To make this feasible, we exploit the fact that by the time we have found a live-wire segment with cost value K , we have actually found all possible live-wire segments with cost value less than K in the image. Moreover, any live-wire segment with cost value greater than or equal to K contains one of the previous live-wire segments with cost value less than K . Therefore, the computation of the minimum-cost segment from a selected point to the current position of the cursor uses the results of computation from the selected point to the previous position of the cursor.

In Section 2, we present the live-wire-on-the-fly method and its algorithms. In Section 3, we present the results of evaluation between live wire and live wire on the fly based on efficiency for segmentation. Finally, we state some concluding remarks in Section 4.

2. LIVE-WIRE-ON-THE-FLY

We define a *2D scene* C as a pair (C, g) consisting of a finite 2D rectangular array C of pixels and a function $g(p) : C \rightarrow [L, H]$ that assigns to each pixel p in C an intensity value lying in an interval $[L, H]$. We associate with C a directed graph in which the vertices of the pixels represent the nodes of the graph and the oriented pixel edges represent the arcs. A 2D boundary of interest in C is a closed, oriented, and connected contour made up of oriented pixel edges. Each oriented pixel edge in C is a potential boundary element b , which is called a *bel* for short. To each bel b , we assign a set of features whose values characterize the "boundariness" of b . These values are converted to a single joint cost value $c(b)$ per bel b . Thus, the problem of finding the best boundary segment (live-wire segment) between any two points (pixel vertices) specified on the boundary is translated to finding the minimum-cost path between the corresponding two vertices of the graph. The issues about selection of features and how to convert feature values into cost values were previously addressed in.⁶ The problem we want to address here is how to reduce the time for optimum path computation, and, consequently, the total user's time required for segmentation.

To tackle this problem, we will exploit some known properties of graph theory, particularly for the computation of shortest-paths, as described in Section 2.1. This leads to the algorithms presented in Section 2.2.

2.1. Graph Properties of Shortest Paths

In the literature on shortest-path algorithms,¹⁹ there are many efficient solutions for finding minimum-cost paths in a weighted and directed graph. Particularly, we have adopted Dial's implementation of the Dijkstra's algorithm.²⁰ This algorithm computes the shortest-paths to all nodes from a single node in $O(m + nC)$ time, where m is the number of arcs, n is the number of nodes, and C is the maximum cost assigned to any arc in the graph. Actually, in this case, the cost assigned to each arc should be an integer in the interval $[0, C]$. Dial's solution uses a circular queue with $C + 1$ buckets of nodes as the priority queue of the Dijkstra's algorithm. Since the bottleneck of the Dijkstra's algorithm is in maintaining the priority queue, Dial's solution uses the bucket sort algorithm to speed up this process. We will come back to this issue in Section 2.2.

In our problem, the live-wire segment between a selected point v_s on the boundary and the current position v_e of the cursor in C is the shortest-path $P = (v_s \sim v_e)$ from v_s to v_e in our graph, where the cost of P , denoted

$K(P)$, is the sum of the joint costs $c(b)$ of all bels b comprising P . In fact, Dijkstra's algorithm returns a tree of minimum-cost path (or a tree of shortest-path) rooted at v_s ,²¹ which consists of all minimum-cost paths from v_s to all vertices in C . We will denote this tree by $T(v_s) = \{P = (v_s \rightsquigarrow v_e) / v_e \in C\}$.

For any real number k , we denote by $T_k(v_s)$ the tree of minimum-cost path rooted at v_s such that the cost of any path in this tree is less than k . That is, $T_k(v_s) = \{P = (v_s \rightsquigarrow v_e) / v_e \in C, K(P) < k\}$. The algorithm reported in this paper exploits the following properties of $T(v_s)$.

1. To compute the minimum-cost path $P = (v_s \rightsquigarrow v_e)$ with cost $K(P)$, there is no need to compute $T_k(v_s)$ for $k > K(P)$.
2. By the time we have found the minimum-cost path $P = (v_s \rightsquigarrow v_e)$ with cost $K(P)$, we have actually found the tree of minimum-cost path $T_{K(P)}(v_s)$.
3. The tree of minimum-cost path $T_k(v_s)$ contains the tree of minimum-cost path $T_{K(P)}(v_s)$ whenever $k \geq K(P)$.

We use the first property to modify Dial's implementation of the Dijkstra's algorithm to quit optimum path computation by the time we have found the minimum-cost path $P = (v_s \rightsquigarrow v_e)$. We call this algorithm DSP (see Section 2.2). We use the second property to avoid optimum path computation for any path $P' = (v_s \rightsquigarrow v'_e)$ with cost $K(P') < K(P)$. Thus, when the user moves the cursor to a new position v'_e , such that $K(P') < K(P)$, and we have already found P , the algorithm just shows $P' = (v_s \rightsquigarrow v'_e)$ without requiring computation. We use the third property to continue optimum path computation for paths $P' = (v_s \rightsquigarrow v'_e)$ with costs $K(P') \geq K(P)$ based on the previous result of algorithm DSP for computing P .

2.2. ALGORITHMS

Algorithm LWOF

Input: The joint cost function c and an initial vertex v_0 selected on a 2D boundary of interest in C ;

Output: A closed, connected, and oriented contour B (made up of bels);

Auxiliary Data Structures: A 2D "cumulative cost" array cc representing the total cost of the optimal paths found so far from v_s to other vertices in C ; a 2D "direction" array dir indicating, for each vertex, to which of its immediate neighboring vertices the optimal path goes; a circular queue Q of vertices with $C+1$ buckets; a list L of vertices which have already been processed; a current path $P(v_s \rightsquigarrow v_e)$, where v_s is the current point selected on the boundary and v_e is the current position of the cursor in C ; and a list B of bels which have already been identified as belonging to the boundary of interest in C ;

begin

1. set $cc(v)$ to ∞ and $dir(v)$ to *null* for all vertices v in C , and set L to empty;
2. $v_s \leftarrow v_0$, set $cc(v_s)$ to 0, and put v_s in Q ;
3. *repeat*
 - a. determine the vertex v_e in C pointed to by the cursor;
 - b. if v_e is not a vertex of any bel in B then
 - (i) compute $P \leftarrow \text{DSP}(v_s, v_e, Q, cc, c, dir, L)$ and display the bels in P ;
 - (ii) if v_e is selected by the user and $v_e \in C$ then
 - a. add the bels in P to B ;
 - b. set $cc(v)$ to ∞ and $dir(v)$ to *null* for all vertices v in C ;
 - c. remove all vertices v from Q , and remove from L all vertices v which do not belong to any bel in B ;
 - d. $v_s \leftarrow v_e$, set $cc(v_s)$ to 0, remove v_s from L , and put v_s in Q ;

```

    endif;
endif;

until the user indicates a "close" operation;

4.  $v_e \leftarrow v_0$  and remove  $v_e$  from  $L$ ;
5. compute  $P \leftarrow \text{DSP}(v_s, v_e, Q, cc, c, \text{dir}, L)$  and display the bels in  $P$ ;
6. add the bels in  $P$  to  $B$  and output the bels in  $B$ ;

end

```

Algorithm DSP

Input: an initial vertex v_s ; a terminal vertex v_e ; the circular queue Q ; the cumulative cost array cc ; the joint cost function c ; the direction array dir ; and the list L of already processed vertices;
Output: A set of bels forming an optimal path from v_s to v_e ;

begin

1. *while* $v_e \notin L$ *do*
 - a. remove a vertex v from Q such that $cc(v) = \min_{v' \in Q} \{cc(v')\}$, and put v in L ;
 - b. *for each* vertex v' such that v' is in the set of the 4-adjacent neighbors of v and $v' \notin L$ *do*
 - (i) compute $cc_{tmp} = cc(v) + c(b')$ where b' is the bel whose direction goes from v' to v and $c(b')$ is the joint cost of b' ;
 - (ii) *if* $cc_{tmp} < cc(v')$ *then*
 - a. set $cc(v')$ to cc_{tmp} and $\text{dir}(v')$ to the direction from v' to v ;
 - b. *if* $v' \notin Q$ *then* insert v' in Q *else* update v' in Q ;
 - endif*,
 - endfor*,
- endwhile*;

2. starting from v_e , trace recursively the next vertex pointed to by the current vertex using the direction information in dir until v_s is reached, and return the bels so traced;

end

In the algorithms above, Q is a bucket represented by a circular vector with $C + 1$ positions from 0 to C (see Figure 1). Each position i , $i = 0, \dots, C$, has associated with it a doubly linked list which contains vertices with the same cumulative cost value. In Step 3b(ii)c of algorithm LWOF, we remove all vertices v from Q in $O(C)$ time since we just have to set to *null* the list associated with each position i , $i = 0, \dots, C$, in Q . An index i_0 is used to indicate the current initial position in Q (see Figure 1). In Step 1a of algorithm DSP, a vertex v in Q with the minimum cumulative cost $cc(v)$ is removed from the beginning of the doubly linked list at position i_0 . If this list is empty, i_0 is incremented until the next position in which a non-empty list is found. Taking the worst case, this operation has a computational time complexity of $O(C)$. In Step 1b(ii)b of algorithm DSP, a vertex v' with cumulative cost $cc(v')$ is inserted in Q at the beginning of the doubly linked list at position $[cc(v') \bmod (C + 1)]$. This operation has a computational time complexity of $O(1)$. The Dijkstra's algorithm guarantees that the vertices in Q will be always stored in the increasing order of cumulative cost, because the difference between the maximum and the minimum

cumulative costs of the vertices in Q is always less than or equal to C . In the same step, a vertex v' in Q may have its cumulative cost updated, meaning that we have found a new path from v , to v' with a cost less than the current cost $cc(v')$. In this case, we have to remove v' from its current position in Q and insert it into a new position in Q . This process is done with a computational time complexity of $O(1)$.

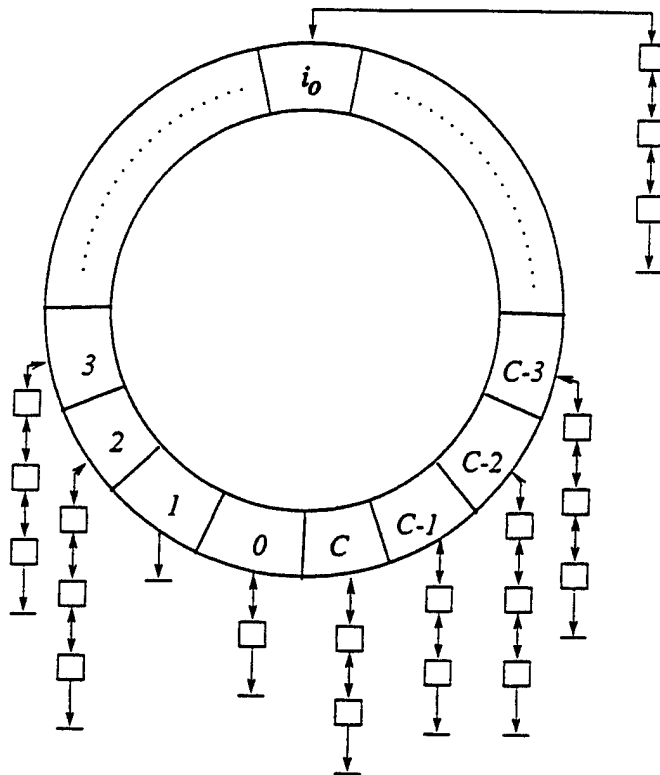


Figure 1. Bucket Structure in a *circular* queue.

In the worst case, algorithm DSP has the same computational time complexity $O(m + nC)$ as in the Dial's implementation of Dijkstra's algorithm, where m is the number of bels in C , n is the number of vertices in C and C is the maximum cost $c(b)$ assigned to any bel b . Other shortest-path algorithms exist with computational time complexity less than $O(m + nC)$ (e.g., $O(m + n \log C)$, $O(m + n\sqrt{\log C})$, and $O(m \log \log C)$, see²⁰). These algorithms use more complex data structures than our circular queue to reduce the time complexity for inserting and removing vertices. In our implementation, we have a time complexity of $O(1)$ for inserting and updating vertices in Q . In the worst case, we have a time complexity of $O(C)$ for removing a vertex from Q with minimum cumulative cost, as opposed to a logarithmic complexity obtained by these algorithms. After some experimentation, we have found that the number of increments to reach the next non-empty position in Q is usually less than 0.01 of C . Actually, even C is not a big number. Typically, we have used 4095 and 255 for C in our implementation of live wire. Therefore, it is not clear that the speed improvement in live wire with other algorithms is really significant. This should be investigated further.

3. EVALUATION

In⁶, we have assessed the goodness of a segmentation method based on three factors - precision, accuracy, and efficiency. Precision refers to the repeatability of the method and can be measured by evaluating the variations in the result of segmentation because of subjective operator input. Accuracy refers to the degree of agreement with truth. Efficiency refers to the practical viability of the method expressed as some function of the total user's time required to complete the segmentation process. Based on 2,000 tracings in a particular application and statistical analysis of the results, we have shown that the segmentations of the 2D live-wire method in general agree with those of manual tracing (accuracy) and that the live-wire method is more repeatable (precision), with a statistical

significance level of $p < 0.03$, and 1.5-2.5 times faster (efficiency), with a statistical significance level of $p < 0.02$, than the manual method. In this section, we will show the results of comparing live wire and live wire on the fly taking into account the efficiency of the methods. Since the delineation of the contours output by live wire on the fly is exactly in the same way as in live wire, the accuracy and precision of the former will be identical to those of the latter, and, therefore, they need not be assessed again.

In,⁶ we have introduced a feature called f_8 in live wire to constrain the search for optimal paths in the current slice to an annular region (shell) of width W centered around the projection onto the current slice of the contour(s) traced in the previous slice. With feature f_8 , live wire yields very fast response even for large images. Of course, we can also use f_8 to further improve the efficiency of live wire on the fly on large images, but we will consider in this section a comparison between live wire with f_8 and live wire on the fly. Therefore, our experiments will take into account three methods:

- LW: live wire without f_8 .
- LWF8: live wire with f_8 using $W = 60$ pixels.
- LWOF: live wire on the fly.

For our experiments, we have chosen one object (the talus bone of the human foot) in one of our ongoing applications, the kinematic analysis of the tarsal joints of the foot based on MR images.⁹⁻¹¹ This was one of the objects used in the past to evaluate the previous live methods.^{6,16} We created a set of 67 2D scenes from the images within our database as follows. The images (slices) in our database are all of size 256×256 pixels. We chose a set, denoted C_{256} , of 30 slices from this set pertaining to the data set of one subject. By bilinear interpolation of each of these slices, we created another set, denoted C_{128} , of 30 128×128 slices. Analogously, we created a set C_{512} of five 512×512 slices and a set C_{1024} of two 1024×1024 slices from the original 256×256 slices. The reason for choosing a fewer number of scenes of size 512×512 and 1024×1024 is that the response time of LW in these scenes is prohibitively slow. One operator segmented the talus in each of these scenes using each of the two methods LW and LWOF. He also segmented the talus in C_{256} using LWF8. Our evaluation study thus consists of 164 segmentation experiments in total. More experiments involving other operators are currently underway. We used a 300 MHz Pentium PC for these experiments.

We denote the *time taken* to complete any segmentation experiment e by T_e (expressed in seconds). Consider any fixed scene type $t \in \{C_{128}, C_{256}, C_{512}, C_{1024}\}$ and method $m \in \{LW, LWOF, LWF8\}$. We define the *time taken* T_{tm} (in seconds/slice) for segmenting the talus in a 2D scene of type t using method m to be the average of all times T_e over all segmentation experiments e involving m and all 2D scenes of type t .

We have done three types of timing measurements. The first type measures the CPU times for computing the live wire segments independent of other supporting processes that are required to conduct live wire segmentation. This allows us to assess the difference in speed that exists purely between the old and the new algorithms. The second type measures the time taken by the user to segment one complete contour ignoring the time for other processes such as displaying the slice and the computation of the cost values $c(b)$ for all belts. The third type includes all processes, and, therefore, gives an idea of the comparative user time required for overall segmentation for the different methods in an actual application. We note here that, as in the live-wire method,⁶ training is required only once for an application and is not needed on a per study basis. This is typically under 5 minutes and is not included in any of the time measurements.

Tables 1, 2 and 3 list the values of T_{tm} for all possible values of t and m , for the three types of measures, respectively. Although *LWOF* can find optimum paths hundreds of times faster than *LW* (see Table 1), users cannot react with the same speed (see Table 2). Table 3 shows that, from the point of view of actual segmentation, *LWOF* is about 1.5 to 33 times faster than *LW* for images from 128×128 pixels to 1024×1024 pixels. Even constraining optimum path computation into an annular region of width equal to 60 pixels (i.e., method *LWF8*), live wire on the fly is about 2.3 times faster. Note that, the advantage of live wire on the fly over live wire increases with the size of the image and with the number of points required per boundary. In our experiments, the 2D boundaries of the talus require 2 to 5 points in both live wire strategies.

| | C ₁₂₈ | C ₂₅₆ | C ₅₁₂ | C ₁₀₂₄ |
|------|------------------|------------------|------------------|-------------------|
| LW | 2.14 | 15.17 | 99.57 | 901.24 |
| LWOF | 0.23 | 0.62 | 2.27 | 8.74 |
| LWF8 | — | 8.25 | — | — |

Table 1. Segmentation times T_{tm} in seconds/slice for all possible values of t and m . This table lists the first type of measurement that indicates the time taken by the shortest-path algorithms only independent of other processes.

| | C ₁₂₈ | C ₂₅₆ | C ₅₁₂ | C ₁₀₂₄ |
|------|------------------|------------------|------------------|-------------------|
| LW | 8.37 | 20.93 | 116.20 | 959.00 |
| LWOF | 5.67 | 5.33 | 8.00 | 15.50 |
| LWF8 | — | 14.13 | — | — |

Table 2. Segmentation times T_{tm} in seconds/slice for all possible values of t and m . This table lists the second type of measurement that indicates the time taken by the user to segment one complete contour ignoring the time for other processes.

| | C ₁₂₈ | C ₂₅₆ | C ₅₁₂ | C ₁₀₂₄ |
|------|------------------|------------------|------------------|-------------------|
| LW | 12 | 24 | 120 | 990 |
| LWOF | 8 | 8 | 12 | 30 |
| LWF8 | — | 18 | — | — |

Table 3. Segmentation times T_{tm} in seconds/slice for all possible values of t and m . This table lists the third type of measurement that indicates the time taken by the user for overall segmentation including all processes.

4. CONCLUDING REMARKS

We have presented a new user-steered image segmentation paradigm, called live wire on the fly, to segment 3D/4D object boundaries in a slice-by-slice fashion. The method uses the previously published live wire framework,⁶ but utilizes a substantially faster shortest-path algorithm for improving speed. Based on 164 segmentation experiments from an actual medical application, we have shown that the new method is about 1.5 to 33 times faster than live wire for actual segmentation, although the pure computational part alone is over a hundred times faster. Other experiments involving multiple operators are being done.

A drawback of live wire is the computation time for all possible minimum-cost segments from each selected point on the boundary to all other points in the image. This time increases with the size of the image compromising the interactivity of the method in some practical situations. Tables 1- 3 show that live wire loses efficiency considerably for images larger than 256×256 pixels. We have eliminated this problem in live wire on the fly by avoiding unnecessary optimum path computation during the segmentation process. Thus, live wire on the fly computes and displays live-wire segments in real time, even for very large images, even on low-powered computers.

ACKNOWLEDGMENTS

The work of the first author (A.X.F.) was partially supported by FAPESP (Proc. 98/06314-5 and Proc. 97/13306-6). The research of the second author is supported by an NIH grant NS 37172 and a grant DAMD 179717271 from the Department of Army. The third author (F.K.M.) has been partially supported by Project ProNEx 107/97 (MCT/FINEP) and CNPq individual research grants: Proc. 300301/98-7.

REFERENCES

1. R.M. Haralick and L.G. Shapiro, Image segmentation techniques, *Computer Vision Graphics and Image Processing*, vol. 29, no. 1, pp. 100-132, Jan, 1985.
2. S.D. Olabarriaga and A.W.M. Smeulders, Setting the mind for intelligent interactive segmentation: Overview, requirements, and framework, *Lecture Notes on Computer Science*, vol. 1230, pp. 417-422, 1997.
3. W.E. Higgins and E.J. Ojard, Interactive morphological watershed analysis for 3D medical images, *Computerized Medical Imaging and Graphics*, vol. 17, no. 4/5, pp. 387-395, 1993.
4. R. Adams and L. Bischof, Seeded Region Growing, *IEEE Transactions on Pattern Analysis and Machine Intelligence*, vol. 16, no. 6, pp 641-647, Jun, 1994.
5. T. McInerney and D. Terzopoulos, Deformable models in medical image analysis: A survey, *Medical Image Analysis*, vol. 1, no. 2, pp. 91-108, 1996.
6. A.X. Falcão, J.K. Udupa, S. Samarasekera, S. Sharma, B.E. Hirsch, and R.A. Lotufo, User-steered image segmentation paradigms: live-wire and live-lane, *Graphical Models and Image Processing*, vol. 60, no. 4, pp. 233-260, Jul, 1998.
7. E.N. Mortensen and W.A. Barrett, Interactive segmentation with intelligent scissors. *Graphical Models and Image Processing*, vol. 60, no. 5, pp. 349-384, Sep, 1998.
8. A.X. Falcão, J.K. Udupa, S. Samarasekera and B.E. Hirsch, User-steered image boundary segmentation, in *Proceedings of SPIE on Medical Imaging*, Newport Beach, CA, vol. 2710, pp. 278-288, Feb, 1996.
9. J.K. Udupa, B.E. Hirsch, S. Samarasekera, H. Hillstrom, G. Bauer, and B. Kneeland, Analysis of in vivo 3D internal kinematics of the joints of the foot, *IEEE Transactions on Biomedical Engineering*, vol. 45, pp. 1387-1396, 1998.
10. B.E. Hirsch, J.K. Udupa, and S. Samarasekera, A new method of studying joint kinematics from 3D reconstructions of MRI data, *Journal of the American Podiatric Medical Association*, vol. 86, no. 1, pp. 4-15, 1996.
11. E. Stindel, J.K. Udupa, B.E. Hirsch, D. Odhner, and C. Couture, 3D MR image analysis of the morphology of the rear foot: Application to classification of bones, *Journal of Bone and Joint Surgery*, submitted.
12. R.C. Rhoad, J.J. Klimkiewicz, G.R. Williams, S.B. Kesmodel, J.K. Udupa, B. Kneeland, and J.P. Iannotti, A new in vivo technique for 3D shoulder kinematics analysis, *Skeletal Radiology*, vol. 27, pp. 92-97, 1998.
13. B.S. Morse, W.A. Barrett, J.K. Udupa, and R.P. Burton, Trainable optimal boundary finding using two-dimensional dynamic programming, *Technical Report MIPG180*, Medical Image Processing Group, Department of Radiology, University of Pennsylvania, Mar, 1991.
14. J.K. Udupa, S. Samarasekera, W.A. Barrett, Boundary detection via dynamic programming, in *Proceedings of SPIE*, vol. 1808, pp. 33-39, 1992.
15. E.N. Mortensen, B.S. Morse, W.A. Barrett and J.K. Udupa, Adaptive boundary detection using live-wire two dimensional dynamic programming, in *IEEE Proceedings of Computers in Cardiology*, pp. 635-638, Oct, 1992.
16. A.X. Falcão and J.K. Udupa, Segmentation of 3D objects using live-wire, in *Proceedings of SPIE on Medical Imaging*, Newport Beach, C, vol. 3034, pp. 228-239, Feb, 1997.
17. E.N. Mortensen and W.A. Barrett, Intelligent scissors for image composition, in *Proceedings of Computer Graphics (SIGGRAPH'95)*, Los Angeles, C, pp. 191-198, Aug, 1995.
18. W.A. Barrett and E.N. Mortensen, Fast, accurate, and reproducible live-wire boundary extraction, in *Proceedings of Visualization in Biomedical Computing*, Hamburg, Germany, pp. 183-192, Sep, 1996.
19. N. Deo and C. Pang, Shortest-path algorithms: Taxonomy and annotation, *Networks*, vol. 14, pp. 275-323, 1984.
20. R.K. Ahuja, T.L. Magnanti and J.B. Orlin, *Network Flows: Theory, Algorithms and Applications*, Prentice-Hall, Englewood Cliffs, NJ, 1993.
21. R.E. Tarjan, *Data Structures and Network Algorithms*, Society for Industrial and Applied Mathematics, Philadelphia, PA, 1983 (sixth printing in 1991).

Breast tissue density quantification via digitized mammograms

Punam K. Saha, Jayaram K. Udupa

Emily F. Conant, Dev P. Chakraborty

Department of Radiology, University of Pennsylvania

Philadelphia, PA 19104

Daniel Sullivan

National Cancer Institute – EPN – 800

6130 Executive Blvd., Rockville, Maryland, MD 20852

Correspondence: Jayaram K. Udupa

Medical Image Processing Group, Department of Radiology

University of Pennsylvania

4th floor, Blockley Hall, 423 Guardian Drive

Philadelphia, PA 19104-6021

Email: jay@mipg.upenn.edu

Tel: (215)-662-6780, Fax: (215)-898-9145

Abstract

Studies reported in the literature indicate that breast cancer risk is associated with mammographic densities. An objective, repeatable, and a quantitative measure of risk derived from mammographic densities will be of considerable use in recommending alternative screening paradigms and/or preventive measures. However, image processing efforts toward this goal seem to be sparse in the literature, and automatic and efficient methods do not seem to exist. In this paper, we describe and validate an automatic and reproducible method to segment dense tissue regions from fat within breasts from digitized mammograms using scale-based fuzzy connectivity methods. Different measures for characterizing mammographic density are computed from the segmented regions and their robustness in terms of their linear correlation across two different projections (CC and MLO) are studied. The accuracy of the method is studied by computing the area of mismatch of segmented dense regions using the proposed method and using manual outlining. A comparison between the mammographic density parameter taking into account the original intensities and that just considering the segmented area is demonstrated which indicates that the former may have some advantages over the latter.

Keywords: Image analysis, mammograms, glandular tissue, image segmentation, fuzzy connectedness.

I. INTRODUCTION

In the mid 1970s, studies by John Wolfe [1], [2] suggested that an association existed between mammographic parenchymal patterns and the risk of developing breast cancer. Since then there have been many studies looking at the relationship between mammographic fibroglandular density (often referred to as just density) and the risk of developing breast cancer. Although a few studies reported no association of density with increased risk, the majority of studies have found an association between parenchymal patterns and breast cancer risk. A recent meta-analysis [3] of all studies confirms that subjects with mammographic densities have an increased risk of breast cancer relative to those without densities. The risk increases with the density of the breast [4]. Women with dense breasts are known to have a four to six fold increase in breast cancer risk [1], [5], [6]. Cancers are detected at later stages in dense breasts and mammographers recognize that their diagnostic accuracy is lower in such women.

The Wolfe classification was proposed many years ago to identify groups of women at high risk for breast cancer [5]. This scheme was widely used for many years, but has fallen into disuse because of several limitations. For example, inter-observer variability is a problem when the radiologists' subjective assessment is used to classify the amount of density present [7]. Secondly, the magnitude of the increased risk has varied widely in the published studies [3]. Thirdly, identification of this risk factor for a given woman has not altered screening recommendations [6], [8]. Computer-assisted analysis of mammographic density would provide an objective, quantitative measure of cancer risk factor. This measure will be useful in total risk analysis in several ways. First, such risk analysis could influence the choice of alternative screening paradigms such as intervals between mammograms or use of other modalities such as MRI. Second, this measure could be useful in selecting a group of women for whom the risk-benefit ratio of a potentially toxic preventive measure, such as tamoxifin, would be favorable [16], [17]. Third, this measure could be used to signal the need for more careful interpretation of a subset of mammograms. For example, double-reading might be indicated for mammograms above a certain level of density.

Image processing efforts toward this goal seem to be sparse in the literature, and au-

tomatic and efficient methods for generating this measure do not seem to exist. Boyd et. al. [6] studied the relation between mammographic densities and breast cancer risk using both radiologist classification and computer-assisted density measurement. The computer-assisted measurement was based on interactive density thresholding using two user-selected thresholds. They observed statistically significant increases in breast cancer risk associated with increasing mammographic density in both methods. Boone et. al. [18] developed and evaluated a computerized method of calculating a breast density index and compared this index with breast density index ranking provided by mammographers. Byng et. al. [19] made a quantitative symmetry analysis between mammograms of different breasts of the same patient and between mammograms at different projections of the same breast via subjective classification, interactive thresholding, regional skewness measurement, and texture analysis. Ursin et. al. [20] studied the change in mammographic densities in women participating in a trial of a gonadotropin-releasing hormone agonist (GnRHA)-based regimen for breast cancer prevention using simultaneous evaluation, expert outlining, and non-expert computer-based thresholding methods. They observed that all three methods yielded statistically significant reduction in densities from baseline to the 12-month follow-up mammogram in women on the contraceptive regimen. They found a high correlation between computer-based results and the results from the expert outlining method. Huo et. al. [21] studied the ability of computer-extracted features, computed over a region of interest selected from the central breast region, along with age, to identify women at risk. They found that a computerized characterization of parenchymal patterns may be associated with breast cancer risk. An automatic method for segmenting the parenchymal region of a mammogram using first and second order gray-level histograms is presented in [22]. Another approach is presented in [23] for determining the volume of non fatty tissues in mammograms. Recently a computer-assisted user-interactive method to quantify mammographic density has been published [6], which concluded that quantitative classification of densities allows for the determination of more specific gradients of risk than do Wolfe's classifications.

In this paper, we describe and validate an automatic and reproducible method to quantify mammographic densities and study the accuracy of related parameters. In Section II,

a brief description of the principles of the scale-based fuzzy connectedness method which forms the core of the proposed method is presented. In section III, we describe how different parameters are automatically selected for applying fuzzy connectivity on different regions. In Section IV, we discuss the results and validate the method — (1) by studying linear correlations of different area and density related parameters obtained from a set of mammograms across two projections and (2) by studying the accuracy of the method by computing the area of mismatch between the dense regions estimated by the new method and by manual outlining. A comparison between the mammographic density parameter taking into account the original intensities and that just considering the segmented area is demonstrated. Finally, we state our conclusions in Section V.

II. SCALE-BASED FUZZY CONNECTEDNESS PRINCIPLES

The concepts described here are applicable to n -dimensional (fuzzy) digital spaces; see [24], [25] for details. However, since our application deals with two-dimensional (2D) images, we confine ourselves only to the 2D case.

Most real objects have a heterogeneous material composition. Further, imaging devices have inherent limitations including spatial, parametric, and temporal resolutions. In the acquired images of objects, these introduce inaccuracies and artifacts such as noise, blurring, and background variation. The artifacts together with material heterogeneity cause the object regions to exhibit a gradation of intensity values in the image. Even if the physical object is perfectly homogeneous and is made of exactly one material, its image will exhibit a graded composition within the object regions due to artifacts. In spite of the graded composition, knowledgeable human observers usually do not have difficulties in perceiving object regions as an integrated whole. That is, image elements in these regions seem to hang together to form the object regions in spite of their gradation of values. These two notions — graded composition and hanging togetherness — must be handled properly by any segmentation method for effective, robust performance. In our methods, they are addressed by a fuzzy relation among image elements called fuzzy connectedness [24], [25]. Such a general, sound, theoretic and algorithmic framework for segmentation greatly facilitates the quick development of new segmentation applications, as we have demonstrated for fuzzy connectedness in brain image analysis [10], [11], [12], [13], MRA

[14], and craniofacial soft tissue display [15].

The scale-based method is briefly outlined below to the extent needed to follow our breast segmentation approach. The full details of its theory are given in [25]. We will be dealing with two object regions in our segmentation method as described in Section III. The first corresponds to the background region in the mammographic image and the second corresponds to the dense region. In the description in the rest of this section, “object region” refers to each of these regions.

Throughout we denote the digitized mammographic image, referred to as a (2D) *scene*, by $\mathcal{C} = (C, f)$, where C denotes the pixel array, and $f(c)$ denotes the pixel value for any pixel $c \in C$. For any pixel $c \in C$, we think of c as a pair (c_1, c_2) representing the two coordinates of the center of c . The range of f is assumed to be $[L, H]$, where L and H are integers.

We define a fuzzy relation κ , called *fuzzy affinity*, on the pixel array C . This is intended to be a local relation among pixels that are nearby. The strength of this relation between any two pixels c and d in C , denoted by $\mu_\kappa(c, d)$, lies in $[0, 1]$. It consists of three components: a fuzzy adjacency component α , a component ψ based on object homogeneity, and a component ϕ based on object features. The idea is that when c and d are more adjacent, have more homogeneity of intensities, and are both very close to an expected object feature value, then c and d have high affinity. In other words, they hang together locally very strongly. α depends on how far c and d are. ψ depends on how similar the intensity values (or other features) of the pixels in a neighborhood around c are to those around d . ϕ depends on how close the intensities (or other features) of the pixels around c and those around d are to some expected values of the intensities (or other features) for the object under consideration. We denote the strengths of all these three components (all of which lie in $[0, 1]$) by $\mu_\alpha(c, d)$, $\mu_\psi(c, d)$ and $\mu_\phi(c, d)$, respectively. We describe below the functional forms utilized for these components.

Although the theory permits more general forms, in this paper, we use the following functional form for μ_α . For any pixel c , $\mu_\alpha(c, c) = 1$. Further, for any two pixels c, d , $\mu_\alpha(c, d) = 1$ if c and d differ in exactly one coordinate by 1; otherwise $\mu_\alpha(c, d) = 0$. The specification of both μ_ψ and μ_ϕ requires the notion of “object scale” at every pixel in \mathcal{C} . The

idea behind this notion is that if we can roughly estimate the size of the object structure locally at every pixel, then this information can be utilized to determine a neighborhood size around c and d for specifying μ_ψ and μ_ϕ in a way that is tuned to the object and is independent of pixel-level variation due to noise. The *object scale* $r(c)$ in C at any pixel c in C denotes the size (radius) of the largest disc centered at c that lies entirely in the object region in which c lies. Paradoxically, it appears that computing scale requires image segmentation. It is possible, however, to develop algorithms that give a rough estimate of object scale at every pixel based on measuring intensity homogeneity discontinuities and that do not require explicit image segmentation. We have demonstrated in [25] that this estimation is sufficient to give a good approximation of the scale and to make the fuzzy-connectedness-based segmentation very robust to noise and pixel-level variations. For now, we assume that $r(c)$ is known at any $c \in C$. In determining the scale-based fuzzy affinity between any pixels $c, d \in C$, two digital discs, centered at c and d , denoted $B_{cd}(c)$ and $B_{cd}(d)$, both of radius $\min[r(c), r(d)]$, defined by

$$B_{cd}(c) = \{e \in C \mid \|c - e\| \leq \min[r(c), r(d)]\}, \quad (1)$$

$$B_{cd}(d) = \{e \in C \mid \|d - e\| \leq \min[r(c), r(d)]\}, \quad (2)$$

where $\|\cdot\|$ denotes the Euclidean distance, are utilized.

For defining μ_ψ , consider any two pixels $c, d \in C$ such that $\mu_\alpha(c, d) > 0$. Consider any pixels $e \in B_{cd}(c)$ and $e' \in B_{cd}(d)$ such that they represent the corresponding pixels within $B_{cd}(c)$ and $B_{cd}(d)$; that is, $c - e = d - e'$. We will define two weighted sums $D^+(c, d)$ and $D^-(c, d)$ of the differences of intensities between the two discs as follows. Let

$$\delta_{cd}^+(e, e') = \begin{cases} f(e) - f(e'), & \text{if } f(e) - f(e') > 0, \\ 0, & \text{otherwise,} \end{cases} \quad (3)$$

$$\delta_{cd}^-(e, e') = \begin{cases} f(e') - f(e), & \text{if } f(e) - f(e') < 0, \\ 0, & \text{otherwise.} \end{cases} \quad (4)$$

Then

$$D^+(c, d) = \sum_{\substack{e \in B_{cd}(c) \\ e' \in B_{cd}(d) \\ \text{s.t. } c - e = d - e'}} [1 - G_{0, m_\psi + 3\sigma_\psi}(\delta_{cd}^+(e, e'))] G_{0, \min[r(c), r(d)]}(\|c - e\|), \quad (5)$$

$$D^-(c, d) = \sum_{\substack{e \in B_{cd}(c) \\ e' \in B_{cd}(d) \\ \text{s.t. } c - e = d - e'}} [1 - G_{0, m_\psi + 3\sigma_\psi}(\delta_{cd}^-(e, e'))] G_{0, \min[r(c), r(d)]}(\|c - e\|), \quad (6)$$

where “s.t.” denotes “such that”; $G_{m, \sigma}$ denotes an unnormalized Gaussian with mean m and standard deviation σ ; m_ψ and σ_ψ are, respectively, the expected mean and standard deviation of intensity differences between all pairs of adjacent pixels within the object region; $\|c - e\|$ represents the distance between c and e . We will describe in the next section how these parameters are estimated for breast images.

The connection of the above equations to the homogeneity-based affinity μ_ψ is as follows. There are two types of intensity variations surrounding c and d — intra- and inter-object variations. The intra-object component is generally random, and therefore, is likely to be near 0 overall. The inter-object component, however, has a direction. It either increases or decreases along the direction given by $c - d$, and is likely to be larger than the intra-object variation. It is reasonable, therefore, to assume that the smaller of $D^+(c, d)$ and $D^-(c, d)$ represents the intra-object component and the other represents the combined effect of the two components. (Note that when the values of δ_{cd}^+ (respectively, δ_{cd}^-) are small, $D^+(c, d)$ (respectively, $D^-(c, d)$) also becomes small.) If there is a slow background component of variation, within the small neighborhood considered, this component is unlikely to cause a variation comparable to the inter-object component. This strategy leads us to the following functional form for μ_ψ :

$$\mu_\psi(c, d) = 1 - \frac{|D^+(c, d) - D^-(c, d)|}{\sum_{e \in B_{cd}(c)} G_{0, \min[r(c), r(d)]}(\|c - e\|)}. \quad (7)$$

Note that $|D^+(c, d) - D^-(c, d)|$ represents the degree of local inhomogeneity of the regions containing c and d . Its value is low when both c and d are inside an (homogeneous) object

region. Its value is high when c and d are in the vicinity of (or across) a boundary. The denominator in (7) is a normalization factor.

For completing the specification of μ_ψ , the values of three parameters $r(c)$, m_ψ and σ_ψ need to be determined. The method of estimating $r(c)$ is independent of the type of object region to be segmented and will be described later in this section. The method of estimating m_ψ and σ_ψ is specific to the object region and will be explained in Sections III-A and III-B.

For defining the object-feature-based affinity, μ_ϕ , we first compute scale-based filtered intensity value at c that takes into account the disc $B_r(c)$ defined by

$$B_r(c) = \{e \in C \mid \|c - e\| \leq r(c)\}. \quad (8)$$

The filtered intensity value at any $c \in C$ is given by

$$f_a(c) = \frac{\sum_{e \in B_r(c)} f(e) G_{0,r(c)}(\|c - e\|)}{\sum_{e \in B_r(c)} G_{0,r(c)}(\|c - e\|)}. \quad (9)$$

Depending on whether the object of interest is darker or lighter, we define the following function utilized in defining μ_ϕ .

Object is darker:

$$W_\phi(c) = \begin{cases} 1, & \text{if } f_a(c) < m_\phi, \\ G_{m_\phi, \sigma_\phi}(f_a(c)), & \text{otherwise.} \end{cases} \quad (10)$$

Object is lighter:

$$W_\phi(c) = \begin{cases} G_{m_\phi, \sigma_\phi}(f_a(c)), & \text{if } f_a(c) < m_\phi, \\ 1, & \text{otherwise.} \end{cases} \quad (11)$$

In both cases, m_ϕ and σ_ϕ represent the expected mean and standard deviation of the intensities in the object region, respectively. Finally, the following functional form is used for μ_ϕ :

$$\mu_\phi(c, d) = \begin{cases} 1, & \text{if } c = d, \\ \min[W_\phi(c), W_\phi(d)], & \text{otherwise.} \end{cases} \quad (12)$$

For completing the specification of μ_ϕ , the values of three parameters $r(c)$, m_ϕ and σ_ϕ need to be determined. The method of estimating $r(c)$ is presented below. The method of estimating m_ϕ and σ_ϕ is specific to the type of object region to be segmented and will

be explained in Sections III-A and III-B. Finally, the three components of affinity are combined as follows to define the scale-based fuzzy affinity, μ_κ

$$\mu_\kappa(c, d) = \mu_\alpha(c, d) \sqrt{\mu_\psi(c, d) \mu_\phi(c, d)}. \quad (13)$$

We now describe an algorithm for estimating object scale at every pixel. For a disc $B_k(c)$ of any radius k (see (8)) centered at c , we define a fraction, $FO_k(c)$, that indicates the fraction of the disc boundary occupied by a region in which the scene is sufficiently homogeneous with c , by

$$FO_k(c) = \frac{\sum_{d \in B_k(c) - B_{k-1}(c)} G_{0, m_\psi + 3\sigma_\psi}(|f(c) - f(d)|)}{|B_k(c) - B_{k-1}(c)|}. \quad (14)$$

Here $|B_k(c) - B_{k-1}(c)|$ denotes the number of pixels in $B_k(c) - B_{k-1}(c)$. We define $B_0(c)$ to be simply the set $\{c\}$. The algorithm for object scale estimation (*OSE*) is summarized below. The algorithm iteratively increases the disc radius k by 1, starting from 1, and checks for the fraction of the object $FO_k(c)$ containing c that is contained on the disc perimeter. The first time when this fraction falls below a pre-selected threshold t_s , we consider that the disc enters into an object region different from that to which c belongs. Following the arguments in [25], we have used $t_s = 0.85$.

Algorithm *OSE*

Input: $\mathcal{C}, c \in C, m_\psi, \sigma_\psi$, a fixed threshold t_s .

Output: $r(c)$.

begin

```

set  $k = 1$ ;
while  $FO_k(c) \geq t_s$  do
    set  $k$  to  $k + 1$ ;
endwhile;
set  $r(c)$  to  $k$ ;
output  $r(c)$ ;
```

end

The notion of pixel affinity captures the local hanging-togetherness property of pixels. The notion of fuzzy connectedness expands this into a global phenomenon as follows.

Consider any two pixels c and d (not necessarily nearby) in C . (Note that when c and d are far apart, their affinity is 0.) Consider any path (i.e., a sequence of nearby pixels) starting from c and ending in d . We define a “strength of connectedness” of this path as simply the smallest affinity (weakest link) along the path between a pair of successive pixels in the path. Fuzzy connectedness is a global fuzzy relation, denoted K , on C . The strength of this relation between c and d (not necessarily nearby), denoted $\mu_K(c, d)$, is the largest of the strength of connectedness of *all possible* paths between c and d . A scale-based fuzzy connected object of C of strength θ , for any $\theta \in [0, 1]$, that contains a specified pixel o in C is a subset O of pixels of C . O is such that, for any two pixels c, d in O , $\mu_K(c, d) \geq \theta$, and for any pixel e not in O , $\mu_K(c, e) < \theta$. Given C , o , θ and a scale-based affinity relation κ , finding O requires the computation of the strength of connectedness of literally all possible paths between each pair of pixels in the set of all possible pairs of pixels in C . However, the theory leads to practically viable algorithms [24], [25] of far less complexity that are based on dynamic programming. We make use of these algorithms in our application.

For any scene $\mathcal{C} = (C, f)$, any fuzzy affinity κ , any pixel o in C , we define the *fuzzy connectivity scene* of \mathcal{C} with respect to o to be the scene $\mathcal{C}_{Ko} = (C, f_{Ko})$, where for any $c \in C$, $f_{Ko}(c) = \mu_K(o, c)$. That is, the value assigned to any pixel c in \mathcal{C}_{Ko} is the strength of connectedness of c and o . We generalize this definition from a single pixel o to a set of pixels X by setting $f_{KX}(c) = \max_{x \in X} \{\mu_K(x, c)\}$. That is, in the fuzzy connectivity scene $\mathcal{C}_{KX} = (C, f_{KX})$ of \mathcal{C} with respect to X , any pixel c is assigned a value $f_{KX}(c)$ that is the maximum of the strength of connectivity of c with the elements of X . Connectivity scenes are what are output by the fuzzy connectedness algorithms [24], [25]. Upon thresholding them, we get the segmented fuzzy objects.

III. DENSITY QUANTIFICATION

Our method of mammographic density quantification consists of the following steps: (1) segmentation of the breast region from background; (2) segmentation of fat and dense regions within the breast; (3) estimation of the parameters representing quantified density. These are described in separate subsections below.

A. Segmentation of Breast from Background

At the very beginning, using 3DVIEWNIX [26] supported live-wire [27] tools, regions corresponding to pectoral muscles are interactively excluded when those are projected on to the scene. This tool takes help from the operator in recognizing where the pectoral muscles are in the image but does the delineation of their boundary automatically. In this fashion, subjectivity is minimized. In the entire process of density quantification, this is the only step requiring operator intervention, if pectoral muscles appear in the mammographic projection. Scale-based fuzzy connectivity is used for segmenting the breast region from the background. Our approach will be to segment the background region rather than the breast region. To do this, we need to (1) determine the values of the parameters m_ψ , σ_ψ , m_ϕ , and σ_ϕ for the background; and (2) specify a set of pixels in the background region. These are accomplished automatically as described below.

In this study, we have utilized 120 mammograms from 60 patients, each in two projections — MLO and CC. Studying all the 120 mammograms, we found that intensity histograms of mammograms always contain a prominent peak at low intensities, and this mode corresponds to the background. A typical histogram is shown in Figure 1. The first

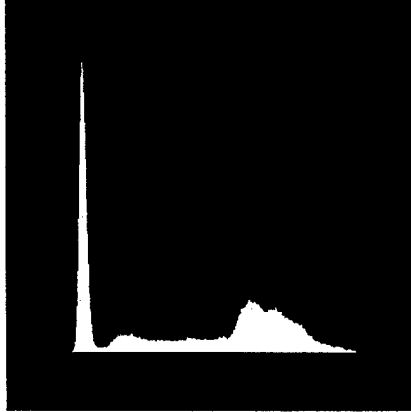


Fig. 1. A typical mammographic intensity histogram.

prominent peak in the histogram is detected and the intensity m_ϕ corresponding to this peak is considered as the mean background intensity. Observing that this part of the histogram is roughly symmetric about m_ϕ , the standard deviation of background intensities σ_ϕ is computed as the root-mean-squared distance of the intensities from m_ϕ as follows.

Let $h(i)$ represent the number of pixels in the mammographic scene with intensity i (i.e., $h(i)$ is the height of the histogram at i). Then, σ_ϕ is determined as follows

$$\sigma_\phi = \sqrt{\frac{\sum_{L \leq i \leq m_\phi} (i - m_\phi)^2 h(i)}{\sum_{L \leq i \leq m_\phi} h(i)}}. \quad (15)$$

In this application, since the object of interest (i.e., the mammographic background) is darker, we use the functional form of (10) for computing object-feature-based affinity. Instead of an operator painting pixels in the background region for training, the set of pixels in \mathcal{C} satisfying $L \leq f(c) \leq m_\phi + 3\sigma_\phi$ is utilized for estimating the parameters m_ψ and σ_ψ for homogeneity-based affinity μ_ψ . m_ψ and σ_ψ are taken to be simply the mean and the standard deviation of intensity differences between all pairs of adjacent pixels in this set.

During digitization, all mammograms were oriented so that the top-right and the bottom-right corners always lie in the background. (This was standardized for both left and right breasts.) These two corner pixels are used to form the reference set X for scale-based fuzzy connectedness processing. Figure 2(b) shows the connectivity scene obtained for the mammogram at CC projection shown in Figure 2(a). As shown in Figure 2(b), there is very good contrast between the background and the breast region in this connectivity scene. We discard connectivity strengths greater than half the maximum strength and keep the lower half as the zone for the breast region. This zone, however, often includes high noise pixels and markers in the background often used during mammography. To eliminate these pixels, the leftmost 1-pixel in the middle row in the thresholded connectivity scene is chosen as the reference pixel and the hard connected component containing this pixel is found as the breast region. Figure 2(c) shows the hard segmented breast region for the original mammogram of Figure 2(a). This method has worked correctly and automatically in all studies we have analyzed so far.

B. Segmentation of Fat and Dense Regions

Our strategy here is to segment the dense region as a set of fuzzy connected objects. The segmentation operation is confined to the breast region. The fat region thus gets defined indirectly as the complement of the dense region in the breast. For this segmentation, as

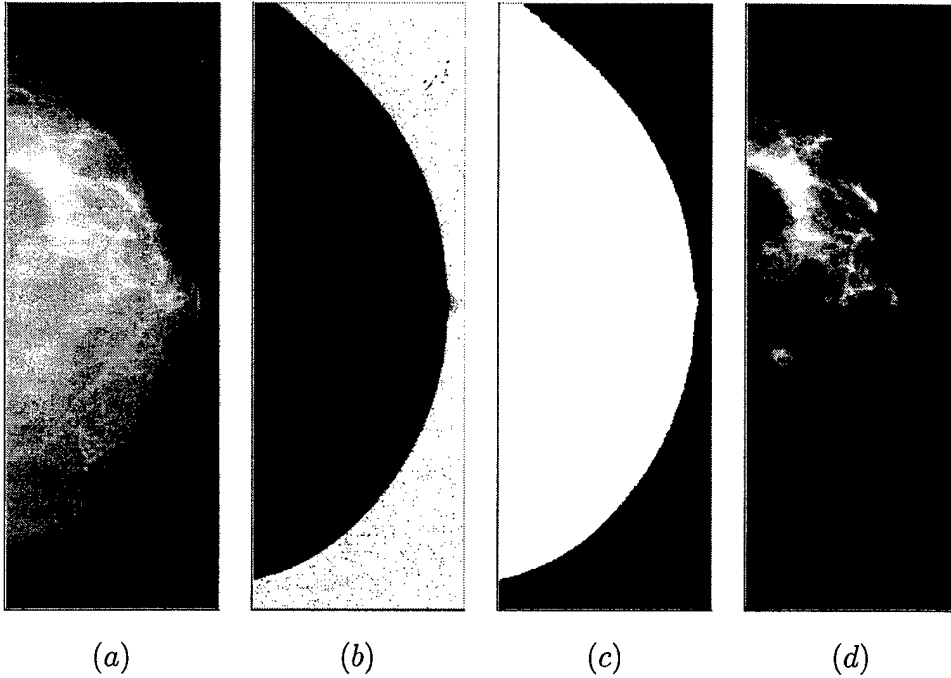


Fig. 2. (a) An original mammographic scene of a patient's breast at CC projection. (b) Scale-based fuzzy connectivity scene for the background. (c) Segmented breast region. (d) Scale based fuzzy connectivity scene for the dense region.

in breast segmentation, we need to specify the values of parameters m_ψ , σ_ψ , m_ϕ , and σ_ϕ for the dense region as well as a few pixels as the starting information in the dense region.

Our approach to computing the parameters will be as for the segmentation of the breast region — to determine automatically a set of pixels that are definitely in the dense region and then to estimate the parameters from the intensity distribution within this set of pixels. In this application, since the object of interest (i.e., the dense regions) is lighter, we use the functional form of (11) for computing object-feature-based affinity μ_ϕ . To determine a set of pixels in the dense region, the largest intensity value MAX is determined by ignoring the upper 0.1 percentile of intensity in the histogram of the breast region. Similarly, the smallest intensity value MIN is determined by ignoring the lower 0.1 percentile of intensity. We then select within the breast the set of pixels having intensity not less than $MIN + 0.75(MAX - MIN)$ for estimating the parameters. Specifically, we take the mean and standard deviation of the intensities of the pixels in this set as the values of m_ϕ and σ_ϕ . Further, we take the mean and standard deviation of intensity differences between all pairs of adjacent pixels in this set as the values of m_ψ and σ_ψ . Finally, the set of pixels

in the breast region with intensity greater than $MIN + 0.85(MAX - MIN)$ is used as the set of reference pixels. Figure 2(d) shows the scale-based fuzzy connectivity scene obtained for the dense region for the original mammogram in Figure 2(a). In the next section, we describe an automatic threshold selection method that is applied to the fuzzy connectivity scene for the dense region for a segmentation of the breast region into dense and fatty regions.

C. Automatic threshold selection

The connectivity scene is an image in which pixels hanging together strongly with the reference pixels supposedly all belong to the same object region [24]. It is usually easy to segment the object region by thresholding the connectivity scene even if the original scene is not amenable for thresholding. This property of fuzzy connectedness is demonstrated in [24] and a quantitative validation is presented in [25]. In the past, in other applications utilizing fuzzy connectedness [10], [13], [14], [15], we have used fixed thresholds on connectivity scenes. In this application, we found that fixing the connectedness threshold is not always satisfactory, although each connectivity scene is still far more amenable to thresholding than the original. With this as the motivation, we developed an automatic threshold selection strategy for connectivity scenes, building on the idea of homogeneity-based affinity described in the previous selection but as applied to the connectivity scene.

To select the best threshold, the method minimizes an energy function computed by considering spatial arrangements of pixel intensities within each region and across regions. We emphasize that the processing is now confined to the breast region. The basic idea is as follows. Every threshold divides the scene into two regions. A second order statistic, threshold energy, of local disagreements in the scene stemming from this partitioning is estimated and is used as a criterion for optimizing the threshold. Threshold energy characterizes the goodness (rather, badness) of a particular threshold and is defined as follows. Let B denote the set of pixels in the segmented breast region. We define two fuzzy relations ρ and $\bar{\rho}$, respectively called *likeliness of belonging to the same object* and *likeliness of belonging to different objects*, on the pixels in B . The strengths of both these relations between any two pixels c and d in B depend on (1) how far c and d are; and on (2) how similar the intensity values (or other features) of the pixels in the circular

neighborhood around c are to those around d . As discussed in Section II, the size of the circular neighborhoods around c and d depends on the object scales at c and d . In fact the criterion in (2) is the measure of homogeneity-based affinity μ_ψ between c and d . Two controlling parameters (indicating expected object homogeneity) are required to calculate the value of μ_ψ as described earlier. These two parameters are estimated as the mean and the standard deviation of intensity differences of all pairs of adjacent pixels in the region with pixel intensities (connectedness values) falling in the upper half of the histogram of the connectivity scene. The strength of the fuzzy relation “likeliness of belonging to the same object” between two pixels $c, d \in B$, denoted $\mu_\rho(c, d)$, is then defined as follows.

$$\mu_\rho(c, d) = \mu_\alpha(c, d) \frac{\sum_{\substack{a, b \in B \text{ s.t.} \\ \mu_\psi(a, b) \leq \mu_\psi(c, d)}} \mu_\alpha(a, b)}{\sum_{a, b \in B} \mu_\alpha(a, b)}. \quad (16)$$

The strength of the fuzzy relation “likeliness of belonging to different objects” between two pixels $c, d \in B$, denoted $\mu_{\bar{\rho}}(c, d)$, is defined as follows.

$$\mu_{\bar{\rho}}(c, d) = \mu_\alpha(c, d) \left(1 - \frac{\sum_{\substack{a, b \in B \text{ s.t.} \\ \mu_\psi(a, b) \leq \mu_\psi(c, d)}} \mu_\alpha(a, b)}{\sum_{a, b \in B} \mu_\alpha(a, b)} \right). \quad (17)$$

Let $f_p(c, d, t)$ denote a predicate that takes a value 1 when the pixels c, d belong to the same object at the threshold t and 0 otherwise. Then the threshold energy $E(t)$ is determined as follows.

$$E(t) = \sum_{c, d \in B} f_p(c, d, t) \mu_\rho(c, d) + (1 - f_p(c, d, t)) \mu_{\bar{\rho}}(c, d). \quad (18)$$

In words, $E(t)$ expresses the level of concordance between the two regions resulting by applying the threshold t to the connectivity scene. Finally, the threshold for which $E(t)$ is minimum (indicating minimum concordance or maximum discordance between the two regions) is selected as the optimum threshold. For the fuzzy connectivity scene of Figure 2(d), the distribution of $E(t)$ is shown in Figure 3(a), while Figure 3(b) shows the location of the optimum threshold on the histogram of the connectivity scene of Figure 2(d). The segmented binary scene is shown in Figure 3(c).

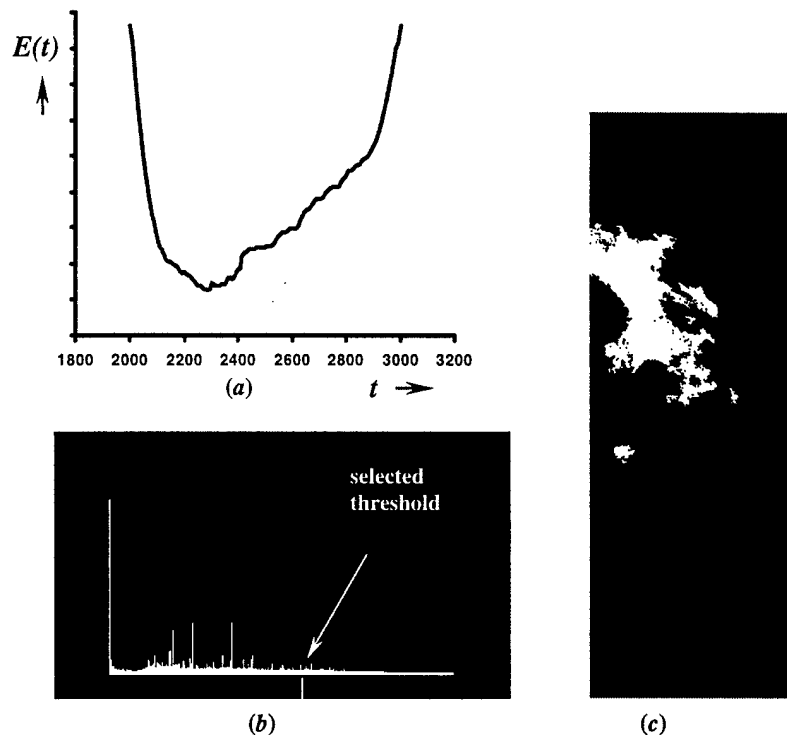


Fig. 3. (a), (b) Threshold energy and connectivity strength distributions for the connectivity scene of Figure 2(d). (c) Segmented dense region using automatic thresholding.

D. Density Quantification

From the original scene and the segmented fat and dense regions, the following parameters are computed.

TG: Total density within the breast region defined as the sum of intensities of pixels in the segmented dense region.

TF: Total fat within the breast region defined as the sum of intensities of pixels in the segmented fat region.

AB: Total area of breast defined as the number of pixels in the segmented breast region.

AG: Total area of density within the breast region defined as the number of pixels in the segmented dense region.

AF: Total area of fat within the breast region defined as the number of pixels in the segmented fat region.

AvF: Average pixel intensity within the fat area defined by TF/AF.

The following parameters, some of which are derived from the above, which may be more meaningful, are actually used in our testing: TG, TG/TF, TG/AvF, TG/AB, AG, AG/AF, and AG/AB. Linear correlations of each of these parameters across two different projections (CC and MLO) were tested for all 60 studies.

IV. RESULTS AND DISCUSSION

The method has been tested in two ways — (1) by studying correlation of each density parameter computed from patients' mammograms at two different projections, and (2) by studying the accuracy of the method in terms of the area of mismatch between dense regions segmented by the new method and by manual outlining.

A. Patient Mammograms

The method has been tested on 60 studies selected from our database. Each study had two mammographic projections — CC and MLO. These mammograms were digitized on a Lumisys scanner at a resolution of 100 microns. The population includes 30 normal studies as well as 14 studies with benign and 16 with malignant masses and calcifications. Except for the exclusion of pectoral muscles in some cases, the entire method worked automatically on all mammograms wherein all parameters required by the algorithms were selected automatically. An additional 54 mammograms were processed for a different project — to assess the effect of hormone therapy on breast density. The algorithms produced visually acceptable segmentations in all 174 cases. Figure 4 demonstrates the results of application of the proposed automatic method on several mammograms. The linear correlation coefficients for the parameters TG, TG/TF, TG/AvF, TG/AB, AG, AG/AF, and AG/AB derived from the two sets of projection images were 0.967, 0.902, 0.951, 0.944, 0.959, 0.915, and 0.941, respectively. The scatter plots and the R-values of different parameters across the two different projections over 60 pairs of mammograms are shown in Figures 5(a)–(g). In all these figures, the horizontal axis represents logarithmic value of the estimated parameter for each mammogram at the CC projection while the vertical axis represents the same for the matching mammogram at MLO projection. Although the scatter plots display logarithmic values, the R-values of linear correlation were computed on actual values of the parameters. It may be pointed out the the actual scatter in the

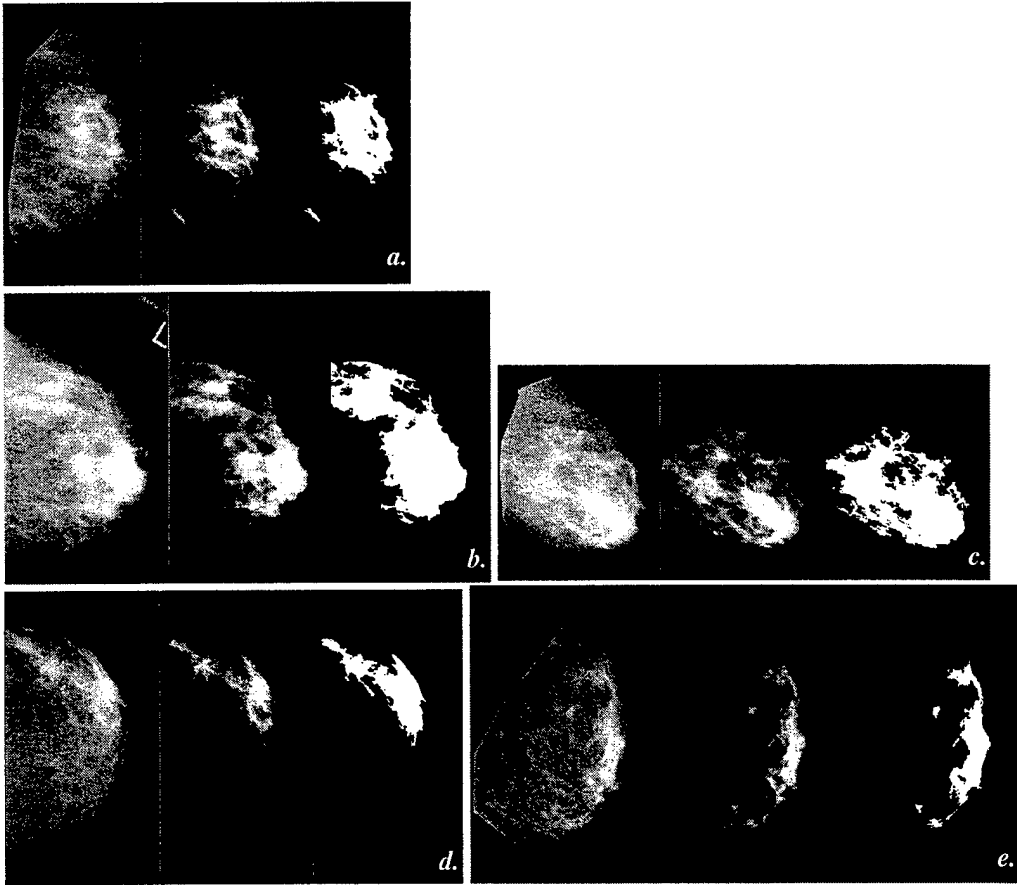


Fig. 4. Results of application of the proposed density segmentation method on several mammograms at CC and MLO projections. In each set, the original scene, the connectivity scene for the dense region and the segmented dense region are shown.

log-log graphs appear less. However, the log-log graphs were used to present compact displays for large data ranges. The ranges of gradients and y-intercepts of the trend lines were 0.998 to 1.0095 and -0.2893 to -0.0704, respectively.

The high value of correlation coefficients indicates that our method of measurement is highly consistent between the two projection images of the same patient. The highest correlation is obtained for TG. Generally the parameters that use area measurements yielded lower correlations. The argument behind this may be that unless the 3D shape of the actual dense region in the breast is approximately spherical, the shapes of its CC and MLO projections may be quite different from each other. This may yield very different area measures (AG, AF) although the total density may still be the same. To

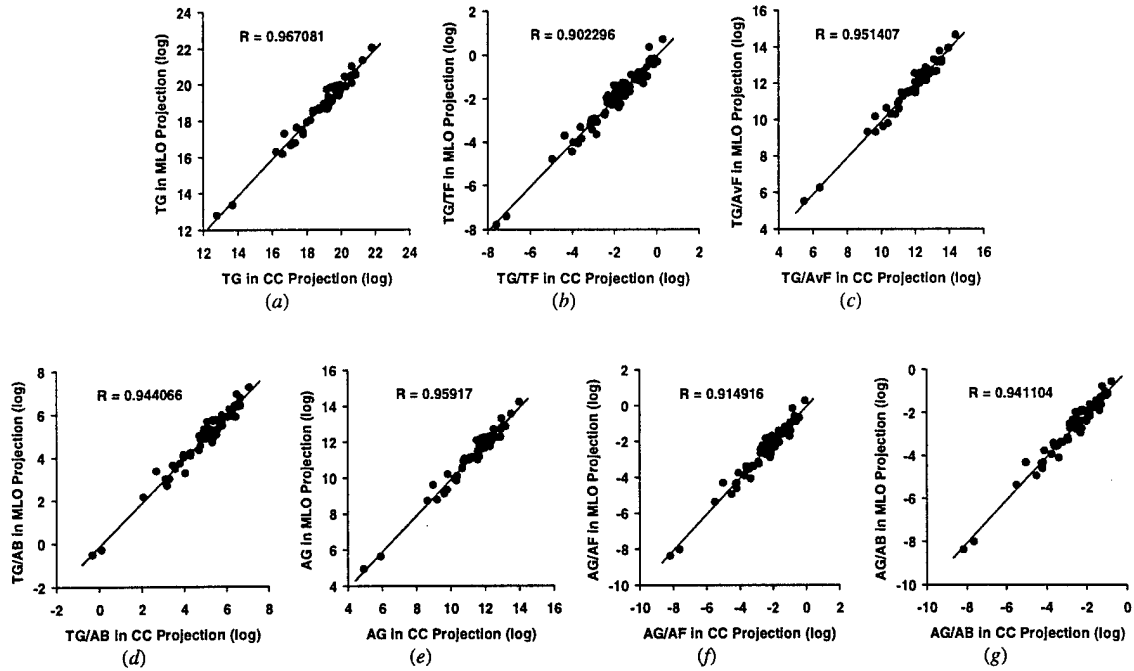


Fig. 5. (a)–(g) Scatter plots and R-values of correlation studies for different quantitative parameters computed from mammograms at CC and MLO projections. In each scatter plot, the horizontal axis indicates the logarithmic value of the parameter at CC projection while the vertical axis indicates the same at MLO projection.

verify this hypothesis, we selected among the 60 pairs of studies a subset of 20 pairs in which the shapes of projections of the same breast in CC and MLO appeared quite different. For this subset, we then computed the correlation coefficients. The coefficients for TG and AG for this subset were 0.898 and 0.68, respectively. The scatter plot for this experiment is shown in Figures 6(a),(b). To estimate statistical significance of the difference of the correlation coefficients for these two populations, we used the Fisher's Z-transformation test [30]. The p -value was 0.036245 showing that the difference in the correlation coefficients is statistically significant. However, the actual data were skewed and after removing the stray observations the p -value rose to 0.361511 indicating that the difference was not significant. The primary reason behind this disagreement may be the high nonlinearity between the total length in 3D of the tissue intercepted by a beam of X-ray and the outcoming energy. If this nonlinearity is corrected for with a knowledge of the length of interception, then we believe that TG and related parameters will correspond

more accurately to actual total density than the area-based parameters.

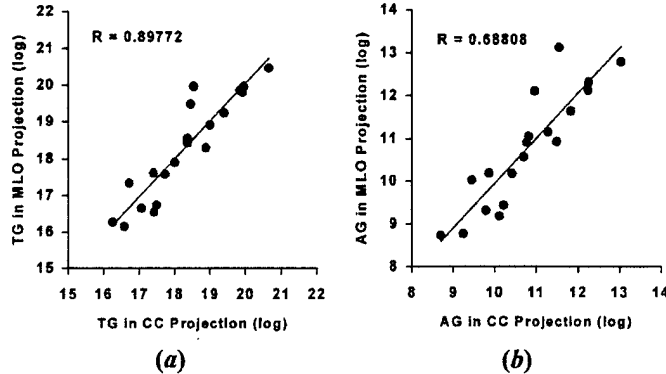


Fig. 6. (a)–(b) Scatter plots and R-values of correlation studies of TG and AG for a set of 20 studies with quite different shape at different projection. In each scatter plot, the horizontal axis indicates the logarithmic value of the parameter at CC projection while the vertical axis indicates the same at MLO projection.

B. Comparison with Manual Outlining

A major difficulty in validating a density quantification method is how to generate the truth. Creation of a realistic physical breast phantom with known volume of dense tissue with realistic shape and distribution is a research topic of its own. In this paper, we have used manual outlining of dense regions by an expert mammographer to provide a surrogate of this truth. The outlining was performed using a computerized freehand drawing tool on digitized mammograms as supported by 3DVIEWNIX [26]. An example of manual outlining is presented in Figure 7. The task of manual outlining is difficult, quite ill-defined, and has its own limitations in terms of definition and inter and intra-operator variability. Additionally, we observed that the correlation of the density parameters computed from manual outlining is lower than that using the proposed method. 15 pairs of mammograms were randomly selected from our data set of 60 pairs of mammograms. Dense regions in each mammogram were manually outlined by the same expert and the parameters TG and AG were computed over the delineated regions. The linear correlation coefficients for TG and AG were 0.638 and 0.534, respectively. The scatter plots and the R-values of these two parameters across the two projections over 15 pairs of mammograms are shown



Fig. 7. An example of manual outlining. The border of the dense region is shown bright.

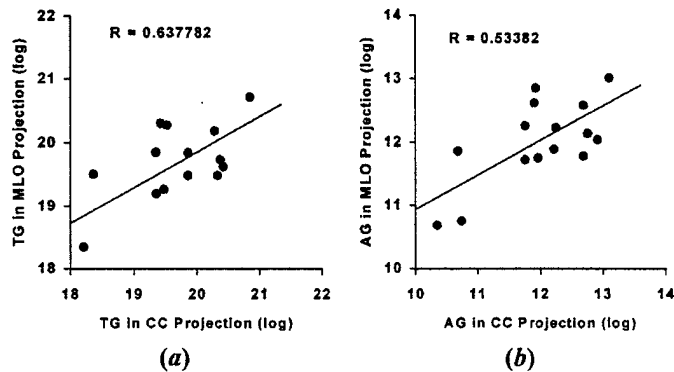


Fig. 8. (a)–(g) Scatter plots and R-values of correlation studies for the parameters TG and AG computed from mammograms at CC and MLO projections. In each scatter plot, the horizontal axis indicates the logarithmic value of the parameter at CC projection while the vertical axis indicates the same at MLO projection.

in Figures 8(a) and (b).

While the correlation of different density parameters computed by the proposed method is demonstrated in the previous section, the purpose of the experiment described here is to show that the disagreement of the results produced by the automatic method with those of manual outlining is within the limitation range of the second method itself. 15 mammograms were randomly selected from our data set of 120 mammograms. Dense regions in each of these mammograms were manually outlined by the same expert at two

different time instants (with a gap of 2 days). Also, the dense regions were segmented in each mammogram using the proposed method. For each mammogram, two percent areas of mismatch, AM , were computed, one between the results of manual segmentation at different time instants and the other between the results of manual segmentation at the first time instant and those using the proposed method. If X and Y are the two sets of pixels being compared, $AM(X, Y)$ was defined by $\frac{|X \text{ EOR } Y|}{(|X|+|Y|)/2} \times 100$. The 95% confidence interval of AM for manual segmentation at different time instants was [0, 22.81] and that for manual and the automatic method was [0, 18.14]. This shows that the disagreement of delineation using the proposed method with manual outlining is within the range of variability of the latter method itself.

V. CONCLUSION

A near automatic method for quantification of breast density from digitized mammograms has been developed and tested on 87 pairs of patient mammograms. This method was executed automatically except for the exclusion of projected pectoral muscles. The method consists of the following steps: separation of the breast from the background, creation of a fuzzy connectivity scene for the dense region, segmenting this connectivity scene using an automatic threshold selection method, and then computing various parameters that characterize total breast density. A set of density and area related parameters has been proposed and their precision in terms of their linear correlation across two different projections has been studied. The scale-based fuzzy connectivity method has been found to be very robust and effective in segmenting the mammographic images. Amount of density is considered to be one of the strongest risk factors for breast cancer. Automatic, repeatable, and consistent breast density quantification from digitized mammograms is practical using the proposed method. The correctness of the proposed density quantification method has been validated in two ways — (1) showing high R-values of linear correlation between the two projections (CC, MLO) of the various parameters computed over segmented dense and fatty regions and (2) demonstrating the disagreement between delineations using the proposed method and using manual outlining to be within the range of variability of the second method. The method removes the subjectivity inherent in interactive threshold selection techniques currently used. The ability of the computed density

parameters in evaluating risk is currently being investigated at our institution.

A comparison between the mammographic density parameter taking into account the original intensities and that considering just the segmented area has been carried out. The motivations behind this consideration was that unless the 3D shape of the actual dense region in the breast is approximately spherical, the shapes of its CC and MLO projections may be quite different from each other while intensity based parameters would better capture the thickness and volume of the dense region using intensity information. For 60 pairs of mammograms at CC and MLO projections, generally the parameters that use area measurements yielded lower correlations. To verify this argument, we selected among the 60 pairs of studies a subset of 20 pairs in which the shapes of projections of the same breast in CC and MLO appeared quite different and difference in the correlation coefficients was statistically significant. However, when the skewness of data was removed by removing stray observations, there was no significant difference in correlation coefficients. The primary reason behind this disagreement may be the high nonlinearity between the total length in 3D of the tissue intercepted by a beam of X-ray and the outcoming energy. Another hurdle in using intensity related parameters originates from the fact that the values of these parameters do not indicate the actual volume of dense regions. This is because, actual intensities in mammograms are dependent on different imaging parameters such as the energy and the frequency of X-rays used, plate thickness, film characteristics and X-ray attenuation coefficients of different tissues of different patients. It will be useful in the future to resolve this problem of nonlinearity and to somehow normalize the total density parameters such that they relate to the physical volume of dense regions.

ACKNOWLEDGMENTS

The authors are grateful to Drs. Larry Toto, H. L. Kundel for the digitized mammographic data set. The work of the authors is supported by grants DAMD 179717271 from the Department of Army and NS 37172 from NIH.

REFERENCES

- [1] J.N. Wolfe, "Breast pattern as an index of risk for developing breast cancer", *AJR*, **126**, pp. 1130-1139, 1976.
- [2] J.N. Wolfe, "Breast parenchymal patterns and their changes with age", *Radiology*, **121**, pp. 545-552, 1976.

- [3] E. Warner et. al., "The risk of breast-cancer associated with mammographic parenchymal patterns: a meta-analysis of the published literature to examine the effect of method of classification", *Cancer Detection and Prevention*, **16**, pp. 67–72, 1992.
- [4] A.M. Oza and N.F. Boyd, "Mammographic parenchymal patterns: a marker of breast cancer risk", *Epidemiologic Reviews*, **15**, pp. 196–208, 1993.
- [5] J.N. Wolfe, "Risk for breast cancer development determined by mammographic parenchymal pattern", *Cancer*, **37**, pp. 2486–92, 1976.
- [6] N.F. Boyd, J.W. Byng, R.A. Jong, E.K. Fishell, L.E. Little, A.B. Miller, G.A. Lockwood, D.L. Tritchler, and M.J. Yaffe, "Quantitative classification of mammographic densities and breast cancer risk: results from the Canadian national breast screening study", *Journal of the National Cancer Institute* **87**, pp. 670–675, 1995.
- [7] M. Moscowitz, P. Gartside, and C. McLaughlin, "Mammographic patterns as markers for high-risk benign breast disease and incident cancers", *Radiology*, **134**, pp. 293–5, 1980.
- [8] J.N. Wolfe, A.F. Saftlas, and M. Salane, "Mammographic parenchymal patterns and quantitative evaluation of mammographic densities: a case control study", *American Journal of Roentgenology*, **148**, pp. 1087–92, 1987.
- [9] J. K. Udupa, L. Wei, Y. Miki, and R. I. Grossman, "A system for comprehensive analysis of multiple sclerosis lesion load based on MR imagery", *SPIE Proceeding*, **3031**, pp. 610–618, 1997.
- [10] J. K. Udupa, L. Wei, S. Samarasekera, Y. Miki, M. A. van Buchem, and R. I. Grossman, "Multiple sclerosis lesion quantification using fuzzy connectedness principles", *IEEE TRAns. Medical Imaging*, **16**, pp. 598–609, 1997.
- [11] Y. Miki, R. I. Grossman, J. K. Udupa, M. A. van Buchem, L. Wei, M. D. Philips, U. Patel, J. C. McGown, and D. L. Kolson, "Differences between relapsing remitting and chronic progressive multiple sclerosis as determined with quantitative MR imaging", *Radiology*, **210**, pp. 769–774, 1999.
- [12] Y. Miki, R. I. Grossman, J. K. Udupa, L. Wei, M. Polansky, L. J. Mannon, and D. L. Kolson, "Relapsing-remitting multiple sclerosis: longitudinal analysis of MR images — lack of correlation between changes in T2 lesion volume and clinical findings", *Radiology*, **213**, pp. 395–399, 1999.
- [13] A. Kumar, W. Bilker, J.K. Udupa, and G. Gottlieb, "Late onset minor and major early evidence for common neuroanatomical substrates detected by using MRI", *proceedings of the National Academy of Science*, **95**, pp. 7654–7658, 1998.
- [14] B. L. Rice, Jr. and J. K. Udupa, "Clutter-free volume rendering for magnetic resonance angiography using fuzzy connectedness", *International Journal of Imaging Systems and Technology*, **11**, pp. 62–70, 2000.
- [15] J.K. Udupa, J. Tian, D.C. Hemmy, and P. Tessier, "A pentium-based craniofacial 3D imaging and analysis system", *Journal of Craniofacial Surgery*, **8**, pp. 333–339, 1997.
- [16] S.M. Lippman, T.L. Bassford, and F.L. Meyskens, Jr., "A quantitatively scored cancer-risk assessment tool: its development and use", *Journal of cancer Education*, **7**, pp. 15–36, 1992.
- [17] R.T. Chlebowski et. al., "Breast cancer chemoprevention tamoxifen: current issues and future prospective", *Cancer* **72**, pp. 1032–7 Supplement, 1993.
- [18] J. M Boone, K. K. Lindfors, C. S. Beatty, and J. A. Selbert, "A breast density index for digital mammograms based on radiologists' ranking", *Journal of Digital Imaging*, **11**, pp. 101–115, 1998.
- [19] J. W. Byng, N. F. Boyd, L. Little, G. Lockwood, E. Fishell, R. A. Jong, and M. J. Yaffe, "Symmetry of

projection in the quantitative analysis of mammographic images”, *European Journal of Cancer Prevention*, **5**, pp. 319–327, 1996.

[20] G. Ursin, A. Melvin, A. Astrahan, M. Salane, Y. R. Parisky, J. G. Pearce, J. R. Daniels, M. C. Pike, and D. V. Spicer, “The detection of changes in mammographic densities”, *Cancer Epidemiology, Biomarkers and Prevention*, **7** pp. 43–47, 1998.

[21] Z. Huo, M. L. Giger, O. I. Olopade, and S. A. Cummings, “Computerized analysis of parenchymal patterns for the assessment of breast cancer risk”, *Supplement to Radiology, RSNA*, **209(P)**, pp. 354, 1998.

[22] J. Suckling, D. R. Lewis, and S. G. Blacker, “Parenchymal delineation by human and computer observers”, in Proceeding of the 2nd International Workshop on Digital Mammography, Eds. A.G. Gale et. al., York, England, 1994.

[23] R. Highnam, M. Brady, and B. Shepstone, “A representation for mammographic image processing”, *Medical Image Analysis*, **1**, pp. 1–18, 1996.

[24] J. K. Udupa and S. Samarasekera, “Fuzzy connectedness and object definition: theory, algorithms, and applications in image segmentation”, *Graphical Models and Image Processing*, **58**, pp. 246–261, 1996.

[25] P. K. Saha, J. K. Udupa, and D. Odhner, “Scale-based fuzzy connected image segmentation: theory, algorithms, and validation”, *Computer Vision Image Understanding*, **77**, pp. 145–174, 2000.

[26] J.K. Udupa, D. Odhner, S. Samarasekera, R.J. Goncalves, K. Iyer, K. Venugopal, and S. Furui, “3DVIEWNIX: a open, transportable, multidimensional, multimodality, multiparametric imaging system, proceedings of SPIE”, **2164**, pp. 58–73, 1994.

[27] A.X. Falcão, J.K. Udupa, S. Samarasekera, and S. Sharma, “User-steered image segmentation paradigms: live wire and live lane”, *Graphical Models Image Processing* **60**, pp. 233–260, 1998.

[28] M. Tabb and N. Ahuja, “Multiscale image segmentation by integrated edge and region detection”, *IEEE Trans. Image Processing*, **6**, pp. 642–655, 1997.

[29] T. Lindeberg, *Scale-Space Theory in Computer Vision*, Boston, MA: Kluwer, 1994.

[30] R. F. Woolson, *Statistical methods for the analysis of biomedical data*, New York: Wiley, 1987.

[31] T.S. Curry, J.E. Dowdley, and R. C. Murry Jr., *Christensen's Introduction to the Physics of Diagnostic Radiology*, Lea & Febiger, Philadelphia, 1984.